

USING PHYSICAL SCIENCES APPROACHES TO INVESTIGATE THE MINERALIZED
MICROENVIRONMENTS OF METASTATIC BREAST CANCER

A Dissertation

Presented to the Faculty of the Graduate School

of Cornell University

In Partial Fulfillment of the Requirements for the Degree of

Doctor of Philosophy

by

Frank He

December 2018

© 2018 Frank He

USING PHYSICAL SCIENCES APPROACHES TO INVESTIGATE THE MINERALIZED MICROENVIRONMENTS OF METASTATIC BREAST CANCER

Frank He, Ph.D.
Cornell University, 2018

Breast cancer is among the most common malignancy in women worldwide. Progress in early detection and targeted therapeutics have improved the clinical prognosis of patients with localized cancer. However, high mortality rates and short median survival times continue to be associated with skeletal metastases, which occur in 80% of patients with advanced disease. These dismal statistics reflect an inadequate mechanistic understanding of the microenvironmental factors that mediate the progression of primary breast cancer to bone metastasis. In particular, hydroxyapatite (HA) mineral, a key component of mammary calcifications and an essential nanostructural constituent of bone tissue, has largely been overlooked in studies of breast cancer, but may play an important role in its malignant progression. Thus, the overall goal of this work was to examine the relevance of HA mineral to bone metastatic disease within mineralized microenvironments specific to the breast cancer metastatic cascade. To this end, innovative, interdisciplinary approaches spanning tissue engineering, materials science, and cell biology were pursued. Chapter 2 focuses on the functional characterization of tumor cell-HA interactions and details the use of a tissue-engineered scaffold system to investigate whether HA can actively promote breast cancer cell malignancy. Interestingly, it was found that premalignant MCF10DCIS.com cells exposed to HA mineral adopted morphological changes associated with increased invasiveness and exhibited increased motility that was dependent on IL-8 signaling. Furthermore, DCIS xenograft tumors initiated in HA scaffolds exhibited evidence of increased malignant progression. Meanwhile, chapter 3 describes a multiscale characterization of the bone metastatic site in animal models of advanced breast cancer. Here, by combining high resolution X-ray scattering analysis with large

area Raman imaging, backscattered electron microscopy, histopathology, and micro-computed tomography, it was observed that HA nanocrystal immaturity may be linked with secondary tumor formation in bone and that mammary tumors remotely alter HA nanostructure via possible osteogenic mechanisms. Collectively, the results from this work suggest a dynamic reciprocity between breast cancer cells and the HA embedded within their mineralized microenvironments. More studies will be needed to elucidate the mechanisms by which tumor cell-HA interactions drive malignancy to potentially identify improved therapeutic strategies. Importantly, this work has provided a framework for how future studies could utilize tissue engineering and materials science approaches to investigate mineralized tumor microenvironments relevant to breast cancer and bone metastasis.

BIOGRAPHICAL SKETCH

Frank He was born in Shanghai, China on May 9, 1986. At an early age, he immigrated with his parents to the United States, where he grew up in the suburbs of Northern New Jersey. During his formative high school years at the Bergen County Academies in Hackensack, he discovered a fascination with the life sciences. Frank went on to pursue a degree in Molecular and Cell Biology at the University of California at Berkeley, achieving Magna Cum Laude with Phi Beta Kappa Honors. Following his graduation, he worked as a Research Associate at the Cancer Program of the Broad Institute of MIT and Harvard, where he developed novel technologies to systemically assess phosphorylation profiles of signaling proteins.

In Fall of 2011, Frank matriculated at Cornell University as a doctoral student in the Department of Biomedical Engineering. He joined Dr. Claudia Fischbach's group to utilize physical sciences and engineering approaches to investigate tumor-matrix interactions in cancer microenvironments. Frank has presented regularly at conferences, published a book chapter, and was the primary author on two research manuscripts. As a GAANN Teaching fellow, he developed and taught a module for the course 'Molecular Principles in Biomedical Engineering.' He has enjoyed mentoring undergraduates as part of the Cornell Office of Academic Diversity Initiatives mentoring program and has been inducted into the Edward A. Bouchet Graduate Honor Society. Frank has won numerous awards while in graduate school, including the National Science Foundation GRFP, the Presidential Life Science Fellowship, and the Howard Hughes Med-into-Grad Fellowship. Frank will conduct his postdoctoral studies at the Dana-Farber Cancer Institute in Boston, and he looks forward to building a scientific career that will impact biomedicine and healthcare.

ACKNOWLEDGMENTS

This dissertation represents the culmination of a challenging yet rewarding seven-year journey. During this time, I have been fortunate to have received the support and mentorship of the many individuals who have shaped my graduate school experience.

My committee has been an invaluable source of guidance. First and foremost, I must thank my advisor and committee chair, Dr. Claudia Fischbach, who has been a dedicated mentor from the very start. She has challenged me to become a better scientist and has inspired me to become a more well-rounded person. I enjoyed a good working relationship with Dr. Lara Estroff, who was an excellent collaborator and has generously provided me with her technical expertise. I would also like to thank Dr. Tracy Stokol, who has challenged me to go beyond the engineered model systems and the materials characterization approaches to think deeply and critically about the physiological relevance of my work.

I was able to gain new skills and perspectives by spending time outside of Ithaca. While at the Max Planck Institute of Colloids and Interfaces in Potsdam, I was grateful to have had the opportunity with Dr. Peter Fratzl, whose scientific intuition, creativity, and enthusiasm were inspirational. I would also like to acknowledge my other colleagues in Germany – especially Dr. Wolfgang Wagermaier, Dr. Admir Masic, Dr. Bettina Willie, and Dr. Georg Duda – who were all supportive and generous with their time. During my clinical immersion term at Memorial Sloan Kettering Cancer Center, I had the great opportunity to learn from Dr. John Healey, who encouraged me to think about cancer as a more holistic disease rather than something that can be studied solely with models that focus only on specific questions.

I have had the privilege of being able to work with so many talented and hardworking people in the Cornell community. I looked forward to days when I could visit my colleagues across campus, sometimes discussing science and other-times sharing laughs. Thank you for all

for bringing such warmth and positivity to my life. I must acknowledge the Biomedical Engineering administrative staff who have been so welcoming and supportive from the very day I set foot on campus. And of course, to the wonderful members of the Fischbach Lab, thank you for your friendship over the years. I have learned so much from you and I will miss you.

This graduate research would not have been possible without my family. My father's curiosity of the natural world is what inspired me to pursue science in the first place. My mother has always encouraged me to find ways to realize my potential and to live a life that I would be proud of. Special thanks to Stella, my lovely girlfriend, who has showed her unwavering support for me during the stressful period of thesis work.

Finally, I would like to thank my funding sources, which include the National Science Foundation, Howard Hughes Medical Institute, the United States Department of Education, the National Institutes of Health, and the National Cancer Institute.

TABLE OF CONTENTS

CHAPTER 1: INTRODUCTION.....	1
1.1 Hydroxyapatite mineral and bone metastatic breast cancer.....	1
1.2 Mineralized microenvironments of the breast cancer-bone metastasis cascade.....	3
1.2.1 Relationships between mammary calcifications and cancer	4
1.2.2 Bone mineral properties and relevance to metastasis.....	7
1.3 Investigating cell-mineral interactions using engineered culture models.....	10
1.4 Materials characterization of HA in mineralized tissues	11
1.4.1 X-ray scattering	12
1.4.2 Raman Imaging	13
1.5 Research Objectives.....	15
1.6 References.....	18
CHAPTER 2: HYDROXYAPATITE MINERAL ENHANCES MALIGNANT POTENTIAL IN A TISSUE-ENGINEERED MODEL OF BREAST CANCER	25
2.1 Abstract.....	25
2.2 Introduction.....	26
2.3 Materials and Methods.....	28
2.3.1 Cell lines and growth media	28
2.3.2 Scaffold fabrication	28
2.3.3 Three-dimensional cell culture	29
2.3.4 Scaffold characterization	29
2.3.5 Analysis of cell proliferation and IL-8 expression	29
2.3.6 Cell morphology and cell clustering analysis.....	30
2.3.7 Cell motility analysis.....	31
2.3.8 Human sample analysis	32
2.3.9 Scaffold-xenograft studies.....	33
2.3.10 Statistical analyses.....	34
2.4 Results.....	34
2.4.1 Mineral-containing PLG scaffolds enable study of cell-mineral interactions in 3D.....	34
2.4.2 Correlation between IL-8 enrichment and presence of mammographic calcifications and proliferative ductal epithelia.....	36
2.4.3 HA mineral regulates proliferation and IL-8 expression across breast cancer cell lines ...	37
2.4.4 DCIS cells interacting with HA mineral in 3D adopt morphological hallmarks of invasiveness.....	39
2.4.5 HA mineral increases DCIS cell motility mediated by IL-8	41
2.4.6 DCIS xenografts exposed to HA mineral in scaffolds exhibit characteristics associated with increased malignancy	43

2.5 Discussion.....	46
2.6 Acknowledgements.....	50
2.7 References.....	51
CHAPTER 3: MULTISCALE CHARACTERIZATION OF THE MINERAL PHASE AT SKELETAL SITES OF BREAST CANCER METASTASIS	56
3.1 Abstract.....	56
3.2 Introduction.....	57
3.3 Materials and Methods.....	61
3.3.1 Tibiae from mouse xenograft models of breast cancer	61
3.3.2 Micro-computed tomography (μ CT).....	61
3.3.3 Backscattered electron microscopy (BSE)	62
3.3.4 Histological studies	62
3.3.5 Small-angle X-ray scattering measurements (SAXS).....	62
3.3.6 Synchrotron measurements (SAXS/WAXS).....	63
3.3.7 Statistical analysis of X-ray scattering data.....	64
3.3.8 Large area Raman imaging.....	64
3.3.9 Analysis of mouse tibiae from cell-tree tumor conditioning.....	65
3.3.10 In vitro assessment of osteogenic differentiation	66
3.4 Results.....	67
3.4.1 In tibiae of healthy mice, HA nanocrystals are more immature in regions prone to metastasis.....	67
3.4.2 Metastasis initiation in the proximal tibial metaphysis alters the bone ECM	69
3.4.3 Metaphyseal HA nanostructure is altered by the presence of a localized mammary tumor.....	75
3.5 Discussion.....	81
3.6 Acknowledgements.....	85
3.7 References.....	86
CHAPTER 4: CONCLUSIONS	90
4.1 A dynamic reciprocity between breast cancer cells and HA mineral	90
4.2 Connections to the “seed-and-soil” theory of metastasis.....	92
4.3 Future directions and perspectives.....	95
4.3.1 Considerations for developing mineral-containing models of breast cancer and bone metastasis.....	95
4.3.2 Organs-on-a-chip: modeling metastatic processes on a whole-body level	96
4.3.3 Concluding remarks: physical sciences approaches may accelerate cancer research	97
4.4 References.....	98
APPENDIX.....	101

LIST OF FIGURES AND TABLES

Figure 1.1: Mineralized microenvironments in the primary and secondary bone site of breast cancer	2
Figure 1.2: Mammary microcalcifications.....	5
Figure 1.3: Bone structure is affected by cancer metastasis	8
Figure 1.4: HA-containing polymeric scaffolds	11
Figure 1.5: Characteristics of bone mineral nanostructure obtained via X-ray scattering	13
Figure 1.6: A typical Raman spectrum of bone	14
Figure 2.1: Mineral-containing PLG scaffolds enable study of cell-mineral interactions in 3D..	35
Figure 2.2: Histopathological analysis of human breast cancer samples correlates IL-8 enrichment with the presence of mammographic calcifications and proliferative ductal epithelia.....	36
Figure 2.3: Hydroxyapatite mineral regulates proliferation and IL-8 expression across breast cancer cells.....	38
Figure 2.4: IL-8 expression of MDA-MB-231 cells cultured in HA scaffolds is mediated by the integrin $\alpha\beta 3$	38
Figure 2.5: DCIS cells interacting with hydroxyapatite mineral in 3D culture adopt morphological hallmarks of invasiveness.....	40
Figure 2.6: Calculation of the Morphology Factor captures a range of migratory cell shapes in scaffold cultures of DCIS cells	41
Figure 2.7: Hydroxyapatite mineral increases DCIS cell motility mediated by IL-8.....	42
Figure 2.8: DCIS cells exposed to pre-culture in hydroxyapatite-containing scaffolds may exhibited IL-8 dependent directed migration.....	43
Figure 2.9: DCIS xenografts in hydroxyapatite scaffolds exhibit characteristics associated with increased malignancy.....	45
Figure 3.1: X-ray scattering analysis setup.....	59
Figure 3.2: Experimental setup for multiscale analysis of bone hierarchical structure.....	60

Figure 3.3: Laboratory-based SAXS analysis of tibiae from healthy mice shows that hydroxyapatite nanocrystals in the metaphysis are more immature than ones in the diaphysis....68

Figure 3.4: Mouse models of advanced breast cancer69

Figure 3.5: Multiscale characterization of the bone metastatic site identifies changes in the extracellular matrix associated with secondary tumor formation70

Figure 3.6: Representative Movat’s Pentachrome (MP) stained cross-sections shows massive destruction of metaphyseal trabecular bone and severe disruption of the epiphyseal chondrocytes in tibiae with metastasis71

Figure 3.7: The metaphysis experiences severe degradation during bone metastasis while the diaphysis remains unaffected72

Figure 3.8: Collagen type I content is decreased in metaphyseal bone that is interfacing with the secondary tumor73

Figure 3.9: Large area Raman imaging indicates that the phosphate-to-amide ratio ($PO_4/Amide\ I$) is increased in metaphyseal bone interfacing with a secondary tumor74

Figure 3.10: Large area Raman imaging indicates that metaphyseal bone mineral crystallinity ($FWHM^{-1} * 100$ of the $PO_4\ v1$ peak) is increased in mice with localized mammary tumors as well as in mice with bone metastasis74

Figure 3.11: Macro- to micro-scale analysis of metaphyseal bone suggests no structural differences between control mice and mice with mammary tumors76

Table 3.1: Summary of ρ - and T-parameter data from laboratory-based SAXS analysis76

Figure 3.12: Scanning synchrotron-based SAXS/WAXS analysis of metaphyseal tissue bordering the growth plate reveals shorter hydroxyapatite nanocrystals in mice carrying mammary tumors78

Figure 3.13: Tumor-secreted factors can promote osteogenic activity80

Figure 3.14: Proposed functional relationship between hydroxyapatite mineral characteristics and breast cancer bone metastasis84

Figure A.1: Hydroxyapatite mineral may increase SRC and ERK phosphorylation101

LIST OF ABBREVIATIONS

2D	Two-dimensional
3D	Three-dimensional
AR	Aspect Ratio
ARS	Alizarin Red S Stain
BMI	Body mass index
BP	Bisphosphonates
BSE	Backscattered electrons
BV/TV	Bone Volume Fraction
CO	Calcium oxalate
CXCR4	C-X-C chemokine receptor type 4
DCIS	Ductal carcinoma <i>in situ</i>
DMEM	Dulbecco's Modified Eagle Media
ECM	Extracellular matrix
EDTA	Ethylenediaminetetraacetic acid
EMT	Epithelial-mesenchymal transition
ERK	Extracellular signal-regulated kinases
ER	Estrogen receptor
FBS	Fetal bovine serum
Fn	Fibronectin
HA	Hydroxyapatite
HER2	Human epidermal growth factor receptor 2
IBC	Invasive Breast Cancer
IDC	Invasive Ductal Carcinoma
IGF-1	Insulin-like growth factor 1
IHC	Immunohistochemistry
IL-8	Interleukin-8
ILC	Invasive lobular carcinoma
LCIS	Lobular carcinoma <i>in situ</i>
LOX	Lysyl oxidase

MC	Microcalcification
MF	Morphology Factor
N.Oc/B.pm	Osteoclast number normalized to bone perimeter
OI	Osteogenesis Imperfecta
PLG	Poly(lactide-co-glycolide)
PR	Progesterone receptor
PMMA	Polymethylmethacrylate
RANKL	Receptor activator of nuclear factor kappa-B ligand
RGD	Arginylglycylaspartic acid
qRT-PCR	Quantitative real-time polymerase chain reaction
SAXS	Small angle X-ray scattering
SDF-1	Stromal cell-derived factor 1
SEM	Scanning electron microscopy
Tb.Sp	Trabecular separation
Tb.Th	Trabecular thickness
TCM	Tumor conditioned media
TGF- β	Transforming growth factor beta
TRAP	Tartrate-resistant acid phosphatase
μ CT	Microcomputed tomography
WAXS	Wide angle X-ray scattering

CHAPTER 1: INTRODUCTION

1.1 Hydroxyapatite mineral and bone metastatic breast cancer

Breast cancer is the most frequently diagnosed cancer in women worldwide (1). In the United States, improvements in detection and treatment have increased the 5-year survival rate for breast cancer to over 95% when detected at the earliest stages (2). However, the 5-year survival rate drops to 83% for patients diagnosed with regional spread and to only 26% for those with distant metastases (3). Advances in genomics have yielded insight into the molecular profiles of breast tumors and have resulted in the development of targeted therapies against certain oncogenic drivers such as the estrogen receptor (ER) and human epidermal growth factor receptor-2 (HER2) (4). Still, these therapeutic options are limited and do not address bone metastatic disease, which occurs in 80% of advanced breast cancer patients and represents their main cause of death (5). Current clinical treatments for breast cancer bone metastasis are palliative at best and mean survival time remains at a dismal two-years post diagnosis (6). These grim statistics reflect an insufficient mechanistic understanding of this disease and may be due to limitations of traditional approaches used to perform breast cancer research.

The vast majority of the research efforts thus far have been focused on the cellular and biochemical mechanisms that govern the bone metastatic capability of breast cancer cells (6–8). Studies now demonstrate that components of the extracellular matrix (ECM) also drive cancer pathogenesis and may be just as essential as genetic drivers (9). For breast cancer, matrix proteins

*Certain text and images adapted from **1.** He F, Choi SY, Estroff LA, Fischbach C (2017) Mineralized 3D Culture Systems for Studying Bone Metastatic Breast Cancer. *Engineering 3D Tissue Test Systems*, ed Burg K. (Taylor and Francis Group), pp 169-191; **2.** Chiou AE, Fischbach C (2018) Tissue-Engineered Models for Studies of Bone Metastasis. *Tumor Organoids*, ed Soker S. (Springer International Publishing AG), pp 95-116; **3.** Gamsjaeger S, Kazanci M, EP P, Fratzl P (2009) Raman Application in Bone Imaging. *Raman Spectroscopy for Soft Matter Applications*, ed Maher S. Amer (John Wiley & Sons, Inc), pp 227-267.

such as collagen, fibronectin, laminins, and proteoglycans have been shown to play a major functional role in breast cancer progression and metastasis (10). However, the role of hydroxyapatite $[(Ca_{10}(PO_4)_{6-x}(CO_3)_x(OH)_2)]$ (HA), a mineral component embedded within the ECMs of both the primary and bone metastatic sites of breast cancer (Fig. 1.1), is almost completely unknown. *In vitro* studies have indicated that HA is a bioactive material that modulates key features of cancer cell aggressiveness, including migration (11) and secretion of tumorigenic chemokines (12–14). Hence, it is possible that HA may play a role in the progression from primary breast cancer to bone metastatic disease. However, the underlying mechanisms remain unclear.

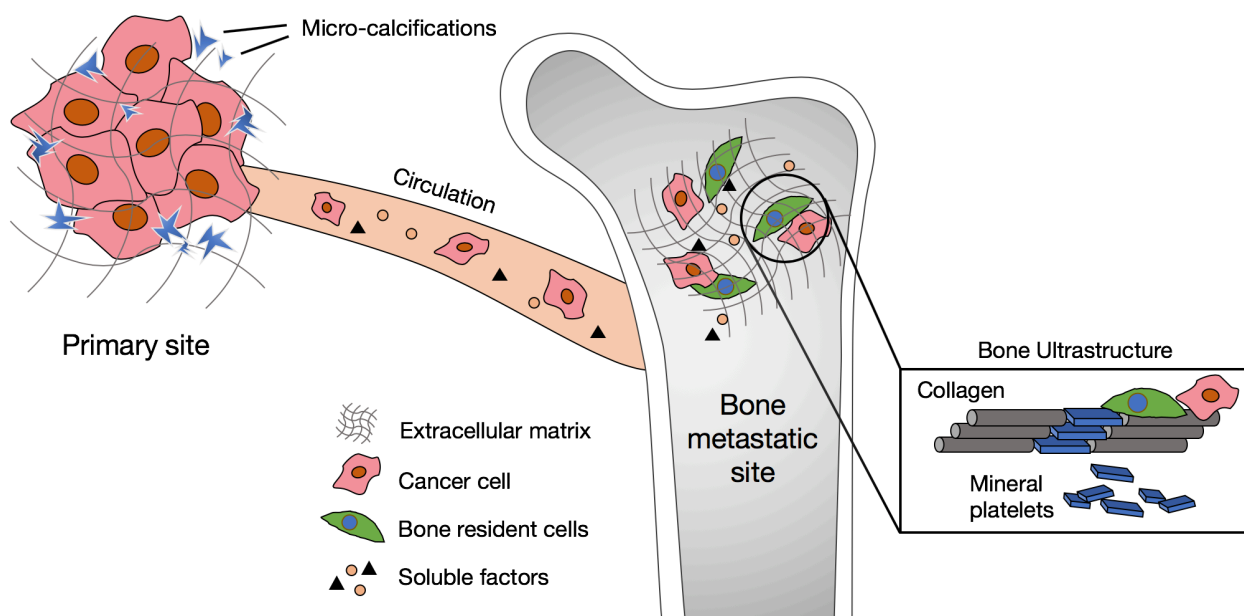


Figure 1.1: Mineralized microenvironments in the primary and secondary bone site of breast cancer. Hydroxyapatite (HA) mineral is a unique feature of both the primary site and secondary bone site in metastatic breast cancer. Mammary microcalcifications composed of HA are frequently associated with malignant disease. Tumor cells disseminated to the skeleton will interact with the bone mineralized extracellular matrix, which is composed of nanocomposite material of collagen fibrils and mineral platelets. Adapted from Chiou AE, Fischbach C (2018) Tissue-Engineered Models for Studies of Bone Metastasis. *Tumor Organoids*, ed Soker S. (Springer International Publishing AG), pp 95-116.

Thus, the overall goal of this work was to investigate the relevance of HA mineral to bone metastatic disease within mineralized microenvironments unique to the metastatic cascade of breast cancer. To this end, innovative, interdisciplinary approaches were pursued. Specifically, techniques from tissue engineering and materials science were integrated with cell biology and animal models. This introductory chapter will summarize current knowledge of the tumor-mineral interactions pertinent to this disease, and then describe physical sciences approaches to 1) functionally interrogate cell-mineral interactions and 2) characterize physicochemical and structural properties of HA in the bone mineralized ECM.

1.2 Mineralized microenvironments of the breast cancer-bone metastasis cascade

Breast carcinomas typically arise within the inner lining of the milk ducts or lobules of the mammary tree, with ductal breast cancers accounting for 80% of all breast cancer diagnoses (15). Ductal carcinomas *in situ* (DCIS) is defined as a premalignant proliferation of neoplastic epithelial cells within the confines of the mammary ducts (16) and is considered the precursor lesion to most invasive carcinomas (17). Microcalcifications (MCs), or small calcium mineral deposits, have been detected via mammographic screening techniques in the vast majority of DCIS patients (18). They typically present as white spots or flecks on a mammogram (19) and those that consist of HA mineral are frequently associated with malignant disease (20, 21). Although *in vitro* studies show that HA may be pro-tumorigenic (11–14), MCs are still treated as passive indicators of disease in clinical settings (19). Given the ubiquitous presence of microcalcifications in DCIS and the bioactive nature of HA, one could hypothesize that interactions between tumor cells and microcalcifications in the breast tissue could stimulate progression of DCIS to invasive cancer.

Meanwhile, metastasis of breast cancer to the skeleton is an osteolytic disease that is known to dramatically interfere with the bone remodeling process, resulting in bone that experiences

severe degradation during its most advanced forms (6–8). Identifying the multifactorial interactions between breast cancer cells and the bone microenvironment is critical to elucidating the pathogenesis of skeletal metastasis, yet little is known about the nature of tumor cell-bone ECM interactions during the different stages of breast cancer. The mineralized ECM of bone is structurally complex, consisting of a fractal-like hierarchical organization based on a nanocomposite of collagen fibrils and HA particles, with mineral accounting for 67% of its dry weight (22). Conceivably, to facilitate the establishment of a secondary bone tumor, favorable interactions between tumor cells and bone mineral HA may be necessary. Interestingly, emerging evidence suggests that nanoscale variations in HA materials properties may in fact regulate secondary tumor formation. Previous studies with mineral-containing cell culture systems have suggested that breast cancer cell adhesion, proliferation and osteolytic factor expression are mediated by the materials properties of HA nanoparticles (12, 14, 23). However, as nanoscale bone mineral properties have not been previously measured in sites of breast cancer metastasis, it remains unresolved whether these *in vitro* observations are physiologically relevant. Characterization of bone mineral properties at sites of metastasis in different stages of breast cancer could inform the development of mineralized culture models to study this disease.

1.2.1 Relationships between mammary calcifications and cancer

Breast MCs are pathological mineral deposits that have been used for diagnosing early stage, non-palpable breast cancer in routine mammographic screenings (24–26) (Fig. 1.2a). Nearly 93% of DCIS (18) and 40% of mammary carcinomas (25) present radiologically detectable mineral deposits, the shape, size, distribution, and density of which can be further used to predict the level

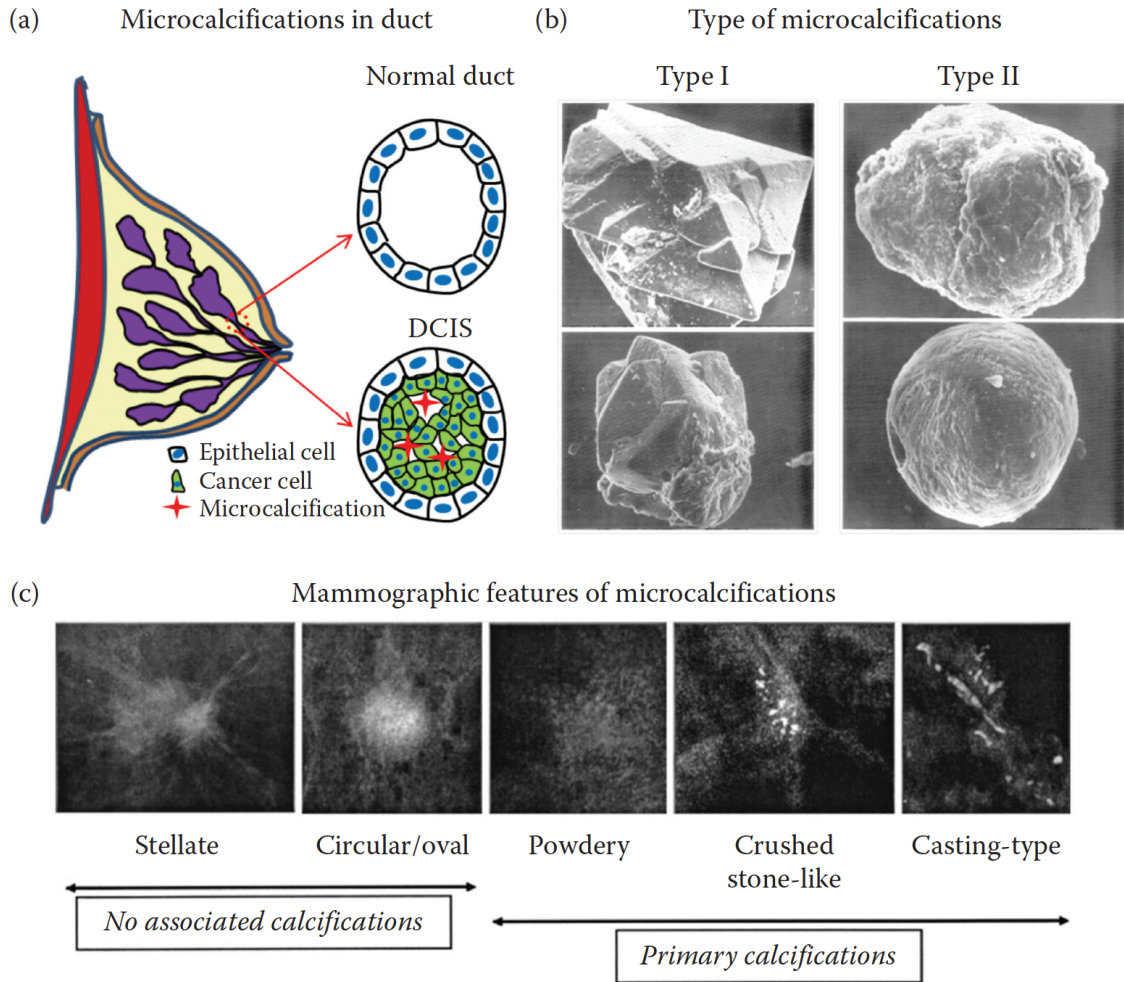


Figure 1.2: Mammary microcalcifications. (a) Microcalcifications are most frequently detected in ductal carcinoma in situ (DCIS) when cancerous cells fill the lumen of mammary ducts and mineral deposits develop due in part to cell death. (b) Scanning electron microscopy images. Left panels show type I microcalcification of a sclerocystic mastopathy (top) and of an *in situ* lobular carcinoma (bottom). Right panels show type II microcalcification in an infiltrating adenocarcinoma of the breast with irregular (top) and smooth surface (bottom). (c) Mammographic descriptors of breast microcalcifications. Adapted from He F, Choi SY, Estroff LA, Fischbach C (2017) Mineralized 3D Culture Systems for Studying Bone Metastatic Breast Cancer. *Engineering 3D Tissue Test Systems*, ed Burg K. (Taylor and Francis Group), pp 169-191.

of breast cancer malignancy (19, 27, 28). While the vast majority of detected MCs are benign, it has been established that certain clustering patterns and morphologies implicate different subtypes or invasive grades of malignant disease. For instance, benign MCs typically have a scattered distribution and are coarser with smooth margins, whereas malignant MCs typically have a

clustered, pleomorphic appearance and are finer with linear branching patterns (29) (Fig. 1.2c). Moreover, breast cancer patients with MCs exhibit decreased survival and increased lymph node involvement (25), suggesting their correlation with a more aggressive phenotype.

Mammary MCs classify into two distinct subgroups and can be distinguished by differences in structure and composition (20, 30). Type I MCs exhibit pronounced crystalline structures and are predominantly composed of calcium oxalate dihydrate ($\text{CaC}_2\text{O}_4 \cdot 2\text{H}_2\text{O}$) (CO) (20), while type II MCs are composed of poorly defined, heterogeneous structures and consist mainly of HA (30) (Fig. 1.2b). Interestingly, CO has been strictly found in benign growths (20, 25, 31, 32), but HA is commonly associated with more invasive disease (20, 21). Furthermore, variations of HA composition (e.g. carbonate substitution of HA) may be used to assess the malignant potential of breast cancer. More specifically, breast MCs with decreased carbonate content may be linked with more aggressive disease relative to their more carbonated counterparts, implicating that compositional variations of MCs may serve as prognostic indicators (21, 33).

Although the exact mechanisms underlying the genesis of breast MCs are unclear, experimental evidence implicates synergistic interactions between mammary tumor cells and their surrounding microenvironments. It has traditionally been thought that the more crystalline type I MCs are formed through cell secretions, whereas the aggregated type II MCs result from cellular degeneration and necrosis (21, 29, 31). However, similar to deposition mechanisms of vascular and other pathological calcifications, the formation of HA in breast tissue could also be due to active cell-mediated processes (34). Indeed, Cox et al. have suggested that tumor cells themselves can deposit HA (11), but other cell types may play a similarly important role. For example, not only are bone marrow-derived mesenchymal stem cells actively recruited by tumors, but they can also spontaneously calcify (35, 36). In particular, morphogens released by activated immune cells may play a role in this process (37). In addition to the cells, mammary tumors contain appreciable

levels of ECM components known to play a key role in mineral formation, such as bone sialoprotein, an RGD-containing phosphoprotein known to initiate HA deposition (38), and osteopontin (38, 39), an inhibitor of ectopic calcification depending on its phosphorylation state (40, 41).

1.2.2 Bone mineral properties and relevance to metastasis

In bone, mineral occurs in the form of HA platelets that are embedded into collagen fibrils (Fig. 1.3a). The composite of collagen fibrils and co-aligned HA mineral platelets composes the fundamental building block of bone (42, 43) and thus, influences bone hierarchical structure and mechanical performance (22, 44–47). This collagen-mineral arrangement optimizes the toughness of the protein with the stiffness of the mineral to provide both rigidity and resistance against fracture. Should the geometric arrangement or integrity of each of these two components be altered in some way, the mechanical performance of bone tissue would be compromised (48). Relatively little is known currently about the modulating effect of breast cancer bone metastasis on bone mineral properties. However, a number of related findings indeed suggest that bone mineral changes in the presence of breast cancer cells and should thus, be considered when studying bone metastasis.

Clinical studies causally associate high bone turnover with cancer metastasis, and inhibiting bone resorption can prevent the growth of tumor cells in the bone (49). After homing to bone, breast cancer cells release factors that cause visible degradation in bone structure (3, 7, 8). In animal models of bone metastasis these osteolytic lesions most frequently occur in the proximal

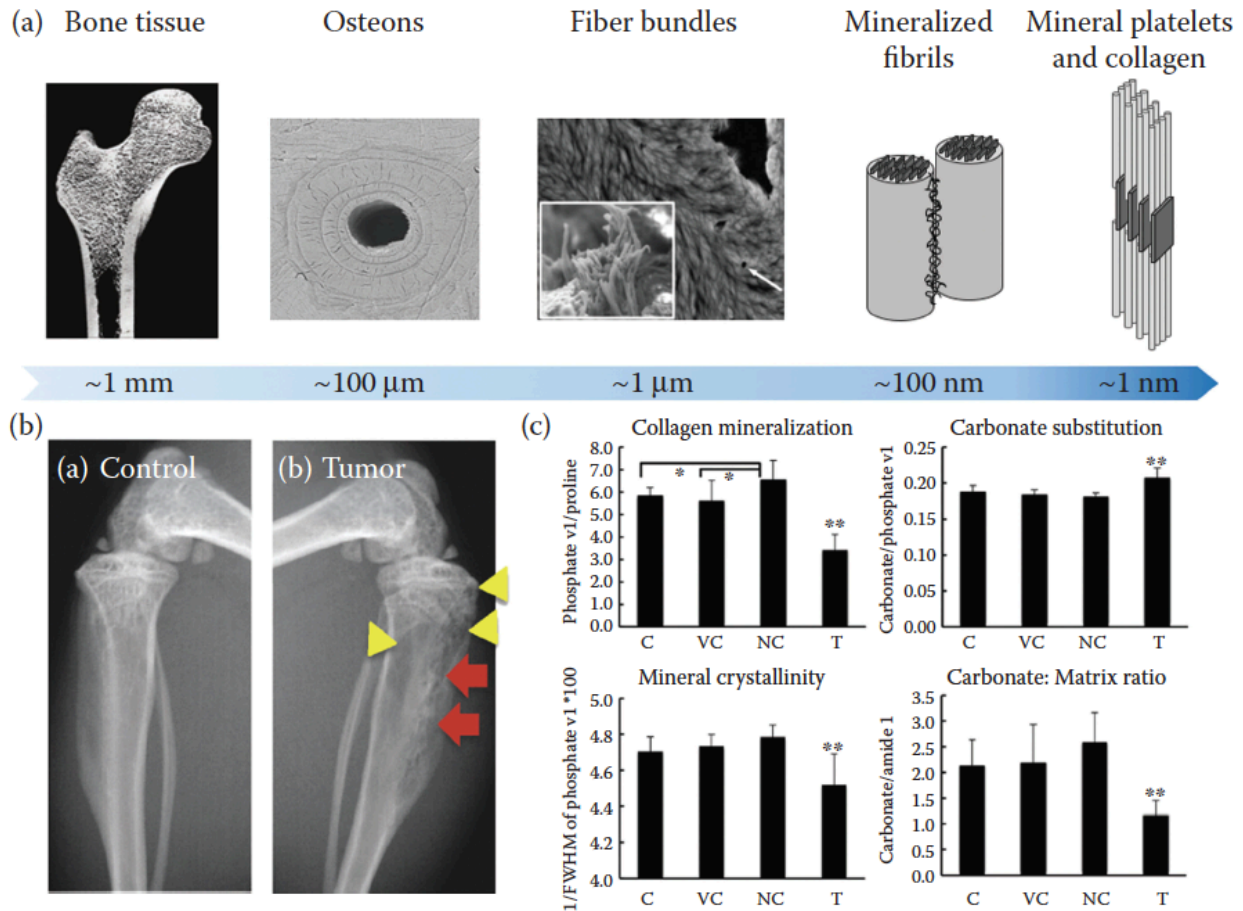


Figure 1.3: Bone structure is affected by cancer metastasis. (a) Hierarchical structure of mammalian bone. Important features are shown at the progressively decreasing length scales from left to right. (b) Prostate cancer metastasis engenders large lesions in the proximal tibiae. Yellow and red arrows indicate osteolytic and osteoblastic lesions, respectively. (c) Raman spectroscopy reveals that collagen mineralization, carbonate substitution, mineral crystallinity, and carbonate: matrix ratio is significantly affected by the bone metastasis shown in (b). C, VC, NC, and T indicate the contralateral control, vehicle injection control, noninjection control, and tumor conditions, respectively. Adapted from He F, Choi SY, Estroff LA, Fischbach C (2017) Mineralized 3D Culture Systems for Studying Bone Metastatic Breast Cancer. *Engineering 3D Tissue Test Systems*, ed Burg K. (Taylor and Francis Group), pp 169-191.

tibiae and in the distal femurs (50–52) and have been attributed to breast cancer cell-associated activation of the bone cell-controlled RANKL pathway (8). However, RANKL independent osteolytic mechanisms via interleukin 8 (IL-8) signaling (53, 54) and lysyl oxidase (LOX) (55) can also contribute to bone degradation. While little is known about whether and how breast tumors change HA in the bone, it has been shown for prostate cancer that the metastasized tumor

engenders significant changes in the collagen mineralization, carbonate substitution, mineral crystallinity, and carbonate:matrix ratio (56), significantly disrupting the nano- and micro-scale integrity of bone structure (Fig. 1.3c). Interestingly, recent experimental evidence suggests that breast tumors may be able to significantly modulate bone structure even in the absence of skeletal metastasis (55, 57). These data implicate that remotely located mammary cancer cells release factors into the circulation (e.g. growth factors, exosomes (58)) that cause pre-metastatic remodeling of the bone niche, ultimately enhancing tumor cell homing (55). How this increased bone homing relates to bone HA and the tumor-mediated changes in its properties remains to be demonstrated.

Indeed, other pathologies such as osteogenesis imperfecta (OI), osteoporosis, pycnodysostosis, and fluorosis have been shown to worsen bone quality by altering the mineral-collagen structural composite (59, 60). Osteogenesis imperfecta, a condition characterized by highly brittle bone (61), is a particularly well-studied example of how bone disease influences mineral nanostructure. Notably, the collagen fibrils in OI (oim/oim) mice exhibit only half the mechanical strength as those from control mice (62), which could be explained by abnormal collagen mineralization patterns: some regions of bone do not exhibit any mineralization (63), whereas others are over-mineralized and are comprised of abnormally thin and variably aligned particles (63–66). Osteogenesis imperfecta bones also exhibit changes in mineral crystallinity (67), collagen cross-links (67, 68), and collagen fibril diameters (69). Thorough characterization studies like these have not yet been performed on breast cancer-associated bone mineral and collagen fibrils. Yet such studies could inform the design of experimental culture models incorporating relevant mineral particle characteristics to investigate their influence on tumor cell behavior and signaling.

1.3 Investigating cell-mineral interactions using engineered culture models

Studies in standard two-dimensional (2D) cell culture have significantly increased our understanding of signaling mechanisms relevant to cancer (70). However, 2D cultures typically fail to mimic the complex microenvironmental conditions that influence disease progression in patients. Indeed, increasing culture dimensionality from 2D to 3D has been shown to significantly alter cell protein expression (71, 72), proliferation (73), differentiation (74), and metabolism (75). In addition, many other microenvironmental components such as the surrounding extracellular matrix (ECM), other neighboring cells, and cytokine gradients have been recapitulated with engineered model systems and revealed novel insights (76).

To directly interrogate cell-mineral interactions, synthetic approaches may enable the most amount of experimental control and reproducibility. For example, HA can be incorporated into porous scaffolds that consist of biodegradable polymers (e.g. poly(lactide-co-glycolide) [PLG]). Such constructs permit control over scaffold architecture and improved mechanical performance while enabling cellular organization into 3D tissue-like structures (71, 77). Being able to modulate scaffold micro-architecture is not only important for the essential transport of oxygen and nutrients, but also for the control of cell proliferation and migration, which are dependent on pore diameter and shape (78, 79). Additionally, differences in scaffold micro-architecture may influence cell shape, which can regulate many different cellular features relevant to bone metastasis including human mesenchymal stem cell differentiation (80) and geometry-dependent cell growth and viability (81). Mineral can be introduced into PLG-based systems by the incorporation of HA nanoparticles during their fabrication by a gas foaming/particulate leaching technique (13, 14) (Fig. 1.4). Using this approach, it was previously demonstrated that the behavior of breast cancer cells changes in the presence of HA and that introduction of mechanical stimulation further alters their gene expression (82). Moreover, culturing breast cancer cells on

PLG scaffolds containing synthetic HA nanoparticles of varying chemical and physical properties has shown that HA size and crystallinity regulates tumor cell adhesion, proliferation, and osteolytic factor secretion (14).

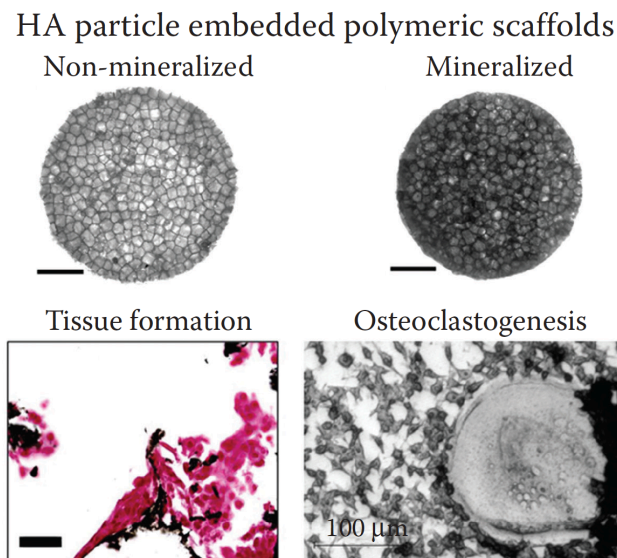


Figure 1.4: HA-containing polymeric scaffolds. Three-dimensional mineral-containing PLG scaffolds can be fabricated by incorporating HA nanoparticles during the fabrication process. When seeded with breast cancer cells, HA-containing scaffolds enable coherent tissue formation (pink) around HA particles (black, von Kossa stained), and conditioned media collected from HA-containing tumor-cell cultures induce osteoclastogenesis relative to media from cultures without HA. Adapted from He F, Choi SY, Estroff LA, Fischbach C (2017) Mineralized 3D Culture Systems for Studying Bone Metastatic Breast Cancer. *Engineering 3D Tissue Test Systems*, ed Burg K. (Taylor and Francis Group), pp 169-191.

1.4 Materials characterization of HA in mineralized tissues

Structural studies of mineralized tissues typically employ a combination of techniques to capture information over a large range of length scales. Techniques such as X-ray scattering (83–88) and Raman spectroscopy (89–92) can reveal structural and physicochemical information on HA mineral with nanometer resolution. To account for spatial heterogeneity of mineralized tissues (48), these instruments can be programmed to scan larger micrometer-scale regions of interest. Importantly, these methods are non-destructive to mineralized tissues. Thus, the obtained data can then be mapped onto imaging information obtained from techniques such as micro-computed

tomography (μ CT), scanning electron microscopy (SEM), and histological staining, which provide information at the greater length scales necessary for physiological context. Having this context is particularly important when interpreting data obtained from either human patient samples or in the case of this thesis work, animal models of metastatic cancer (chapter 3). The following subsections will provide a brief description of how X-ray scattering and Raman imaging has been used in the materials analyses of mineralized tissue, especially with regards to bone.

1.4.1 X-ray scattering

X-ray scattering is considered the gold standard technique for the analysis of bone mineral nanostructure and has greatly contributed to the understanding of bone biomineralization (48). When highly collimated X-rays pass through the experimental specimens, they scatter and produce patterns of light that register on a 2D detector. These scattering patterns can then be used to derive nanoscale information about mineral crystal size and degree of alignment (83, 86) (Fig. 1.5). This technique has been routinely used to characterize HA nanocrystal structure across a range of organisms – including humans, mice, rats, baboons, minipigs, and turkeys (48) – and has shown that even small variations in nanoscale properties are linked to pathological conditions (59).

One important consideration during the design of an X-ray scattering experiment is the X-ray source (86). X-rays can be generated from common laboratory equipment, yielding a 150-200 μ m-sized beam at the sample – appropriate for scanning regions of interest that have larger, millimeter-scale dimensions. Standard small-angle X-ray (SAXS) analysis, which provides information on average bone mineral crystal thickness (T-parameter) and orientation (ρ -parameter), is achievable with this setup. However, to perform higher resolution analysis, access to a synchrotron beamline is necessary. X-rays generated from a synchrotron-source will possess a smaller beam diameter and a greater beam flux. In addition to SAXS, the use of the synchrotron

would also enable the simultaneous collection of the wide-angle X-ray scattering (WAXS) data. This would further enable the calculation of bone mineral crystal length (L-parameter) data. However, the increased resolution may limit reasonable data collection to smaller, more defined regions of interest.

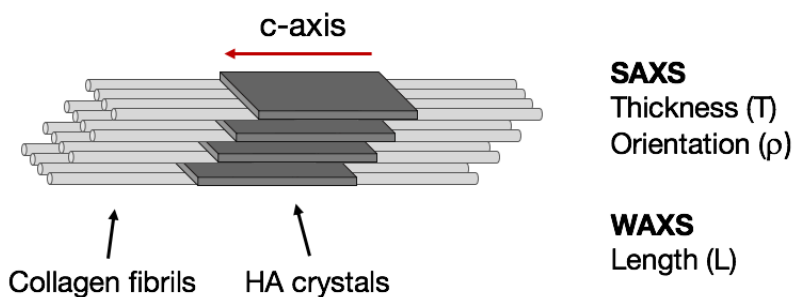


Figure 1.5: Characteristics of bone mineral nanostructure obtained via X-ray scattering. Hydroxyapatite nanoparticles (2-4 nm in thickness) are typically aligned with collagen fibrils, with the crystalline c-axis represented by the red arrow. Hydroxyapatite nanostructural parameters (T , ρ , L) derived from small-angle X-ray scattering (SAXS) and wide-angle X-ray scattering (WAXS) are shown to the right of the bone nanocomposite schematic, which is not drawn to scale.

1.4.2 Raman Imaging

Raman spectroscopy is a vibrational spectroscopy technique used to assess patterns of scattered light from small molecules (60). A sample is irradiated with a monochromatic laser, resulting in an extremely small amount (\sim one in 10^7 photons) of Raman scattered light (93). A charge-coupled device detector will then translate the scattered light into a Raman spectrum, which represents the scattered light intensity plotted against its wavelength difference from the incident light (94). These characteristic frequency (or Raman) shifts can be used in the identification and characterization of specific moieties within biological materials. This technique is sensitive to changes in molecular structure and composition (56) and offers superior spatial resolution of 0.5-1.0 μm (89).

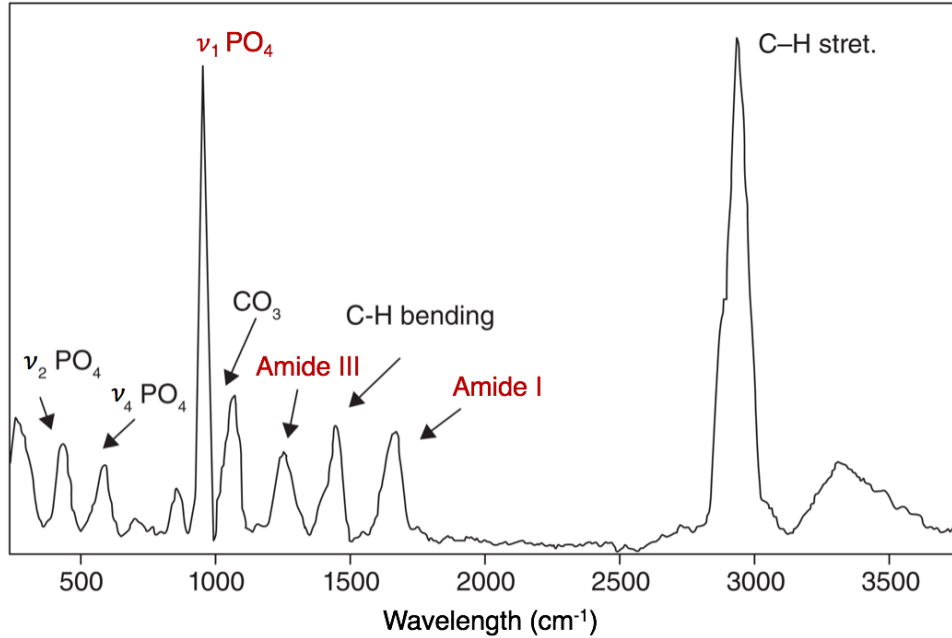


Figure 1.6: A typical Raman spectrum of bone. Raman peaks used in this study are highlighted in red. Adapted from Gamsjaeger S, Kazanci M, EP P, Fratzl P (2009) Raman Application in Bone Imaging. *Raman Spectroscopy for Soft Matter Applications*, ed Maher S. Amer (John Wiley & Sons, Inc), pp 227-267.

As such, Raman has emerged as a versatile technique to assess the compositional and structural qualities of mineralized tissues such as bone (89). A typical Raman spectrum of bone will consist of a strong phosphate ($\nu_1\text{PO}_4$) band at 960 cm^{-1} , otherwise known as the apatite peak, and several bands associated with collagen, including amide III at 1256 cm^{-1} and amide I at 1677 cm^{-1} (95) (Fig. 1.6). Although Raman spectroscopy is not considered a quantitative technique, it can provide supporting data on bone mineral nanostructure from an alternative spectroscopic perspective. For example, the width of the $\nu_1\text{PO}_4$ band can be used to calculate crystallinity, which is a measure of mineral maturity that is strongly correlated with stoichiometrical perfection and the length of the HA crystals along their c-axes (96). Importantly, Raman imaging enables a more complete understanding of the bone ECM because it is especially sensitive to changes in collagen composition. The intensities of the amide peaks correlate to collagen content, though proper analysis would require that the polarization-dependent amide I and polarization-independent

amide III peaks show the same trends to verify that the orientation of the incident beam is not a confounding variable (89, 95). Other measures of bone quality can be derived from relative peak intensities. One particularly relevant parameter is the ratio of the $\nu_1\text{PO}_4$ and amide I peak integrated areas (mineral-to-matrix ratio) (60, 89, 94), which, unlike measures of bone mineral density from dual-energy X-ray absorptiometry or μCT , accounts for both the mineral and organic phases of the bone ECM (60). Collectively, these Raman-based measurements strongly complement the quantitative parameters of bone mineral nanostructure obtained through X-ray scattering analyses.

1.5 Research Objectives

For breast cancer, HA mineral is a unique component of the extracellular matrix at both the primary tumor site and the secondary bone site. Interactions between breast cancer cells and mineral may be critical to disease progression yet the nature of these interactions and how they could impact malignancy is not clear. Studies to date lack the appropriate methodologies to address these unresolved questions in a controlled, pathologically-relevant manner. Thus, this dissertation describes efforts to employ state-of-the-art tissue engineering and materials science techniques to investigate tumor cell-mineral interactions within different stages of the breast cancer-bone metastasis cascade in both *in vitro* and *in vivo* models. Specifically, this work addressed two sub-hypotheses:

1) Hydroxyapatite mineral actively promotes malignancy in preinvasive tumor lesions

Breast cancer cell responses to HA mineral were investigated using a 3D polymeric scaffold system engineered to present HA under dynamic culture conditions. To assess HA-mediated changes as a function of breast cancer progression, differences in tumor cell proliferation and IL-8 expression were assessed in a series of isogenic MCF10A-derived breast epithelial cell lines. MCF10.DCIS (DCIS) cells were then specifically used as a premalignant model for further

analysis of HA-mediated invasiveness. The DCIS cells were precultured in HA-scaffolds, then detached and assessed for changes in single cell shape and colony morphology using epifluorescence imaging of cells stained for nuclei and F-actin. Mineral-mediated changes in single cell motility were assessed by live tracking DCIS cells precultured in HA-scaffolds over the course of 24 hours. Inhibition studies with IL-8 antibody were then used to show IL-8 dependent effects of HA-mediated cell motility. To assess pathological relevance of the *in vitro* findings, DCIS tumor xenografts were initiated in HA scaffolds and compared to their PLG counterparts via histological analysis.

2) Advanced breast cancer cells remotely alter mineral properties in the bone metastatic site

Tibiae from healthy control mice, mice carrying mammary tumors, and mice with overt bone metastasis were analyzed with a set of complementary techniques to assess mineral properties in the bone metastatic site. BoM1-2287, a bone metastatic subline of MDA-MB-231 isolated through an *in vivo* selection process (50), was used in different surgical procedures in immune-compromised mice to establish a controlled set of xenograft models. Bone metastasis was achieved by intracardially injecting luciferase-labeled BoM1-2287 cells, while localized mammary tumors resulted from implanting the same cells into cleared mammary fat pads. Mouse tibiae harvested after 5 to 7 weeks were embedded in polymethylmethacrylate and subjected to μ CT, histological analyses, and backscattered SEM to assess macro- to micro- scale changes in bone structure. SAXS/WAXS as well as Raman imaging was used to bone nanostructure and physicochemical composition. To assess whether changes in bone mineral could be mediated by tumor-derived soluble factors, immune-compromised mice were systemically conditioned with daily intraperitoneal injections of tumor-conditioned media (TCM) over the course of 3 weeks; tibiae were then harvested and analyzed for markers of bone matrix remodeling. The osteogenic potential

of this TCM was assessed by calcium staining bone marrow-derived mesenchymal stem cells cultured in it for 3 weeks.

1.6 References

1. Jemal A, Bray F, Ferlay J (1999) Global Cancer Statistics: 2011. *CA Cancer J Clin* 49(2):1,33-64.
2. Siegel RL, Miller KD, Jemal A (2018) Cancer statistics, 2018. *CA Cancer J Clin* 68(1):7–30.
3. Kingsley LA, Fournier PGJ, Chirgwin JM, Guise TA (2007) Molecular Biology of Bone Metastasis. *Mol Cancer Ther* 6(10):2609–2617.
4. Arnedos M, et al. (2015) Precision medicine for metastatic breast cancer-limitations and solutions. *Nat Rev Clin Oncol* 12(12):693–704.
5. Coleman RE, Rubens RD (1987) The clinical course of bone metastases from breast cancer. *Br J Cancer* 55(1):61–66.
6. Kozlow W, Guise TA (2005) Breast cancer metastasis to bone: Mechanisms of osteolysis and implications for therapy. *J Mammary Gland Biol Neoplasia* 10(2):169–180.
7. Weilbaecher KN, Guise TA, McCauley LK (2011) Cancer to bone: A fatal attraction. *Nat Rev Cancer* 11(6):411–425.
8. Mundy GR (2002) Metastasis to bone: Causes, consequences and therapeutic opportunities. *Nat Rev Cancer* 2(8):584–593.
9. Bissell MJ, Hines WC (2011) Why don't we get more cancer? A proposed role of the microenvironment in restraining cancer progression. *Nat Med* 17(3):320–329.
10. Insua-Rodríguez J, Oskarsson T (2016) The extracellular matrix in breast cancer. *Adv Drug Deliv Rev* 97:41–55.
11. Cox RF, et al. (2012) Microcalcifications in breast cancer: Novel insights into the molecular mechanism and functional consequence of mammary mineralisation. *Br J Cancer* 106(3):525–537.
12. Choi S, Coonrod S, Estroff L, Fischbach C (2015) Chemical and physical properties of carbonated hydroxyapatite affect breast cancer cell behavior. *Acta Biomater* 24:333–342.
13. Pathi SP, Kowalczewski C, Tadipatri R, Fischbach C (2010) A novel 3-D mineralized tumor model to study breast cancer bone metastasis. *PLoS One* 5(1):1–10.
14. Pathi SP, Lin DDW, Dorvee JR, Estroff LA, Fischbach C (2011) Hydroxyapatite nanoparticle-containing scaffolds for the study of breast cancer bone metastasis. *Biomaterials* 32(22):5112–5122.
15. McSherry EA, Donatello S, Hopkins AM, McDonnell S (2007) Molecular basis of

- invasion in breast cancer. *Cell Mol Life Sci* 64(24):3201–3218.
16. Cowell CF, et al. (2013) Progression from ductal carcinoma in situ to invasive breast cancer: Revisited. *Mol Oncol* 7(5):859–869.
 17. Espina V, Liotta LA (2011) What is the malignant nature of human ductal carcinoma in situ? *Nat Rev Cancer* 11(1):68–75.
 18. Hofvind S, et al. (2011) Mammographic morphology and distribution of calcifications in ductal carcinoma in situ diagnosed in organized screening. *Acta radiol* 52(5):481–487.
 19. Tse GM, Tan PH, Pang ALM, Tang APY, Cheung HS (2008) Calcification in breast lesions: Pathologists' perspective. *J Clin Pathol* 61(2):145–151.
 20. Frappart L, et al. (1987) Different types of microcalcifications observed in breast pathology - Correlations with histopathological diagnosis and radiological examination of operative specimens. *Virchows Arch A Pathol Anat Histopathol* 410(3):179–187.
 21. Haka AS, et al. (2002) Identifying Microcalcifications in Benign and Malignant Breast Lesions by Probing Differences in Their Chemical Composition Using Raman Spectroscopy Identifying Microcalcifications in Benign and Malignant Breast Lesions by Probing Differences in Their Che. 5375–5380.
 22. Reznikov N, Bilton M, Lari L, Stevens MM, Kröger R (2018) Fractal-like hierarchical organization of bone begins at the nanoscale. *Science (80-)* 360(6388):eaao2189.
 23. Wu F, et al. (2017) Protein-crystal interface mediates cell adhesion and proangiogenic secretion. *Biomaterials* 116:174–185.
 24. Hansen R, Angelsen BAJ (2009) SURF Imaging for Contrast Agent Detection. *IEEE Trans Ultrason Ferroelectr Freq Control* 56(2):280–290.
 25. Morgan MP, Cooke MM, McCarthy GM (2005) Microcalcifications associated with breast cancer: An epiphenomenon or biologically significant feature of selected tumors? *J Mammary Gland Biol Neoplasia* 10(2):181–187.
 26. Bazin D, Daudon M, Combes C, Rey C (2012) Characterization and some physicochemical aspects of pathological microcalcifications. *Chem Rev* 112(10):5092–5120.
 27. Stomper PC, Geradts J, Edge SB, Levine EG (2003) Mammographic Predictors of the Lesions Without a Mass. *Medicine (Baltimore)* 181(December):1679–1684.
 28. Tabar L, et al. (2004) Mammographic tumor features can predict long-term outcomes reliably in women with 1-14-mm invasive breast carcinoma: Suggestions for the reconsideration of current therapeutic practice and the TNM classification system. *Cancer* 101(8):1745–1759.

29. Muttarak M, Kongmebhol P, Sukhamwang N (2009) Breast calcifications: Which are malignant? *Singapore Med J* 50(9):907–914.
30. Frappart L, et al. (1984) Structure and composition of microcalcifications in benign and malignant lesions of the breast: Study by light microscopy, transmission and scanning electron microscopy, microprobe analysis, and X-ray diffraction. *Hum Pathol* 15(9):880–889.
31. Büsing CM, Keppler U, Menges V (1981) Differences in microcalcification in breast tumors. *Virchows Arch A Pathol Anat Histol* 393(3):307–313.
32. Sharma T, Radosevich JA, Pachori G, Mandal CC (2016) A Molecular View of Pathological Microcalcification in Breast Cancer. *J Mammary Gland Biol Neoplasia* 21(1–2):25–40.
33. Baker R, Rogers KD, Shepherd N, Stone N (2010) New relationships between breast microcalcifications and cancer. *Br J Cancer* 103(7):1034–1039.
34. Cox RF, Morgan MP (2013) Microcalcifications in breast cancer: Lessons from physiological mineralization. *Bone* 53(2):437–450.
35. Yoon Y-S (2004) Unexpected Severe Calcification After Transplantation of Bone Marrow Cells in Acute Myocardial Infarction. *Circulation* 109(25):3154–3157.
36. Breitbach M, et al. (2007) Potential risks of bone marrow cell transplantation into infarcted hearts. *Hematology* 110(4):1362–1369.
37. Abedin M, Tintut Y, Demer LL (2004) Vascular calcification: Mechanisms and clinical ramifications. *Arterioscler Thromb Vasc Biol* 24(7):1161–1170.
38. Bellahcène A, Castronovo V, Ogbureke KUE, Fisher LW, Fedarko NS (2008) Small integrin-binding ligand N-linked glycoproteins (SIBLINGs): Multifunctional proteins in cancer. *Nat Rev Cancer* 8(3):212–226.
39. Bellahcène A, Castronovo V (1995) Increased expression of osteonectin and osteopontin, two bone matrix proteins, in human breast cancer. *Am J Pathol* 146(1):95–100.
40. Gericke A, et al. (2005) Importance of phosphorylation for osteopontin regulation of biomineralization. *Calcif Tissue Int* 77(1):45–54.
41. Addison WN, Masica DL, Gray JJ, McKee MD (2010) Phosphorylation-dependent inhibition of mineralization by osteopontin ASARM peptides is regulated by PHEX cleavage. *J Bone Miner Res* 25(4):695–705.
42. Landis WJ, Song MJ, Leith A, McEwen L, McEwen BF (1993) Mineral and organic matrix interaction in normally calcifying tendon visualized in three dimensions by high-voltage electron microscopic tomography and graphic image reconstruction. *J Struct Biol*

- 110(1):39–54.
43. Traub W, Arad T, Weiner S (1992) Growth of mineral crystals in Turkey tendon collagen fibers. *Connect Tissue Res* 28(1–2):99–111.
 44. Weiner S, Traub W (1992) Bone structure: from angstroms to microns. *FASEB J* 6(3):879–885.
 45. Fratzl P, Weinkamer R (2007) Nature’s hierarchical materials. *Prog Mater Sci* 52(8):1263–1334.
 46. Pazzaglia UE, Congiu T, Marchese M, Spagnuolo F, Quacci D (2012) Morphometry and Patterns of Lamellar Bone in Human Haversian Systems. *Anat Rec* 295(9):1421–1429.
 47. Reznikov N, Shahar R, Weiner S (2014) Bone hierarchical structure in three dimensions. *Acta Biomater* 10(9):3815–3826.
 48. Fratzl P, Gupta HS, Paschalis EP, Roschger P (2004) Structure and mechanical quality of the collagen-mineral nano-composite in bone. *J Mater Chem* 14(14):2115–2123.
 49. Zheng Y, Zhou H, Dunstan CR, Sutherland RL, Seibel MJ (2013) The role of the bone microenvironment in skeletal metastasis. *J Bone Oncol* 2(1):47–57.
 50. Kang Y, et al. (2003) A multigenic program mediating breast cancer metastasis to bone. *Cancer Cell* 3(6):537–549.
 51. Zhang XHF, et al. (2009) Latent Bone Metastasis in Breast Cancer Tied to Src-Dependent Survival Signals. *Cancer Cell* 16(1):67–78.
 52. Mastro AM, Gay C V., Welch DR (2003) The skeleton as a unique environment for breast cancer cells. *Clin Exp Metastasis* 20(3):275–284.
 53. Bendre MS, et al. (2003) Interleukin-8 stimulation of osteoclastogenesis and bone resorption is a mechanism for the increased osteolysis of metastatic bone disease. *Bone* 33(1):28–37.
 54. Bendre MS, et al. (2005) Tumor-derived interleukin-8 stimulates osteolysis independent of the receptor activator of nuclear factor- κ B ligand pathway. *Cancer Res* 65(23):11001–11009.
 55. Cox TR, et al. (2015) The hypoxic cancer secretome induces pre-metastatic bone lesions through lysyl oxidase. *Nature* 522(7554):106–110.
 56. Bi X, et al. (2013) Prostate cancer metastases alter bone mineral and matrix composition independent of effects on bone architecture in mice - A quantitative study using microCT and Raman spectroscopy. *Bone* 56(2):454–460.

57. Thorpe MP, et al. (2011) Breast tumors induced by N-methyl-N-nitrosourea are damaging to bone strength, structure, and mineralization in the absence of metastasis in rats. *J Bone Miner Res* 26(4):769–776.
58. Peinado H, et al. (2012) Melanoma exosomes educate bone marrow progenitor cells toward a pro-metastatic phenotype through MET. *Nat Med* 18(6):883–891.
59. Fratzl P, Gupta HS, Roschger P, Klaushofer K (2009) Bone Nanostructure and its Relevance for Mechanical Performance, Disease, and Treatment. *Nanotechnology* (WILEY-VCH Verlag GmbH & Co), pp 345–360.
60. Gamsjaeger S, et al. (2014) Vibrational spectroscopic imaging for the evaluation of matrix and mineral chemistry. *Curr Osteoporos Rep* 12(4):454–464.
61. Marini J, Smith SM (2000) Osteogenesis Imperfecta. *Endotext* 363:1377–1385.
62. Misof K, Landis WJ, Klaushofer K, Fratzl P (1997) Collagen from the osteogenesis imperfecta mouse model (oim) shows reduced resistance against tensile stress. *J Clin Invest* 100(1):40–45.
63. Traub W, Arad T, Vetter U, Weiner S (1994) Ultrastructural studies of bones from patients with osteogenesis imperfecta. *Matrix Biol* 14(4):337–345.
64. Fratzl P, Paris O, Klaushofer K, Landis WJ (1996) Bone mineralization in an osteogenesis imperfecta mouse model studied by small-angle x-ray scattering. *J Clin Invest* 97(2):396–402.
65. Grabner B, et al. (2001) Age- and genotype-dependence of bone material properties in the osteogenesis imperfecta murine model (oim). *Bone* 29(5):453–457.
66. Vanleene M, et al. (2012) Ultra-structural defects cause low bone matrix stiffness despite high mineralization in osteogenesis imperfecta mice. *Bone* 50(6):1317–1323.
67. Vetter U, Weis MA, Mörike M, Eanes ED, Eyre DR (1993) Collagen crosslinks and mineral crystallinity in bone of patients with osteogenesis imperfecta. *J Bone Miner Res* 8(2):133–137.
68. Carriero A, et al. (2014) How tough is brittle bone? Investigating osteogenesis imperfecta in mouse bone. *J Bone Miner Res* 29(6):1392–1401.
69. Cassella JP, Ali SY (1992) Abnormal collagen and mineral formation in osteogenesis imperfecta. *Bone Miner* 17(2):123–128.
70. Cavallo F, De Giovanni C, Nanni P, Forni G, Lollini PL (2011) 2011: The immune hallmarks of cancer. *Cancer Immunol Immunother* 60(3):319–326.
71. Fischbach C, et al. (2007) Engineering tumors with 3D scaffolds. *Nat Methods* 4(10):855–

860.

72. Kenny PA, et al. (2007) The morphologies of breast cancer cell lines in three-dimensional assays correlate with their profiles of gene expression. *Mol Oncol* 1(1):84–96.
73. Wang F, et al. (1998) Reciprocal interactions between $\alpha 1$ -integrin and epidermal growth factor receptor in three-dimensional basement membrane breast cultures: A different perspective in epithelial biology. *Proc Natl Acad Sci* 95(25):14821–14826.
74. Hosseinkhani H, Hosseinkhani M, Tian F, Kobayashi H, Tabata Y (2006) Osteogenic differentiation of mesenchymal stem cells in self-assembled peptide-amphiphile nanofibers. *Biomaterials* 27(22):4079–4086.
75. Rhodes NP, Srivastava JK, Smith RF, Longinotti C (2004) Metabolic and histological analysis of mesenchymal stem cells grown in 3-D hyaluronan-based scaffolds. *J Mater Sci Mater Med* 15(4):391–395.
76. Infanger DW, Lynch ME, Fischbach C (2013) Engineered Culture Models for Studies of Tumor-Microenvironment Interactions. *Annu Rev Biomed Eng* 15(1):29–53.
77. Hutmacher D, et al. (2001) Mechanical properties and cell cultural response of polycalrolactone scaffolds designed and fabricated via fused deposition modelling. *J Biomedial Mater Res* 55(September 2015):203–216.
78. Bidan CM, et al. (2013) Geometry as a Factor for Tissue Growth: Towards Shape Optimization of Tissue Engineering Scaffolds. *Adv Healthc Mater* 2(1):186–194.
79. Peyton SR, et al. (2011) Marrow-Derived stem cell motility in 3D synthetic scaffold is governed by geometry along with adhesivity and stiffness. *Biotechnol Bioeng* 108(5):1181–1193.
80. McBeath R, Pirone DM, Nelson CM, Bhadriraju K, Chen CS (2004) Cell shape, cytoskeletal tension, and RhoA regulate stem cell lineage commitment. *Dev Cell* 6(4):483–495.
81. Chen CS, Mrksich M, Huang S, Whitesides GM, Ingber DE (1997) Geometric control of cell life and death. *Science (80-)* 276(5317):1425–1428.
82. Lynch ME, et al. (2013) In vivo tibial compression decreases osteolysis and tumor formation in a human metastatic breast cancer model. *J Bone Miner Res* 28(11):2357–2367.
83. Wagermaier W, Gourrier A, Aichmayer B (2013) Understanding Hierarchy and Functions of Bone Using Scanning X-ray Scattering Methods. *Materials Design Inspired by Nature: Function through Inner Architecture*, pp 46–73.
84. Hoerth RM, et al. (2014) Mechanical and structural properties of bone in non-critical and

- critical healing in rat. *Acta Biomater* 10(9):4009–4019.
85. Lange C, et al. (2011) Fetal and postnatal mouse bone tissue contains more calcium than is present in hydroxyapatite. *J Struct Biol* 176(2):159–167.
 86. Pabisch S, Wagermaier W, Zander T, Li C, Fratzl P (2013) *Imaging the nanostructure of bone and dentin through small- and wide-angle X-ray scattering* (Elsevier Inc.). 1st Ed. doi:10.1016/B978-0-12-416617-2.00018-7.
 87. Rinnerthaler S, et al. (1999) Scanning small angle X-ray scattering analysis of human bone sections. *Calcif Tissue Int* 64(5):422–429.
 88. Paris O, et al. (2011) Mapping lattice spacing and composition in biological materials by means of microbeam X-ray diffraction. *Adv Eng Mater* 13(8):784–792.
 89. Gamsjaeger S, Kazanci M, EP P, Fratzl P (2009) Raman Application in Bone Imaging. *Raman Spectroscopy for Soft Matter Applications*, ed Maher S. Amer (John Wiley & Sons, Inc), pp 227–267.
 90. Gentleman E, et al. (2009) Comparative materials differences revealed in engineered bone as a function of cell-specific differentiation. *Nat Mater* 8(9):763–770.
 91. Bertazzo S, et al. (2013) Nano-analytical electron microscopy reveals fundamental insights into human cardiovascular tissue calcification. *Nat Mater* 12(6):576–583.
 92. Kunitake JAMR, et al. (2018) Correlative imaging reveals physiochemical heterogeneity of microcalcifications in human breast carcinomas. *J Struct Biol* 202(1):25–34.
 93. Bazin D, et al. (2009) Diffraction techniques and vibrational spectroscopy opportunities to characterise bones. *Osteoporos Int* 20(6):1065–1075.
 94. Morris MD, Mandair GS (2011) Raman assessment of bone quality. *Clin Orthop Relat Res* 469(8):2160–2169.
 95. Kazanci M, Roschger P, Paschalis EP, Klaushofer K, Fratzl P (2006) Bone osteonal tissues by Raman spectral mapping: Orientation-composition. *J Struct Biol* 156(3):489–496.
 96. Yerramshetty JS, Akkus O (2008) The associations between mineral crystallinity and the mechanical properties of human cortical bone. *Bone* 42(3):476–482.

CHAPTER 2: HYDROXYAPATITE MINERAL ENHANCES MALIGNANT POTENTIAL IN A TISSUE-ENGINEERED MODEL OF BREAST CANCER

Contributors: Siddharth Pathi, Nora Springer, Matthew Whitman, Yeonkyung Lee, Stephen Marcott, Aaron Chiou, Angela Du, Pragya Shah, Joseph Druso, Bryant Blank, Sunish Mohanan, Maxine Jochelson, Neil Iyengar, Jan Lammerding, and Claudia Fischbach.

2.1 Abstract

Screening mammograms routinely detect the presence of breast tissue microcalcifications (MCs), and MCs comprised primarily of hydroxyapatite (HA) are associated with increased tumor aggressiveness and lymph node involvement. The vast majority (90-95%) of ductal carcinoma *in situ* (DCIS) cases present with MCs, though how certain cases progress to invasive breast cancer is unclear. Thus, the study of how tumor cells respond to mineral will be critical in understanding breast cancer pathogenesis. However, there currently exists limited approaches to effectively model tumor cell-mineral interactions. Here, we have cultured breast cancer cells in HA-containing PLG scaffolds to investigate whether HA can promote tumor cell malignancy. Within a series of isogenic MCF10A-derived breast epithelial cell lines representing different stages of breast cancer progression, we found that exposure to HA mineral in scaffolds increased the expression of pro-tumorigenic interleukin-8 (IL-8) among transformed but not benign cell lines. Notably, MCF10DCIS.com cells cultured in HA scaffolds adopted morphological changes that were reflective of increased invasiveness and exhibited increased motility that were dependent on IL-8 signaling. Moreover, MCF10DCIS.com xenograft tumors initiated in HA scaffolds displayed evidence of enhanced malignant progression, including significantly decreased epithelial organization and increased fibrosis compared to PLG controls. These results indicate that HA

*Portions adapted from Pathi SP (2013) Minerals and Metastasis: Hydroxyapatite Promotes Breast Cancer Colonization of Bone. PhD dissertation (Cornell University).

mineral may actively promote malignancy in preinvasive DCIS cells and validate PLG scaffolds as useful tools to study microenvironmental parameters in a pathologically relevant manner.

2.2 Introduction

Breast cancer is a leading cause of cancer-related deaths in women (1). Breast tissue microcalcifications (MCs) serve as critical diagnostic indicators for non-palpable breast cancer during routine mammographic screening (2). Microcalcifications are associated with 90-95% of all ductal carcinoma *in situ* (DCIS) cases as well as some high risk invasive cancers (3–6). The presence of MCs in invasive ductal carcinoma (IDC) patients has been correlated with greater tumor volume, increased lymph node involvement, and decreased 8-year patient survival (7).

Despite their value as diagnostic markers, the functional relationship between MCs and breast cancer malignant progression remains unclear. Studies focused on MC chemical composition have found that MCs associated with benign breast lesions are exclusively composed of calcium oxalate while MCs associated with malignant breast lesions are largely composed of hydroxyapatite (HA) (4, 5, 8). Although mammary MCs are currently treated as inert in clinical settings, *in vitro* studies have shown that HA is bioactive and can regulate breast cancer cell behavior (9–13). Collectively, these observations suggest that HA MCs may actively promote tumor progression and consequently, increase metastatic potential. However, the underlying mechanisms remain unclear.

Both clinical and experimental studies suggest that DCIS is a precursor lesion to most invasive breast carcinomas (IBC) (14), though how DCIS progresses to IBC is a subject of much inquiry. Ductal breast cancer invasion into the surrounding stroma requires that tumor cells breach the basement membrane (15). To facilitate their escape from the primary site, transitioning breast cancer cells are known to undergo the epithelial-to-mesenchymal transition (EMT) (16), which is

a dynamic, multifactorial process characterized by dysregulated proliferation, loss of cell-to-cell contact, and increased cell motility (15, 17–19). These properties are thought to be regulated by a network of cytokines in the tumor microenvironment (20–24). Specifically, interleukin-8 (IL-8) – which has been found to be enriched in neoplastic breast tissue (25, 26) and in the circulation of advanced breast cancer patients (27) – may be critical for the induction of EMT and maintenance of the mesenchymal, de-differentiated phenotype (23, 28). Importantly, there is emerging evidence to suggest that IL-8 is upregulated in breast cancer cells interacting with HA mineral (11–13). These studies, however, are limited by their focus on MDA-MB-231, a highly metastatic breast cancer cell line that is unsuitable for modeling the transition of preinvasive breast cancer to a more malignant phenotype.

Three-dimensional (3D) culture systems employing poly(lactide-*co*-glycolide) (PLG) scaffolds can be used to recapitulate pathologically relevant tumor microenvironmental conditions (29, 30). Within PLG scaffolds, cancer cells cultured *in vitro* organize into tumor-like structures that are representative of their *in vivo* counterparts, with comparable growth kinetics, cytokine secretion profiles, and formation of hypoxic cores (29). Poly(lactide-*co*-glycolide) scaffolds have also been shown to effectively present mineral to cells, as they enable direct cell-to-mineral interactions (11, 12, 31). As such, they are well suited to study how mammary MCs may mediate breast cancer cell behavior. We therefore employed engineered mineral-containing scaffolds to investigate the role of HA mineral on breast cancer cell malignancy. Isogenic breast cancer cell lines of increasing malignancy were first profiled for HA-mediated upregulation of IL-8. Morphological and migratory hallmarks of invasiveness were assessed within a premalignant DCIS cell line cultured on HA scaffolds. Next, antibody inhibition studies were performed to test whether HA-mediated effects on DCIS cell motility were IL-8-dependent. Lastly, to confirm

pathological relevance, DCIS tumors were initiated in a scaffold-xenografts to investigate the effects of HA mineral in an *in vivo* setting.

2.3 Materials and Methods

2.3.1 Cell lines and growth media

Human mammary epithelial cell lines from the MCF10A cell line series – MCF10A, MCF10DCIS.com, and MCF10CA1a (Karmanos Institute) – were cultured in 1:1 DMEM/F12 (Gibco) supplemented with 5% horse serum (Invitrogen), 1% penicillin/streptomycin (Gibco), 10 µg/ml insulin (Sigma), 0.5 µg/ml hydrocortisone (Sigma), 100 ng/ml cholera toxin (Sigma), and 20 ng/ml EGF (Millipore). Human mammary adenocarcinoma cell line MDA-MB-231 was cultured in DMEM (Gibco) supplemented with 10% FBS (Atlanta Biologicals) and 1% penicillin/streptomycin (Gibco).

2.3.2 Scaffold fabrication

Porous, polymeric scaffolds were fabricated using a gas-foaming, particulate leaching method (11). For hydroxyapatite-containing (HA) scaffolds, poly(lactide-*co*-glycolide) (PLG) microparticles (ground and sieved, ~250 µm diameter; Lakeshore Biomaterials) and PLG microspheres (formed by double emulsion, ~5-50 µm diameter; Lakeshore Biomaterials) were dry-mixed with nanocrystalline hydroxyapatite (Sigma) and sodium chloride (sieved, ~250-400 µm diameter; J.T. Baker). The mixture was then pressed to form matrices (8.5 mm diameter, 1 mm thick) at room temperature in a dye press (Fred. S. Carver) and then pressurized in carbon dioxide (800 psi) with a non-stirred vessel (Parr Instruments). After a quick de-pressurization, scaffolds were soaked for 24 hours in de-ionized water to leach out the sodium chloride. Non-mineral-containing (PLG) scaffolds were fabricated similarly, excluding the hydroxyapatite in the starting mixture.

2.3.3 Three-dimensional cell culture

Scaffolds were sterilized in 70% ethanol for 20 minutes, washed 2 times with sterile PBS, then soaked in serum-containing media for 30 minutes. 1.5×10^6 cells were statically seeded on each scaffold and then maintained under dynamic culture conditions on an orbital shaker. The scaffold-tumors were subjected to a 72-hour pre-culture period before analysis or additional *in vitro*-based studies. Gene expression analysis was performed after a 10-day culture period to increase cell numbers for analysis. For *in vivo* studies, scaffold-tumors were cultured for 24 hours prior to surgeries to enable sufficient cell adhesion within the scaffold.

2.3.4 Scaffold characterization

To characterize mineralization, blank scaffolds were soaked in Alizarin Red S stain (20% of 40mM solution in de-ionized water, pH 4.1; VWR) for 20 minutes at room temperature and then washed 4 times in PBS. To visualize distribution of mineral throughout the porous scaffold matrix, blank scaffolds were scanned with a μ CT system (Zeiss) and false-colored based on the attenuation coefficient. To visualize cell associations with mineral in scaffolds, cell-seeded scaffolds were fixed in 4% paraformaldehyde (PFA) (VWR) overnight, embedded in paraffin blocks, cut into cross-sections, and subjected to von Kossa staining.

2.3.5 Analysis of cell proliferation and IL-8 expression

To assess proliferation, tumor cell-seeded scaffolds were lysed in Caron's buffer and sonicated at low power to liberate cellular DNA. Total DNA content was measured from these samples by the QuantiFluor® dsDNA System (Promega) according to manufacturer instructions. To quantify secretion of IL-8, tumor cell-seeded scaffolds were cultured in low serum prior to collection of media, which was then used in the IL-8 ELISA (R&D Systems) according to manufacturer instructions. To analyze IL-8 gene expression, total RNA was harvested from tumor

cell-seeded scaffolds with TRIzol® (Invitrogen) according to manufacturer instructions and 1 µg was reverse transcribed to cDNA (qScript cDNA supermix, Quanta BioSciences). Quantitative real-time polymerase chain reaction (qRT-PCR) was performed using SYBR green detection (Quanta BioSciences) on an Applied Biosystems 7500 System. The following primer sequences were used: human IL-8 (fwd: 5'- agaaaccaccggaaggaacctct-3', rev: 5'- agagctgcagaaatcaggaaggct-3') and human β-actin (fwd: 5' - aatgtggccgaggactttgattgc-3', rev: 5'- aggatggcaagggacttcctgtaa-3') (IDT Technologies). Quantitative analysis was performed based on the $\Delta\Delta C_t$ method(32). Sample size was n = 3 or greater per condition.

2.3.6 Cell morphology and cell clustering analysis

Following an initial pre-culture period, MCF10DCIS.com cells were detached from scaffolds with 0.5% trypsin (Gibco) and re-seeded (4000 cells) onto glass coverslips (18 mm, #1 thickness; Karl Hecht) pre-coated with 30 µg/ml fibronectin (Gibco) (Fn). The re-seeded cells were maintained in standard culture conditions for either 4 hours to analyze morphology or 24 hours to analyze clustering and other invasive characteristics, then fixed in 4% PFA, and co-stained for F-actin (1:100 Alexafluor 568 phalloidin; Invitrogen) and nuclei (1:2000 DAPI; Invitrogen). Imaging was performed on an epi-fluorescence microscope (Zeiss Observer Z1).

Morphology analysis of single cells was performed in ImageJ FIJI. Greyscale images were thresholded to create binary images and all single cells were analyzed for 1/circularity ($\text{perimeter}^2 / 4 \cdot \pi \cdot \text{area}$), which was termed 'Morphology Factor' (MF), and aspect ratio (major axis / minor axis) (AR). All measures of cell morphology were log-transformed to better fit the assumptions of the model (normality of residues, constant variance). The resulting data were analyzed using a mixed model with random (sample and nested replicates) and fixed (condition)

effects. Sample size was $n = 3$ per condition and at least 30 cells were analyzed per sample. Graphs show the log-transformed MF and AR data.

Cell clusters were defined as cells that were tightly bound to at least one other cell. Sample size was $n = 3$ per condition; six representative images per sample were taken and manually counted for cells. The results were expressed as a percentage of the combined total of individual cells and clusters.

2.3.7 Cell motility analysis

To assess random cell migration, MCF10DCIS.com cells pre-cultured in scaffolds were detached with 0.5% trypsin (Gibco) and re-seeded (1500 cells) onto Fn-coated (Gibco) (30 $\mu\text{g}/\text{ml}$) optically clear 96-well plates for live cell tracking (IncuCyte) over 24 hours. IL-8 antibody (20 $\mu\text{g}/\text{ml}$; Cormorant Pharmaceuticals) was added to the media at the start of the experimental period. The x- y- movement of single cells were tracked over timeframes of 300 minutes. Sample size was $n = 4$ per condition and at least five cells were analyzed per sample.

To assess directed migration, MCF10DCIS.com cells pre-cultured in scaffolds were detached with 0.5% trypsin (Gibco) and re-seeded (5000 cells) into bovine collagen I-coated (40 $\mu\text{g}/\text{ml}$; Corning) transwells (8.0 μm pores; VWR) placed in 24-well plates. The cells were seeded in DMEM in the top chambers and induced to migrate towards bottom chambers containing DMEM 10% FBS over 16 hours. An IL-8 antibody (20 $\mu\text{g}/\text{ml}$; Cormorant Pharmaceuticals) was added to the DMEM in the top chamber at the start of the experimental period. Cotton swabs were used to carefully remove cells from the top sides of the transwell membranes. Cells were then fixed in 4% PFA and stained for nuclei (1:2000 DAPI; Invitrogen). A 2.5X objective was used to capture images that were later stitched together to show the entire transwell, which were then manually analyzed for migrated cells.

2.3.8 Human samples analysis

Sixteen patient samples – with mostly mixed pathologies of DCIS and Invasive Ductal Carcinoma (IDC) – were obtained for correlative histopathology and immunohistochemical (IHC) staining for IL-8. Tissue samples were transferred as frozen blocks from Memorial-Sloan Kettering Hospital. Frozen blocks were cryosectioned to 12 μm thickness and mounted on pre-cleaned glass slides. Prior to staining, sections were baked for 20 minutes at 65°C and re-hydrated in Tris-buffer. Sections were then blocked with 3% hydrogen peroxide to prevent signal interference from endogenous activity. Antigen retrieval was performed with Proteinase K (Dako), and TNB solution (Perkin-Elmer) was used for blocking. Sections were incubated with primary antibody against IL-8 (5 $\mu\text{g}/\text{m}$; R&D Systems) overnight at 4°C, followed by a 30 min incubation at room temperature with a biotinylated secondary antibody against mouse (Vector Labs). To increase signal, the TSA amplification kit (Perkin-Elmer) was used according to manufacturer's direction. Signal detection was performed with DAB chromogen (Thermo Scientific), and sections were counter-stained with hematoxylin. Slides were then dehydrated via ethanol gradient and mounted with Entellan (Merck). Slides were scanned using the ScanScope System (Aperio).

Scanned IL-8 IHC images were then transferred to a pathologist for specific evaluation and diagnosis. Slides were scored for gross intensity of IL-8 staining, and individual acini and ductal structures were identified for each slide and scored for ductal integrity/proliferative capacity as well as IL-8 stain intensity. Sections were comprehensively analyzed to identify all ductal structures, and all ductal structures were included in the analysis. If at least 3 ducts could not be identified, that particular section was not analyzed. All metrics were scored on a 0-to-3 scale, with 0 representing negligible intensity or proliferation and 3 representing maximal staining or excessive proliferation and total deterioration of acinar architecture. This analysis was performed

blind, without knowledge of radiology or pathology reports from consulting clinicians. After full evaluation was completed, IHC evaluation was compared with radiology and pathology notes.

2.3.9 Scaffold-xenograft studies

Animal studies were conducted in accordance with Cornell University guidelines and were approved by Cornell University's Institutional Animal Care and Use Committee (IACUC). 6- to 7-week-old female Hsd:Athymic Nude-Foxn1^{nu} mice (n = 5 or 6) from Envigo were used for MCF10DCIS.com scaffold-xenograft studies. Scaffolds were seeded with 5×10^5 cells, maintained in dynamic culture conditions for 24 hours, and then kept on ice until implantation. Mice were anesthetized, and incisions were made to the dorsal interscapular skin. Contralateral subcutaneous pockets in the infrascapular regions containing the third pair of mammary glands were then gently enlarged using a sterile forcep, and then irrigated with sterile PBS. Cell-seeded scaffolds were then inserted into subcutaneous pockets, one on each side. The experimental endpoint was at 4 weeks. Scaffold-tumors were halved: one half was fixed in 4%PFA and embedded in paraffin while the other half was lysed with TPER buffer and mechanically/sonically digested. Blood was also collected and immediately processed to serum. IL-8 ELISA analysis (R&D Systems) was performed on both serum and tissue lysates.

The fixed and embedded scaffold-tumors were stained with hematoxylin and eosin (H&E) and Masson's Trichrome. Scanned images were then transferred to a pathologist for specific evaluation and diagnosis. Epithelial morphology, an assessment of ductal organization, was scored on a 1-to-4 scale, with 1 representing <25% fields containing organized tubules and acinar arrangements with central comedo and with 2, 3, and 4 representing 25-50%, 50-75%, and >75% fields with the aforementioned qualities, respectively. Fibrosis was scored on a 1-to-3 scale, with 1 representing thin distinct bands of fibrovascular stroma throughout sheets of neoplastic cells,

and with 2 and 3 representing streaming thick fibrovascular bands separating neoplastic cells in <50% and >50% of fields, respectively. Cells with visible chromosomes were assessed as Mitotic Figures. This analysis was performed blind.

2.3.10 Statistical analyses

For comparison between two conditions, unpaired Student's t and Mann-Whitney U tests were used to compare parametric and nonparametric data, respectively. For comparison between three conditions, ANOVA with Tukey's post hoc and Kruskal-Wallis with Dunn's post hoc were used to compare parametric data and nonparametric data, respectively. A mixed model was used to analyze cell morphology data (see above). For *in vitro* studies, sample size was either n = 3 or 4, and at least two separate experiments were performed to confirm trends. Data are represented as means +/- SD and p<0.05 was considered statistically significant. GraphPad Prism 8 (GraphPad Software) and JMP 12 (SAS Institute) were used for statistical analyses, which were performed in consultation with an independent statistician from the Cornell Statistical Consulting Unit.

2.4 Results

2.4.1 Mineral-containing PLG scaffolds enable study of cell-mineral interactions in 3D

To investigate the effects of HA mineral on breast cancer cell behavior, we engineered a mineral-containing scaffold-based culture platform that was previously developed by our laboratory to study cancer cell behavior in a bone-mimetic microenvironment (11, 33). Here, we confirmed that these scaffolds enabled direct interaction between HA mineral and the seeded cells. To test surface presence of mineral within scaffold pores, we soaked scaffolds in calcium-binding Alizarin Red S Stain (ARS). We observed that the mineral-containing but not control scaffolds showed strong absorption of the red stain, suggesting surface availability of HA (Fig. 2.1A). Microcomputed tomography images of scaffold cross-sections provided visualization of mineral

distribution throughout the porous matrix and showed comparable pore size between mineral-containing HA scaffolds and control PLG scaffolds (Fig. 2.1B), confirming previous results (11). Breast cancer cells were statically seeded onto the scaffolds and maintained in dynamic culture conditions (Fig. 2.1C) to form tissue-like structures (Fig. 2.1D) in 3D. Von Kossa staining of the seeded breast cancer cells showed that the cells attached along mineral-containing surfaces (Fig. 2.1D), which corroborated earlier work suggesting that breast cancer cells exhibited strong adhesive properties within mineral-presenting culture systems, including mineral-containing PLG scaffolds (11) and to mineral-coated surfaces (13).

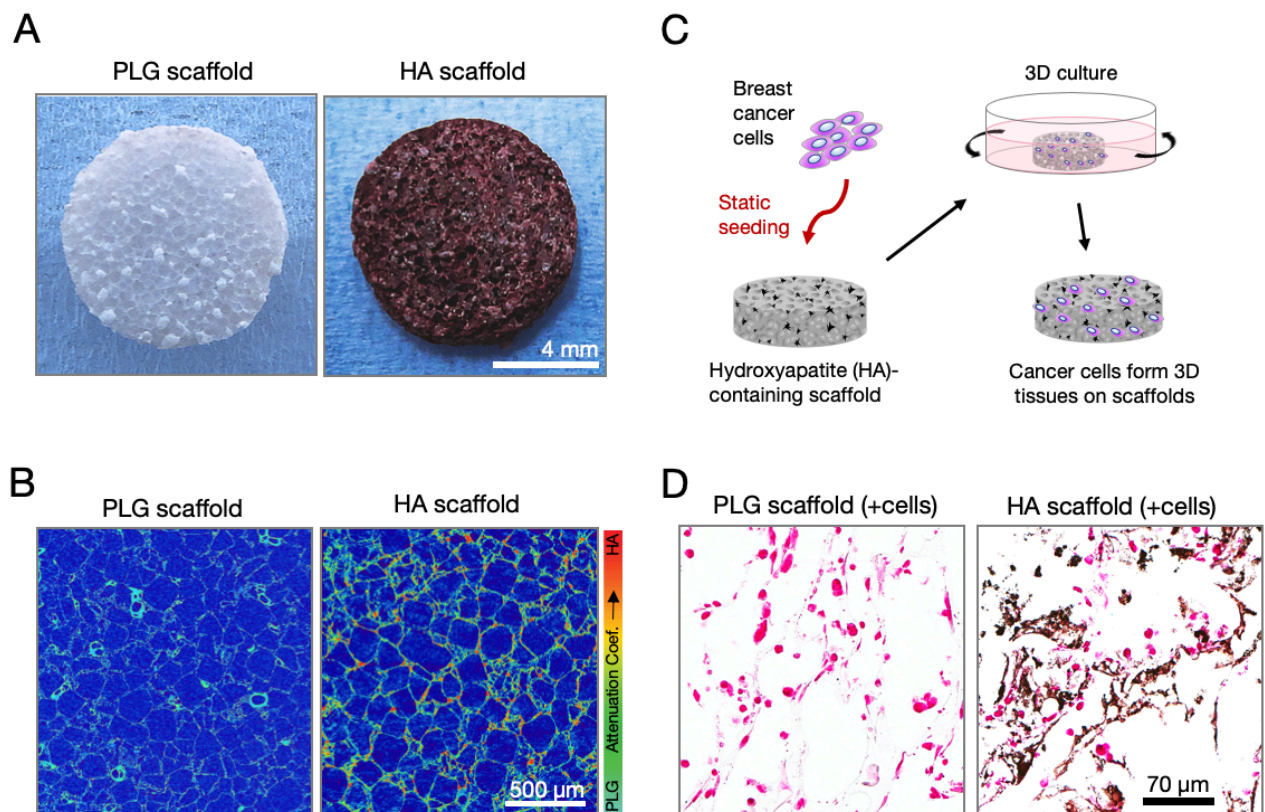


Figure 2.1: Mineral-containing PLG scaffolds enable study of cell-mineral interactions in 3D. (A) Representative Alizarin Red S stain showing surface presentation of mineral in hydroxyapatite (HA)-containing scaffolds versus PLG control scaffolds. (B) Representative false-color microCT cross-sections showing mineral distribution as function of the attenuation coefficient, which increases with atomic number. (C) Schematic showing setup of 3D culture system: breast cancer cells were statically seeded onto hydroxyapatite-containing PLG scaffolds and then maintained under dynamic culture conditions on an orbital shaker. (D) Representative Von Kossa stain showing both calcium phosphate mineral (black) and cell nuclei (pink) in tumor cell-seeded HA scaffolds versus tumor cell-seeded PLG scaffolds.

2.4.2 Correlation between IL-8 enrichment and presence of mammographic calcifications and proliferative ductal epithelia

We had previously shown that HA mineral stimulates IL-8 secretion and proliferation in metastatic breast cancer cell lines *in vitro* (11–13). To evaluate the clinical relevance of these findings to DCIS, we analyzed a set of human breast samples with mostly mixed DCIS/IDC pathologies. Microcalcifications were detected via mammography in over half of these samples and generally presented with morphologies that are linked with malignant lesions (Fig. 2.2A) (4).

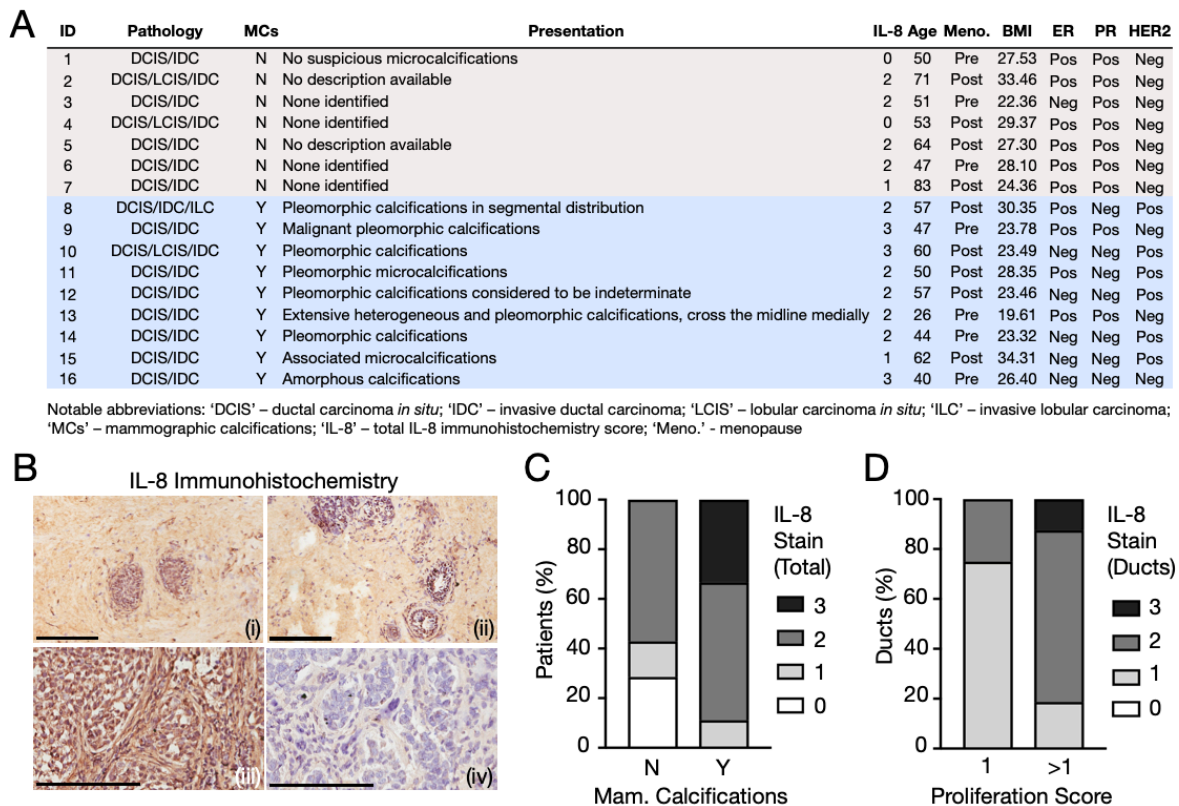


Figure 2.2: Histopathological analysis of human breast cancer samples correlates IL-8 enrichment with the presence of mammographic calcifications and proliferative ductal epithelia. (A) Patient information for assessed specimens, sorted by presence of mammographic calcifications. 'IL-8' indicates the corresponding degree of total IL-8 stain via immunohistochemistry (IHC). (B) Representative IL-8 IHC with hematoxylin counterstain. Image labels: (i) - Weak ductal; (ii) - Strong ductal; (iii) - Strong ductal and stromal; (iv) – No IgG. Scale bars = 200 μ m. (C) Histopathological scoring for the degree of total IL-8 stain as a function of mammographic calcifications. Rubric for total IL-8 staining intensity: 0-to-3, with 0 representing negligible intensity and 3 representing maximum staining. N vs. Y: $p < 0.05$. (D) Histopathological scoring for the degree of ductal IL-8 stain as a function of the ductal proliferation score. Rubric for ductal IL-8 staining intensity: 0-to-3, with 0 representing negligible intensity and 3 representing maximum staining. Rubric for ductal proliferation: 0-to-3, with 0 representing negligible proliferation and 3 representing excessive proliferation and total deterioration of acinar architecture. 1 vs. >1: $p < 0.05$.

Interestingly, we also noted a possible connection between the presence of MCs and PR-/HER2+ subtypes (Fig. 2.2A). IL-8 immunohistochemistry (IHC) showed variable staining patterns, with IL-8 present in ducts, stroma, or both (Fig. 2.2B). Total tissue IL-8 levels were found to be greater in samples with mammographically detected MCs (Fig. 2.2C), and within ducts, there appeared to be a positive correlation between ductal IL-8 staining intensity and ductal proliferation (Fig. 2.2D). Taken together, these analyses point to a potential link between the presence of mammographically-detected MCs in tumorigenic breast tissue and the upregulation of IL-8.

2.4.3 HA mineral regulates proliferation and IL-8 expression across breast cancer cell lines

To more directly investigate how the progression of breast cancer influences responses to HA mineral, we cultured 3 isogenically matched MCF10 cell lines – normal MCF10A (10A), premalignant MCF10DCIS.com (DCIS), and metastatic MCF10CA1a (CA1a) (34) – in our mineral-containing scaffolds and used non-mineral-containing scaffolds as controls. We extracted nucleic acids from our scaffold-tumors to quantify cell proliferation using a DNA assay and IL-8 gene expression using qRT-PCR (Fig. 2.3A); we also quantified the presence of IL-8 in the tumor-conditioned media using an ELISA assay (Fig. 2.3A). We observed that HA stimulated proliferation in the normal (10A) and premalignant (DCIS) cell lines, but not in the invasive (CA1a) cells (Fig. 2.3B). Conversely, however, HA upregulated IL-8 gene expression (Fig. 2.3C) and soluble factor secretion (Fig. 2.3D) in the premalignant (DCIS) and metastatic (CA1a) cell lines, but not in the benign (10A) cells. Collectively, these data suggest that HA-mediated cell proliferation and IL-8 secretion occurs for breast cancer cell lines across a range of molecular profiles. The increase in IL-8 secretion may be mediated by differential engagement of the $\alpha v \beta 3$ integrin (Fig. 2.4) between the breast cancer cells and the HA incorporated within the scaffolds. For the remainder of the study, we focused on the MCF10DCIS.com cell line, as they can form, in

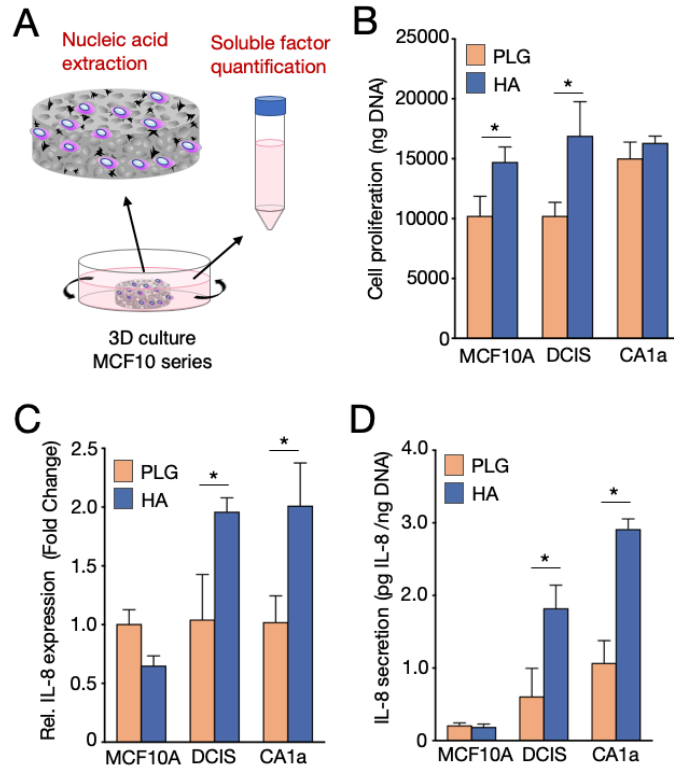


Figure 2.3: Hydroxyapatite mineral regulates proliferation and IL-8 expression across breast cancer cells. (A) Schematic showing extraction of nucleic acids and quantification of soluble factors from 3D cultures of MCF10 series-seeded scaffolds. (B) DNA assay quantifying double-stranded DNA harvested from breast cancer cell lines cultured in scaffolds. (C) RT-PCR analysis of IL-8 gene expression from RNA harvested from breast cancer cell lines cultured in scaffolds. (D) ELISA analysis quantifying IL-8 secretion in tumor-conditioned media. Data are means +/- SD. For all plots, * $p < 0.05$.

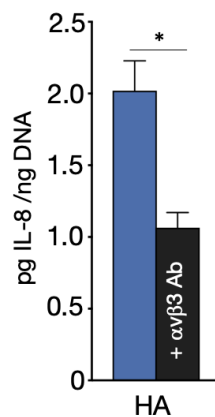


Figure 2.4: IL-8 expression of MDA-MB-231 cells cultured in HA scaffolds is mediated by the integrin $\alpha v \beta 3$. ELISA analysis quantifying IL-8 secretion in tumor-conditioned media from hydroxyapatite-containing scaffolds seeded with MDA-MB-231 cells cultured with or without 25 $\mu\text{g/mL}$ LM609 (Millipore), an antibody antagonist targeting integrin $\alpha v \beta 3$.

xenograft models, comedo-type lesions histopathologically representative of the high-grade DCIS in human samples (35). Notably, this DCIS cell line exhibited a pronounced response to HA mineral, as both proliferation (Fig. 2.3B) and IL-8 expression (Fig. 2.3C, 2.3D) were increased, findings that support our histopathological analyses of human breast samples.

2.4.4 DCIS cells interacting with HA mineral in 3D culture adopt morphological hallmarks of invasiveness

Next, we were interested in whether HA mineral could promote morphological characteristics associated with increased invasiveness. We used epifluorescence microscopy to image DCIS cells that were pre-cultured in either mineral-containing or control scaffolds and then re-seeded onto Fn-coated glass coverslips for analysis (Fig. 2.5A). A tissue culture-treated polystyrene condition (2D) was included to account for effects of dimensionality and confirm that any observed effects were not due to enzymatic dissociation from scaffolds during the re-seeding process. After an attachment period of 4 hours, we assessed changes in cell shape. We found that DCIS cells cultured in HA scaffolds adopted a wide variety of shapes, including elongated spindles, dendritic stellates, and others (36, 37) (Fig. 2.5B). We then quantified these changes by calculating, for each cell analyzed, a Morphology Factor (MF), which we determined to be effective at capturing a range of cell shapes associated with increased motility (Fig. 2.6). Correspondingly, we found that DCIS cells cultured in HA scaffolds exhibited a significant increase in MF when compared to ones pre-cultured in control PLG scaffolds (Fig. 2.5B, 2.5C). To assess how cell colony properties were impacted by HA pre-culture, we allowed the re-seeded DCIS cells to proliferate for a total of 24 hours before imaging. We observed that HA appeared to promote hallmarks of invasiveness (38), including processes connecting multiple cell bodies and

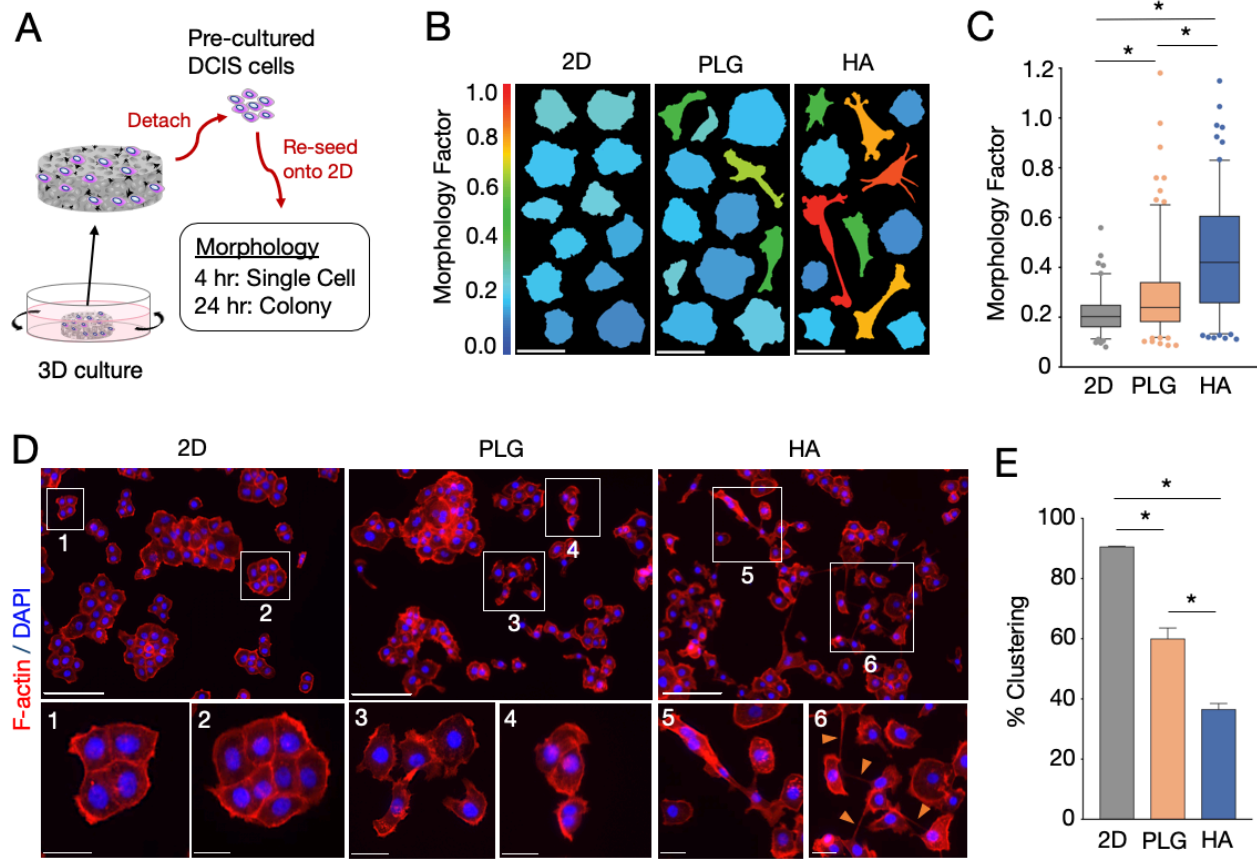


Figure 2.5: DCIS cells interacting with hydroxyapatite mineral in 3D culture adopt morphological hallmarks of invasiveness. (A) Schematic showing experimental setup for morphological characterization: pre-cultured MCF10DCIS.com (DCIS) cells were detached from scaffolds, re-seeded onto Fibronectin-coated glass coverslips, and evaluated for single cell (4 hours) and cell colony (24 hours) morphological characteristics. 2D polystyrene pre-cultures were used as controls. (B) Typical cell morphologies of DCIS cells exposed to different pre-culture conditions. Cells were stained for F-actin for visualization. Each vertical panel shows thresholded images of 12 representative cells with a mean Morphology Factor (MF) equivalent to the mean MF of each respective condition. Color scale: warmer colors indicate greater MF. Scale bars, 50 μm . (C) Graph comparing MFs between pre-culture conditions. The means are depicted by the red bars. * $p < 0.05$. (D) Representative fluorescent images from DCIS cells exposed to different pre-culture conditions. Cells were co-stained for F-actin (red) and nuclei (blue). Insets magnify the regions outlined by white boxes. Orange arrows in inset 6 highlight cellular processes. Scale bars: top panels, 200 μm ; bottom panels, 50 μm . (E) Graph comparing % clustering between pre-culture conditions. Data are means \pm SD. * $p < 0.05$.

decreased cell-to-cell contact (Fig. 2.5D) when compared with PLG. Accordingly, quantifying the relative number of cell clusters (39) confirmed a marked decrease in the percentage of cell clusters (and thus, an increase in the percentage of individual cells) in the DCIS cells pre-cultured in the HA scaffolds versus the control scaffolds (Fig. 2.5E). As expected, the 3D results were

dramatically different from the 2D with regards to cell morphology and clustering as DCIS cells pre-cultured in 2D controls were generally round (Fig. 2.5B), and readily formed organized, tightly-bound cell colonies (Fig. 2.5D, 2.5E).

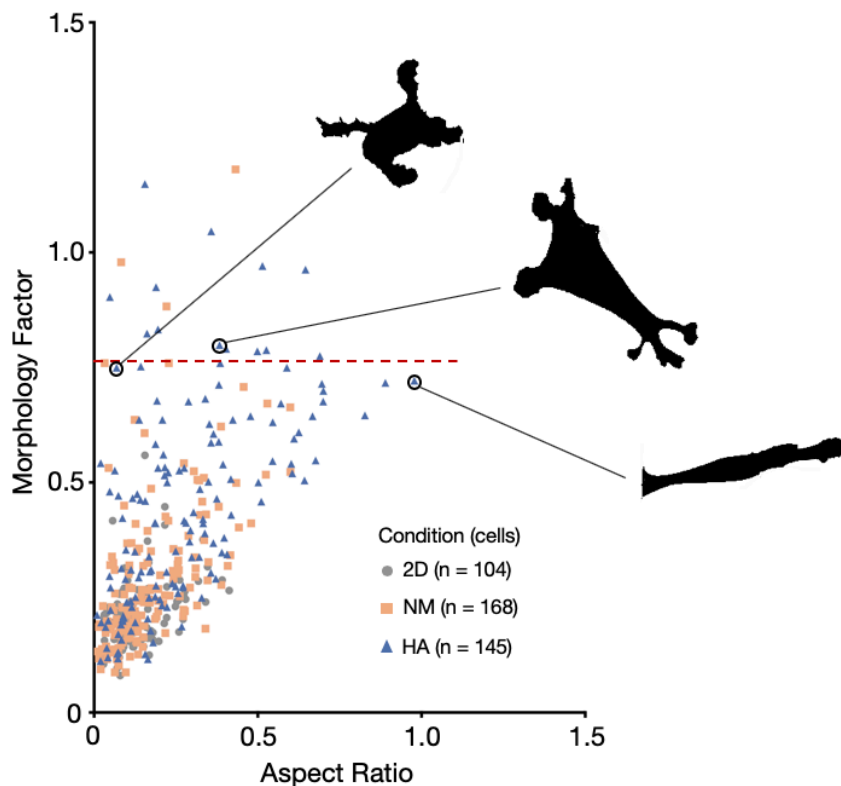


Figure 2.6: Calculation of the Morphology Factor captures a range of migratory cell shapes in scaffold cultures of DCIS cells. Graph compares log-transformed Morphology Factor ($\text{perimeter}^2 / 4 \cdot \pi \cdot \text{area}$) (MF) with log-transformed Aspect Ratio (major axis / minor axis) for cells exposed to the three pre-culture conditions (2D, PLG scaffolds, HA scaffolds). Thresholded images of three representative cells with similarly high MF but varying AR show a range of cell shapes associated with migratory behavior.

2.4.5 HA mineral increases DCIS cell motility mediated by IL-8

We then asked whether HA mineral could enhance the motility of individual DCIS cells. To this end, we performed live tracking of single DCIS cells that were pre-cultured in either mineral-containing or control scaffolds and then re-seeded onto Fn-coated optically-clear plates for analysis (Fig. 2.7A). A 2D condition was also included here to account for other experimental variables, as discussed above.

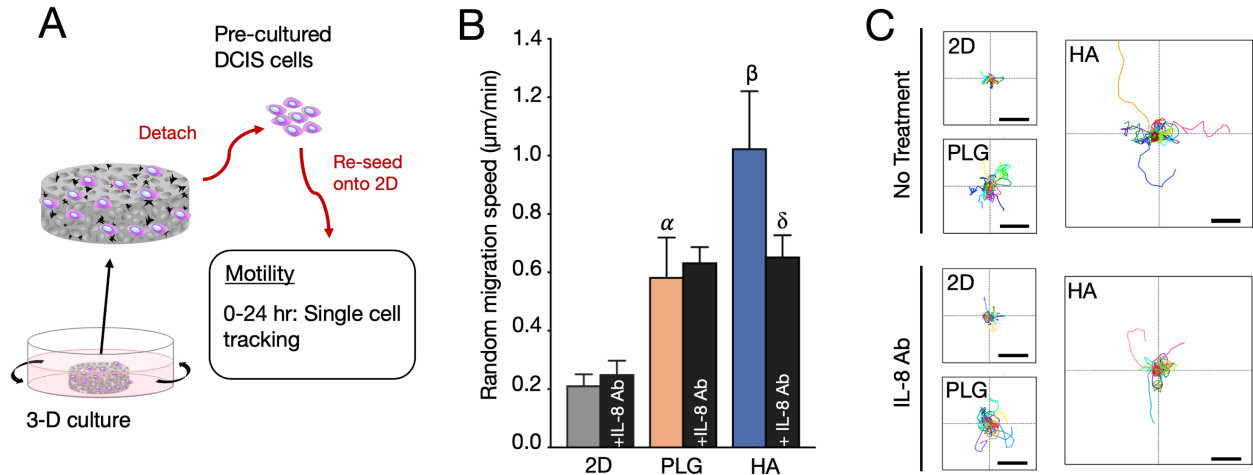


Figure 2.7: Hydroxyapatite mineral increases DCIS cell motility mediated by IL-8. (A) Schematic showing experimental setup for assessment of random migration: pre-cultured MCF10DCIS.com (DCIS) cells were detached from scaffolds, re-seeded onto Fn-coated optically-clear plates, and evaluated for indices of cell motility over 24 hours. In addition to the indicated pre-culture conditions, cells were treated with IL-8 antibody (20 µg/mL) at the start of the tracking period. Cells were analyzed for their x- y-movement over 300-minute timeframes. 2D polystyrene pre-cultures were used as controls. (B) Graph comparing random migration speeds of cells pre-cultured in different conditions. Data are means +/- SD. α ($p < 0.05$): PLG vs. 2D. β ($p < 0.05$): HA vs. PLG; HA vs. 2D. δ ($p < 0.05$): HA+IL8 Ab vs. HA. (C) Relative (x, y) trajectories of single cells tracked for 300 minutes from different pre-culture conditions. For each plot, the lines intersect at position (0,0). Scale bar = 100 µm.

We observed an increase in the random migration speed of DCIS cells pre-cultured in HA scaffolds versus control PLG scaffolds (Fig. 2.7B). Interestingly, a subset of HA pre-cultured DCIS cells also exhibited greater maximum range (Fig. 2.7C). To assess if the increase in HA-mediated motility was dependent on IL-8 signaling, we treated the pre-cultured cells with IL-8 antibody at the start of the tracking period. These effects were decreased during the IL-8 antibody treatment of DCIS cells exposed to HA, but in contrast, no differences were observed in either speed or range in the control PLG scaffold condition with IL-8 antibody treatment (Fig. 2.7B, 2.7C). Moreover, we also found HA pre-cultured cells were responsive to IL-8 antibody treatment in a trans-well assay of directed migration (Fig. 2.8). Accordingly, DCIS cells exhibited greater speed and range when pre-cultured in the 3D scaffold system versus the 2D control (Fig. 2.7B, 2.7C), corresponding with changes of cell morphology associated with dimensionality. Taken

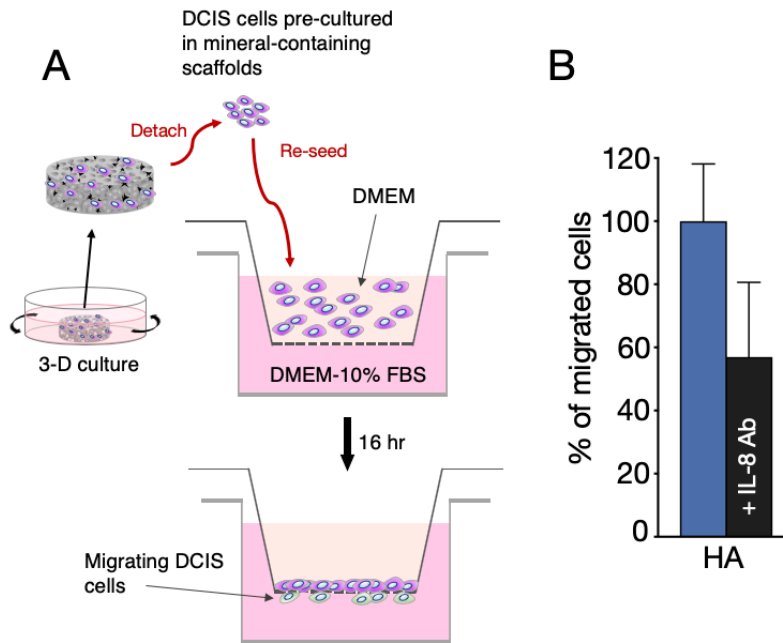


Figure 2.8: DCIS cells exposed to pre-culture in hydroxyapatite-containing scaffolds may exhibit IL-8 dependent directed migration. (A) Schematic showing experimental setup for assessment of directed migration: pre-cultured MCF10DCIS.com (DCIS) cells were detached from hydroxyapatite-containing scaffolds, re-seeded in a Boyden Chamber Assay, and evaluated for migration across the transwell membrane over 16 hours. Cells were driven to move across a gradient of DMEM-0%FBS to DMEM-10% FBS. (B) Graph comparing the percentage of migrated cells between cells pre-cultured on HA scaffolds and the same cells treated with IL-8 antibody (20 $\mu\text{g}/\text{mL}$) at the start of the cell migration period. Data are means \pm SD.

together, these data suggest that DCIS cells interacting with HA-mineral exhibit increased motility, an effect that could be regulated by IL-8 signaling.

2.4.6 DCIS xenografts exposed to HA mineral in scaffolds exhibit characteristics associated with increased malignancy

To assess the *in vivo* relevance of the above *in vitro* findings, we subcutaneously implanted DCIS cell-seeded HA mineral-containing and control PLG scaffolds into the contralateral infrascapular regions containing the third pair of mammary glands of immunodeficient female nude mice. After a time period of 4 weeks to enable sufficient tumor progression (35), scaffold-xenografts were excised from the mice and subjected to histopathological analyses (Fig. 2.9A). As

expected, both HA and PLG scaffolds were largely degraded by the endpoint (data not shown) (40). In hematoxylin and eosin (H&E) stains of scaffold-xenograft cross sections, we observed that the PLG control scaffold tumors were typically composed of comedo-type lesions with relatively organized ductal structures (Fig. 2.9B, C), which is comparable to previous non-scaffold-based xenograft studies with the MCF10DCIS.com cell line at this timepoint (35). In contrast, H&E staining revealed significantly disorganized epithelial morphologies within the HA condition (Fig. 2.9B, C). Furthermore, Masson Trichrome staining revealed increased levels of fibrosis within HA scaffold-xenografts (Fig. 2.9D, E). DCIS xenografts initiated in HA scaffolds also presented regions of greater mitotic activity versus DCIS xenografts initiated in PLG scaffolds (Fig. 2.9F). Interestingly, regions that exhibited greater mitoses strongly correlated with regions that were characterized by more fibrosis (Fig. 2.9G). To assess whether IL-8 could be upregulated by the presence of mineral *in vivo*, we also collected the tumor lysates and serum and performed ELISA-based cytokine detection. We found that a subset of mice carrying HA-scaffold xenografts exhibited greater tumor and serum IL-8 relative to their PLG counterparts (Fig 2.9H). Accordingly, there was a correlation between tumor and serum IL-8 concentrations within the HA condition (Fig 2.9H). Collectively, these data suggest that HA mineral may regulate tumor malignancy *in vivo*, as evidenced by decreased epithelial organization, increased desmoplasia, and potentially enhanced IL-8 secretion. Importantly, the results from these scaffold-xenograft studies confirm the pathological relevance of our *in vitro* findings and provide additional evidence that HA-mineral could be actively promoting the malignant progression of breast cancer.

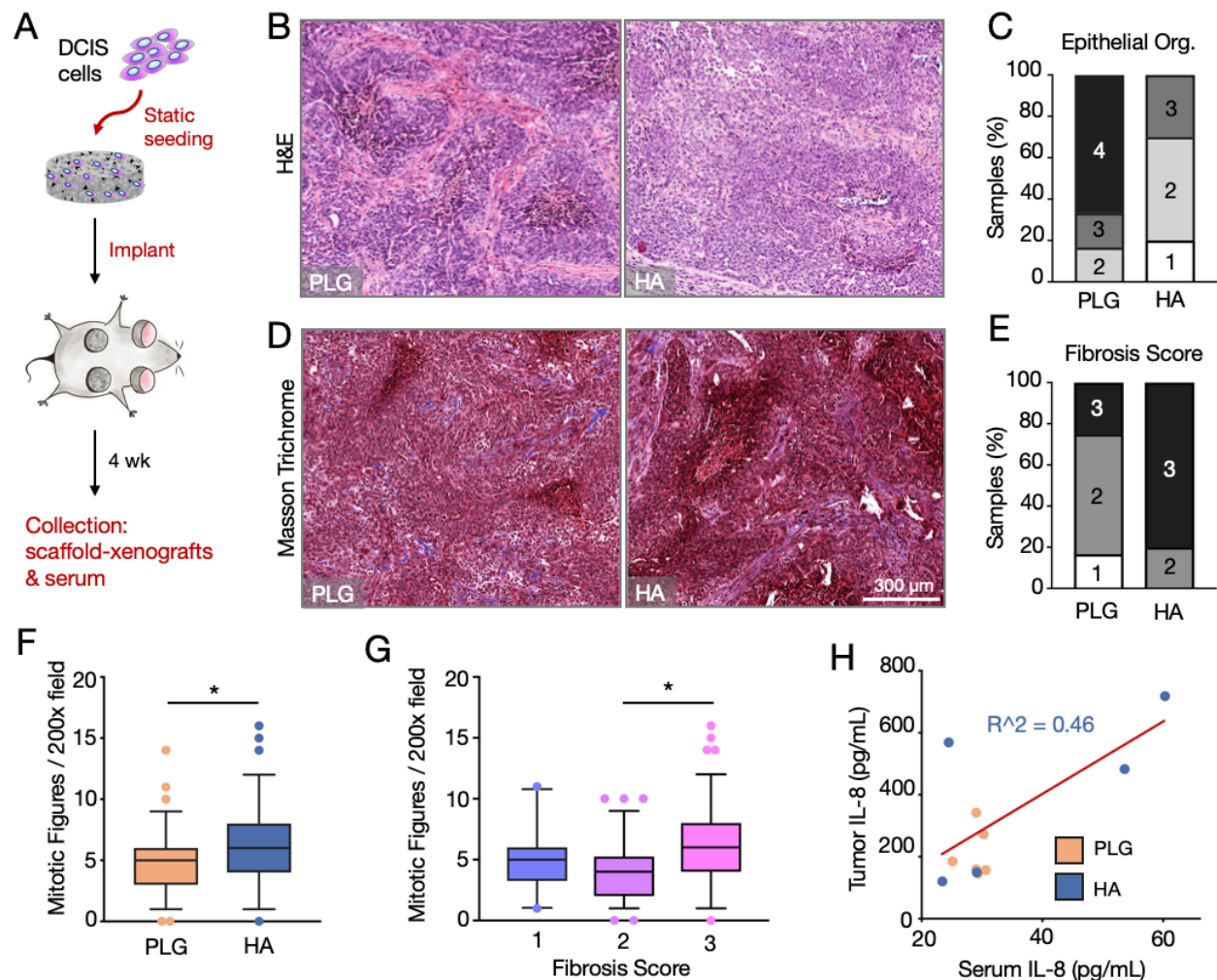


Figure 2.9: DCIS xenografts in hydroxyapatite scaffolds exhibit characteristics associated with increased malignancy. (A) Schematic showing experimental setup for scaffold-xenograft studies: Mineral-containing or control scaffolds seeded with 0.5×10^6 MCF10DCIS.com cells were implanted subcutaneously near the third mammary fat pad. Two scaffolds were implanted per animal. After 4 weeks, scaffold-xenograft tumors and serum were collected for histopathological and biochemical analyses. (B) Representative hematoxylin and eosin (H&E) stained cross sections showing morphology of ducts. (C) Histopathological scoring of the epithelial organization as seen in (B). Rubric: 1-to-4, least-to-most organized, details in methods. PLG vs. HA: $p < 0.05$. (D) Representative Masson Trichrome stained cross sections showing the presence of collagen fibers. (E) Histopathological scoring of the fibrosis as seen in (D). Rubric: 1-to-3, least-to-most fibrosis, details in methods. PLG vs. HA: $p < 0.05$. (F) Box-and-whisker plots showing Mitotic Figures (chromosomes in a given 200x field). Whiskers represent the 5th and 95th percentile. Outlier data points are depicted as dots. (G) Box-and-whisker plots showing Mitotic Figures as a function of Fibrosis Score. Whiskers represent the 5th and 95th percentile. Outlier data points are depicted as dots. (H) Scatter-plot of serum IL-8 vs. tumor IL-8 as detected by ELISA. Correlation as determined by simple linear regression is for HA data points only. For all plots, $*p < 0.05$.

2.5 Discussion

Mammary MCs have been correlated with malignant progression in breast cancer but have thus far been treated solely as passive indicators of cancer. In fact, the vast majority of DCIS cases present with MCs (3), and a recent study analyzing the chemical composition of human DCIS samples have confirmed that these calcifications are HA-based (5). Left untreated, between 14-53% of DCIS will progress to invasive breast cancer (41). However, whether HA MCs can act as active microenvironmental triggers to induce malignant transformation is not clear. This work investigated the hypothesis that HA promotes invasive characteristics within DCIS lesions to facilitate the transition to an overtly malignant condition. By using a tissue-engineered culture model to interrogate cell-mineral interactions in both *in vitro* and *in vivo* experimental settings, we found that HA mineral may stimulate premalignant DCIS cells to develop invasive characteristics through a mechanism that may be dependent on IL-8 signaling.

Previous work has suggested that HA can stimulate secretions of various soluble factors in breast cancer cells (9, 11–13). Our data here suggests that elevated levels of IL-8 may be involved in driving breast cancer disease progression. A number of studies have pointed to a potentially crucial role for IL-8 in metastatic breast cancer, including enrichment of IL-8 in metastatic subpopulations of breast cancer cells (42–45) and high IL-8 levels observed clinically in patients with metastases (27). Additional studies have also shown that IL-8 can play a role in supporting mediators of metastasis in addition to EMT, including angiogenesis (46, 47), hypoxia response (29, 47), and cancer stem cell regulation (43, 48, 49). Although limited by sample size, our IHC analysis of DCIS/IDC samples correlates IL-8 enrichment with the presence of mammographic calcifications and proliferative ductal epithelial. *In vitro* characterization with the PLG scaffold system has shown that HA-mediated IL-8 secretion occurs for breast cancer cell lines with different molecular profiles and malignant characteristics, including MCF10DCIS, MCF10CA1a, MCF-7,

and MDA-MB-231. Interestingly, the non-transformed cell line MCF10A did not exhibit increased IL-8 secretion in the HA-scaffolds, which raises the possibility that MCs may be pro-malignant but may not induce cancerous transformation without additional genetic or environmental drivers.

The observed HA-mediated increase of IL-8 secretion could be regulated by altered integrin engagement during the interaction of breast cancer cells with HA mineral incorporated throughout the scaffolds. Integrins are essential cell adhesion molecules that are known to promote breast cancer metastasis (50). Previous studies have shown that IL-8 secretion is linked to integrin-mediated cell adhesion (46, 51), the dynamics of which are changed in mineralized cell culture systems due to differential protein adsorption onto mineral-containing surfaces (12, 13). Specifically, the $\alpha v\beta 3$ integrin may play a role in regulating IL-8 expression in breast cancer cells exposed to mineral in 3D culture, as our studies indicate a decrease in IL-8 secretion upon treatment of an $\alpha v\beta 3$ antibody antagonist in breast cancer cells cultured within HA scaffolds (Fig. 2.4). Interestingly, it has also been shown that IL-8 in itself can also feedback and increase expression of the $\alpha v\beta 3$ integrin (52, 53), pointing to a possible positive feedback loop between HA-mediated $\alpha v\beta 3$ integrin engagement and IL-8 expression.

The malignant transition of epithelial tumors is characterized by significant changes in tumor cell morphology (54), and previous studies have found that OSCC-3 cells – an aggressive, oral squamous cell carcinoma line – pre-cultured in PLG scaffolds exhibited less differentiated, fibroblastic morphology relative to those cultured in 2D (29). Here we corroborated those findings with MCF10DCIS.com cells (Fig 3B), and additionally observed that the incorporation of HA mineral into the scaffolds further advanced this trend, resulting in cell shapes associated with both mesenchymal and amoeboid morpho-phenotypes (Fig. 2.5B, 2.6) (55). Carcinoma cells are known to rapidly switch between these phenotypic states when moving through a 3D matrix environment

(56), and the significantly increased diversity of cell shapes (Fig. 2.5B, 2.6) that we observed following pre-culture in HA scaffolds could reflect an enhanced morphological plasticity mediated by mineral. We can speculate that the HA-mediated morpho-phenotypes may have imbued the tumor cells with additional modes of motility (56), as a subset of these cells exhibited more persistent movement (Fig. 2.7). Invasive tumor cells can theoretically leverage multiple modes of motility to better respond to physical or biochemical changes in their environments (15). Interestingly, these pre-cultured tumor cells still maintained 3D morpho-phenotypic characteristics during their re-seeded 2D culture periods. This observation supports the idea that HA-mediated changes in phenotypic state may in fact persist across multiple generations (57) and result in more invasive cell colonies even after initial exposure to HA mineral, which often presents heterogeneously in breast tissue (2).

Our studies here also implicate the potential role of IL-8 signaling in the HA-mediated increased in DCIS cell motility. Because our migration studies do not incorporate other cell types or additional soluble factors (Fig. 2.7, 2.8), we posit that these differences in motility were mediated through mechanisms that involve autocrine IL-8 signaling, which is essential for the maintenance of mesenchymal cell states (23) and has been shown to stimulate migratory behavior in both normal endothelial (58) and tumor (59, 60) cells. Additional studies could further investigate how differences in breast cancer cell malignancy affect motogenic responses to IL-8 signaling. One could additionally consider the role of interleukin-6, as it has been recently shown to be working in concert with IL-8 to promote cell migration (61). Although our studies focus exclusively on tumor cell interactions with mineral, future studies could investigate paracrine interactions between tumor cells and neighboring cell types within the context of a mineralized mammary microenvironment.

Microcalcifications are often found in the necrotic cores of breast tumors, likely occurring as a result of unregulated mineralization (5). However, there is evidence to suggest that MC formation may also be an active, cell-mediated process (62) that increases as a function of breast cancer malignancy (63). Interestingly, breast epithelial cells, when induced to acquire mesenchymal characteristics, obtain the ability to produce calcifications (64). Mammary tumors are also known to recruit pro-tumorigenic mesenchymal stem cells (65) that can spontaneously calcify (66, 67). Thus, we can reason that the more malignant the tumor, the more likely that breast cancer cells within that tumor will be exposed to MCs. As we demonstrated in this study with a premalignant cell line model of DCIS, these increased cell-mineral interactions may further accelerate the progression of the malignant phenotype. In our scaffold-xenograft studies, we showed that in addition to a more disorganized epithelial morphology, exposure of tumor cells to HA mineral may also lead to the increased deposition of collagen fibers shown to be linked to the progression of DCIS to IDC (68). However, as DCIS is a highly heterogeneous lesion (69), with spatial variations in pathology, it must be acknowledged that intratumoral cellular responses to HA MCs may differ across patients. In future work, performing a large-scale analysis of calcified tissue samples from controlled patient cohorts of DCIS and IBC will be essential to elucidating the functional connections between HA microcalcifications and the progression of breast cancer.

Using a tissue-engineered approach to model cell-mineral interactions in the breast tumor microenvironment, we here demonstrate that HA mineral promotes invasiveness in a premalignant cell line model of DCIS. This study further validates the use of 3D polymeric scaffolds to study specific microenvironmental parameters that may enable metastasis. Our work implicates HA calcifications as active promoters of malignancy in DCIS and supports the potential use of IL-8 as a prognostic biomarker for breast cancer malignant progression in patients with mammary MCs.

2.6 Acknowledgements

We thank Adrian Shimpi, Matthew Tan, Young Hye Song, and Michael McCoy for technical assistance and Francoise Vermeulen for consulting with statistical analysis. This work was funded by NIH Grant R01CA173083, National Cancer Institute Grants 1U54CA199081-01 and 1U54CA210184-01. The author was supported by an NSF GRFP, an HHMI Med-into-Grad Fellowship, and a US Dept. of Education GAANN Fellowship.

2.7 References

1. Siegel RL, Miller KD, Jemal A (2018) Cancer statistics, 2018. *CA Cancer J Clin* 68(1):7–30.
2. Wilkinson L, Thomas V, Sharma N (2017) Microcalcification on mammography: Approaches to interpretation and biopsy. *Br J Radiol* 90(1069). doi:10.1259/bjr.20160594.
3. Hofvind S, et al. (2011) Mammographic morphology and distribution of calcifications in ductal carcinoma in situ diagnosed in organized screening. *Acta radiol* 52(5):481–487.
4. Tse GM, Tan PH, Cheung HS, Chu WCW, Lam WWM (2008) Intermediate to highly suspicious calcification in breast lesions: A radio-pathologic correlation. *Breast Cancer Res Treat* 110(1):1–7.
5. Kunitake JAMR, et al. (2018) Correlative imaging reveals physiochemical heterogeneity of microcalcifications in human breast carcinomas. *J Struct Biol* 202(1):25–34.
6. Boughey JC, Gonzalez RJ, Bonner E, Kuerer HM (2007) Current Treatment and Clinical Trial Developments for Ductal Carcinoma In Situ of the Breast. *Oncologist* 12(11):1276–1287.
7. Ling H, et al. (2013) Malignant calcification is an important unfavorable prognostic factor in primary invasive breast cancer. *Asia Pac J Clin Oncol* 9(2):139–145.
8. Haka AS, et al. (2002) Identifying Microcalcifications in Benign and Malignant Breast Lesions by Probing Differences in Their Chemical Composition Using Raman Spectroscopy Identifying Microcalcifications in Benign and Malignant Breast Lesions by Probing Differences in Their Che. 5375–5380.
9. Morgan MP, Cooke MM, Christopherson PA, Westfall PR, McCarthy GM (2001) Calcium hydroxyapatite promotes mitogenesis and matrix metalloproteinase expression in human breast cancer cell lines. *Mol Carcinog* 32(3):111–117.
10. Cox RF, et al. (2012) Microcalcifications in breast cancer: Novel insights into the molecular mechanism and functional consequence of mammary mineralisation. *Br J Cancer* 106(3):525–537.
11. Pathi SP, Kowalczewski C, Tadipatri R, Fischbach C (2010) A novel 3-D mineralized tumor model to study breast cancer bone metastasis. *PLoS One* 5(1):1–10.
12. Pathi SP, Lin DDW, Dorvee JR, Estroff LA, Fischbach C (2011) Hydroxyapatite nanoparticle-containing scaffolds for the study of breast cancer bone metastasis. *Biomaterials* 32(22):5112–5122.
13. Choi S, Coonrod S, Estroff L, Fischbach C (2015) Chemical and physical properties of carbonated hydroxyapatite affect breast cancer cell behavior. *Acta Biomater* 24:333–342.

14. Espina V, Liotta LA (2011) What is the malignant nature of human ductal carcinoma in situ? *Nat Rev Cancer* 11(1):68–75.
15. McSherry EA, Donatello S, Hopkins AM, McDonnell S (2007) Molecular basis of invasion in breast cancer. *Cell Mol Life Sci* 64(24):3201–3218.
16. Choi Y, et al. (2013) Epithelial-mesenchymal transition increases during the progression of in situ to invasive basal-like breast cancer. *Hum Pathol* 44(11):2581–2589.
17. Thiery JP (2002) Epithelial–mesenchymal transitions in tumour progression. *Nat Rev Cancer* 2(6):442–454.
18. Polyak K, Weinberg RA (2009) Transitions between epithelial and mesenchymal states: Acquisition of malignant and stem cell traits. *Nat Rev Cancer* 9(4):265–273.
19. Shibue T, Weinberg RA (2017) EMT, CSCs, and drug resistance: The mechanistic link and clinical implications. *Nat Rev Clin Oncol* 14(10):611–629.
20. Thiery JP, Sleeman JP (2006) Complex networks orchestrate epithelial-mesenchymal transitions. *Nat Rev Mol Cell Biol* 7(2):131–142.
21. Mathias RA, et al. (2009) Secretome-based proteomic profiling of Ras-transformed MDCK cells reveals extracellular modulators of epithelial-mesenchymal transition. *J Proteome Res* 8(6):2827–2837.
22. Scheel C, et al. (2011) Paracrine and autocrine signals induce and maintain mesenchymal and stem cell states in the breast. *Cell* 145(6):926–940.
23. Palena C, Hamilton DH, Fernando RI (2013) NIH Public Access. *Futur Oncol* 8(6):713–722.
24. Esquivel-Velázquez M, et al. (2015) The Role of Cytokines in Breast Cancer Development and Progression. *J Interf Cytokine Res* 35(1):1–16.
25. Snoussi K, et al. (2006) Genetic Variation in IL-8 Associated with Increased Risk and Poor Prognosis of Breast Carcinoma. *Hum Immunol* 67(1–2):13–21.
26. Reen ARG, Reen VLG, Hite MCW, Peirs VS (1997) Expression of Cytokine Messenger Rna in Normal and Neoplastic Human Breast Tissue : Identification of Interleukin-8 As a Potential Regulatory Factor in Breast Tumours. 941(December 1996):937–941.
27. Benoy IH, et al. (2004) Increased serum interleukin-8 in patients with early and metastatic breast cancer correlates with early dissemination and survival. *Clin Cancer Res* 10(21):7157–7162.
28. Fernando RI, Castillo MD, Litzinger M, Hamilton DH, Palena C (2011) IL-8 signaling

- plays a critical role in the epithelial-mesenchymal transition of human carcinoma cells. *Cancer Res* 71(15):5296–5306.
29. Fischbach C, et al. (2007) Engineering tumors with 3D scaffolds. *Nat Methods* 4(10):855–860.
 30. Infanger DW, Lynch ME, Fischbach C (2013) Engineered Culture Models for Studies of Tumor-Microenvironment Interactions. *Annu Rev Biomed Eng* 15(1):29–53.
 31. Kim SS, Sun Park M, Jeon O, Yong Choi C, Kim BS (2006) Poly(lactide-co-glycolide)/hydroxyapatite composite scaffolds for bone tissue engineering. *Biomaterials* 27(8):1399–1409.
 32. Schmittgen TD, Livak KJ (2008) Analyzing real-time PCR data by the comparative CT method. *Nat Protoc* 3(6):1101–1108.
 33. Lynch ME, et al. (2016) Three-Dimensional Mechanical Loading Modulates the Osteogenic Response of Mesenchymal Stem Cells to Tumor-Derived Soluble Signals. *Tissue Eng Part A* 22(15–16):1006–1015.
 34. So JY, Lee HJ, Kramata P, Minden A, Suh N (2012) Differential Expression of Key Signaling Proteins in MCF10 Cell Lines, a Human Breast Cancer Progression Model. *Mol Cell Pharmacol* 4(1):31–40.
 35. Hu M, et al. (2008) Regulation of In Situ to Invasive Breast Carcinoma Transition. *Cancer Cell* 13(5):394–406.
 36. Mogilner A, Keren K (2009) The Shape of Motile Cells. *Curr Biol* 19(17):R762–R771.
 37. Rafelski SM, Theriot JA (2004) Crawling Toward a Unified Model of Cell Motility: Spatial and Temporal Regulation of Actin Dynamics. *Annu Rev Biochem* 73(1):209–239.
 38. Kenny PA, et al. (2007) The morphologies of breast cancer cell lines in three-dimensional assays correlate with their profiles of gene expression. *Mol Oncol* 1(1):84–96.
 39. Lourenço BN, et al. (2018) CD44v6 increases gastric cancer malignant phenotype by modulating adipose stromal cell-mediated ECM remodeling. *Integr Biol (United Kingdom)* 10(3):145–158.
 40. Infanger DW, et al. (2013) Glioblastoma stem cells are regulated by interleukin-8 signaling in a tumoral perivascular niche. *Cancer Res* 73(23):7079–7089.
 41. Erbas B, Provenzano E, Armes J, Gertig D (2006) The natural history of ductal carcinoma in situ of the breast: A review. *Breast Cancer Res Treat* 97(2):135–144.
 42. Freund A, et al. (2003) IL-8 expression and its possible relationship with estrogen-receptor-negative status of breast cancer cells. *Oncogene* 22(2):256–265.

43. Charafe-Jauffret E, et al. (2009) Breast cancer cell lines contain functional cancer stem cells with metastatic capacity and a distinct molecular signature. *Cancer Res* 69(4):1302–1313.
44. Singh B, Berry JA, Vincent LE, Lucci A (2006) Involvement of IL-8 in COX-2-Mediated Bone Metastases from Breast Cancer. *J Surg Res* 134(1):44–51.
45. De Larco JE, et al. (2001) A potential role for interleukin-8 in the metastatic phenotype of breast carcinoma cells. *Am J Pathol* 158(2):639–646.
46. Fischbach C, et al. (2009) Cancer cell angiogenic capability is regulated by 3D culture and integrin engagement. *Proc Natl Acad Sci* 106(2):399–404.
47. DelNero P, et al. (2015) 3D culture broadly regulates tumor cell hypoxia response and angiogenesis via pro-inflammatory pathways. *Biomaterials* 55(1):110–118.
48. Al-Hajj M, Wicha MS, Benito-Hernandez A, Morrison SJ, Clarke MF (2003) Prospective identification of tumorigenic breast cancer cells. *Proc Natl Acad Sci* 100(7):3983–3988.
49. Singh JK, Simões BM, Howell SJ, Farnie G, Clarke RB (2013) Recent advances reveal IL-8 signaling as a potential key to targeting breast cancer stem cells. *Breast Cancer Res* 15(4):1–9.
50. Felding-Habermann B, et al. (2001) Integrin activation controls metastasis in human breast cancer. *Proc Natl Acad Sci* 98(4):1853–1858.
51. Lowrie AG, Salter DM, Ross JA (2004) Latent effects of fibronectin, $\alpha 5\beta 1$ integrin, $\alpha V\beta 5$ integrin and the cytoskeleton regulate pancreatic carcinoma cell IL-8 secretion. *Br J Cancer* 91(7):1327–1334.
52. Danhier F, Breton A Le, Pr at V (2012) RGD-based strategies to target alpha(v) beta(3) integrin in cancer therapy and diagnosis. *Mol Pharm* 9(11):2961–2973.
53. Lee CY, et al. (2011) IL-8 increases integrin expression and cell motility in human chondrosarcoma cells. *J Cell Biochem* 112(9):2549–2557.
54. Christofori G (2006) New signals from the invasive front. *Nature* 441(7092):444–450.
55. Friedl P, Wolf K (2010) Plasticity of cell migration: A multiscale tuning model. *J Cell Biol* 188(1):11–19.
56. Paňkova K, R sel D, Novotny M, Brabek J (2010) The molecular mechanisms of transition between mesenchymal and amoeboid invasiveness in tumor cells. *Cell Mol Life Sci* 67(1):63–71.
57. Wu PH, et al. (2015) Evolution of cellular morpho-phenotypes in cancer metastasis. *Sci*

Rep 5(July):1–10.

58. Li A, et al. (2005) Autocrine role of interleukin-8 in induction of endothelial cell proliferation, survival, migration and MMP-2 production and angiogenesis. *Angiogenesis* 8(1):63–71.
59. Li XJ, et al. (2012) As an independent unfavorable prognostic factor, IL-8 promotes metastasis of nasopharyngeal carcinoma through induction of epithelial-mesenchymal transition and activation of AKT signaling. *Carcinogenesis* 33(7):1302–1309.
60. Araki K, et al. (2009) Phosphoglucose isomerase/autocrine motility factor promotes melanoma cell migration through ERK activation dependent on autocrine production of interleukin-8. *J Biol Chem* 284(47):32305–32311.
61. Jayatilaka H, et al. (2017) Synergistic IL-6 and IL-8 paracrine signalling pathway infers a strategy to inhibit tumour cell migration. *Nat Commun* 8(May):1–12.
62. Cox RF, Morgan MP (2013) Microcalcifications in breast cancer: Lessons from physiological mineralization. *Bone* 53(2):437–450.
63. Vidavsky N, et al. (2018) Studying biomineralization pathways in a 3D culture model of breast cancer microcalcifications. *Biomaterials* 179:71–82.
64. Scimeca M, et al. (2014) Microcalcifications in breast cancer: An active phenomenon mediated by epithelial cells with mesenchymal characteristics. *BMC Cancer* 14(1):286.
65. Karnoub AE, et al. (2007) Mesenchymal stem cells within tumour stroma promote breast cancer metastasis. *Nature* 449(7162):557–563.
66. Yoon Y-S (2004) Unexpected Severe Calcification After Transplantation of Bone Marrow Cells in Acute Myocardial Infarction. *Circulation* 109(25):3154–3157.
67. Breitbach M, et al. (2007) Potential risks of bone marrow cell transplantation into infarcted hearts. *Hematology* 110(4):1362–1369.
68. Acerbi I, et al. (2015) Human breast cancer invasion and aggression correlates with ECM stiffening and immune cell infiltration. *Integr Biol (United Kingdom)* 7(10):1120–1134.
69. Cowell CF, et al. (2013) Progression from ductal carcinoma in situ to invasive breast cancer: Revisited. *Mol Oncol* 7(5):859–869.

CHAPTER 3: MULTISCALE CHARACTERIZATION OF THE MINERAL PHASE AT SKELETAL SITES OF BREAST CANCER METASTASIS

Contributors: Aaron E. Chiou, Hyun Chae Loh, Maureen Lynch, Bo Ri Seo, Young Hye Song, Min Joon Lee, Rebecca Hoerth, Emely L. Bortel, Bettina Willie, Georg N. Duda, Lara A. Estroff, Admir Masic, Wolfgang Wagermaier, Peter Fratzl, and Claudia Fischbach

3.1 Abstract

Skeletal metastases, the leading cause of death in advanced breast cancer patients, depend on tumor cell interactions with the mineralized bone extracellular matrix. Bone mineral is largely comprised of hydroxyapatite (HA) nanocrystals with physicochemical properties that vary significantly by anatomical location, age, and pathology. However, it remains unclear whether bone regions typically targeted by metastatic breast cancer feature distinct HA materials properties. Here we combined high resolution X-ray scattering analysis with large area Raman imaging, backscattered electron microscopy, histopathology, and micro-computed tomography to characterize HA in mouse models of advanced breast cancer in relevant skeletal locations. The proximal tibial metaphysis served as a common metastatic site in our studies; we identified that in disease-free bones this skeletal region contained smaller and less oriented HA nanocrystals relative to ones that constitute the diaphysis. We further observed that osteolytic bone metastasis led to a decrease in HA nanocrystal size and perfection in remnant metaphyseal trabecular bone. Interestingly, in a model of localized breast cancer, metaphyseal HA nanocrystals were also smaller and less perfect than in corresponding bone in disease-free controls. Collectively, these results suggest that skeletal sites prone to tumor cell dissemination contain less mature HA (i.e., smaller, less perfect, and less oriented crystals) and that primary tumors can further increase HA immaturity even prior to secondary tumor formation, mimicking alterations present during tibial

*Published as He F et al (2017) Multiscale characterization of the mineral phase at skeletal sites of breast cancer metastasis. *Proceedings of the National Academy of Sciences*, 114(40): 10542-10547.

metastasis. Engineered tumor models recapitulating these spatiotemporal dynamics will permit assessing the functional relevance of the detected changes to the progression and treatment of breast cancer bone metastasis.

3.2 Introduction

Eighty percent of advanced breast cancer patients develop metastases in bone (1). Following dissemination to the skeleton, metastatic breast cancer cells intimately interact with bone cells to facilitate seeding and expansion while disrupting homeostatic bone remodeling (1–3). The early stage-colonization of disseminated tumor cells appears to depend on active osteogenesis and adhesion to osteoblasts (4), whereas the eventual transition to macro-metastasis involves a vicious cycle that promotes osteolytic activity through the aberrant activation of osteoclasts (1–3). While most studies have focused on identifying the cellular and molecular mechanisms underlying bone metastasis (1–4), very little is known about how breast cancer and bone metastasis alter the physical properties of the mineralized bone extracellular matrix (ECM).

The basic building block of the bone ECM is a nanocomposite of collagen fibrils and co-aligned mineral crystals that underlie a unique hierarchical structure (5, 6). Primarily composed of carbonated hydroxyapatite ($\text{Ca}_5(\text{PO}_4, \text{CO}_3)_3(\text{OH})$) (HA), these mineral crystals are elongated platelets with thicknesses of approximately 2-7 nm and with lengths on the order of 15-200 nm (5, 7). The physicochemical properties of HA (i.e., crystallinity, chemical composition, size, aspect ratio, arrangement) dictate bone mechanical properties (5) and can vary as a function of disease, diet, age and anatomical location (8–13). Notably, HA crystal size and orientation increase with bone tissue maturity (11–13). These variations, in turn, may modulate tumor progression. Studies with synthetically defined cell culture substrates have suggested that breast cancer cell adhesion, proliferation, and osteolytic factor expression are regulated by the materials

properties of HA nanocrystals (14–16). However, the physiological relevance of these *in vitro* observations is unclear as it remains unresolved whether bone metastasis-relevant sites feature specific nanoscale HA materials properties and if these properties vary with cancer.

Previous *in vivo* studies of bone metastasis have utilized micro-computed tomography (μ CT) or dual-energy X-ray absorptiometry to assess various bone indices such as bone mineral density, bone volume fraction, and trabecular number or thickness (17, 18). While these techniques have yielded important insights, they are not capable of resolving bone mineral properties at the nanometer length scale. We sought to address this gap in knowledge by employing X-ray scattering, a non-destructive technique which can quantitatively assess the size (thickness via the T-parameter and length via the L-parameter) and arrangement (orientation via the ρ -parameter) of bone mineral nanocrystals (11, 19) (Fig. 3.1). To account for the spatial heterogeneity of bone mineral (5), X-ray scattering instruments can be programmed to scan larger micron-scale regions of interest. This technique has greatly contributed to the understanding of bone biomineralization, as it has been widely used to characterize HA nanocrystal structure across a range of organisms (e.g., humans, mice, rats, baboons, minipigs, turkeys) (5) and has shown that even very small changes to these nanostructural features are linked to pathological conditions (20). Here, we have combined X-ray scattering with complementary imaging techniques that include large area Raman imaging, backscattered electron microscopy (BSE), histology, and μ CT. This multiscale approach allowed us to correlate HA nanostructural differences with bone tissue chemical composition and mineral crystallinity as well as cellularity and global changes in mineral distribution (Fig. 3.2). These studies provide the most detailed to date assessment of bone hierarchical structure as it pertains to breast cancer and bone metastasis.

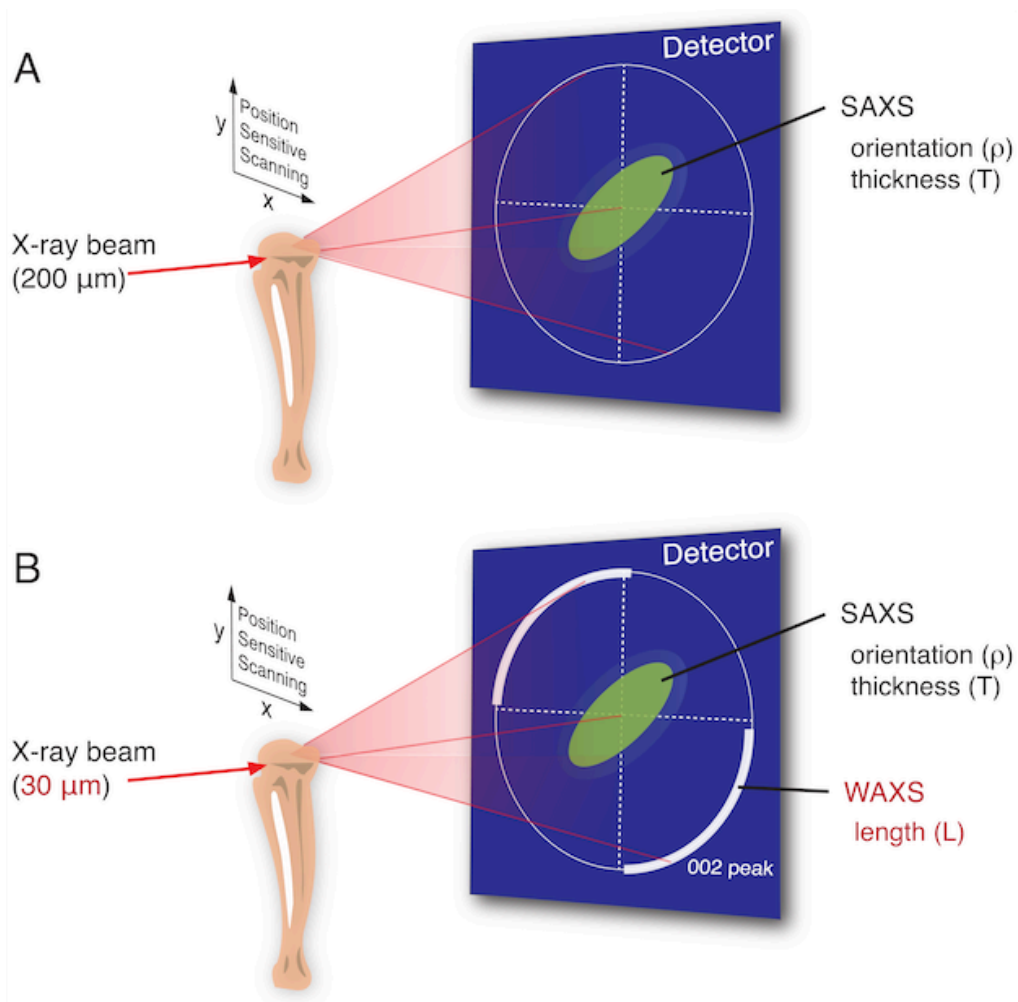


Figure 3.1: X-ray scattering analysis setup. (A, B) Bone specimens are exposed to highly collimated X-rays in a stepwise manner on the x- and y- plane perpendicular to the direction of the incident beam. The scattered light registers on a 2D detector and can then be used to derive information about mineral nanostructure. Laboratory-based SAXS analysis (A) provides information about mineral orientation (ρ) and thickness (T). Synchrotron-based SAXS/WAXS analysis (B) provides enhanced spatial resolution and, in addition to orientation and thickness, information about mineral nanocrystal length (L) derived from the width of the 002 peak.

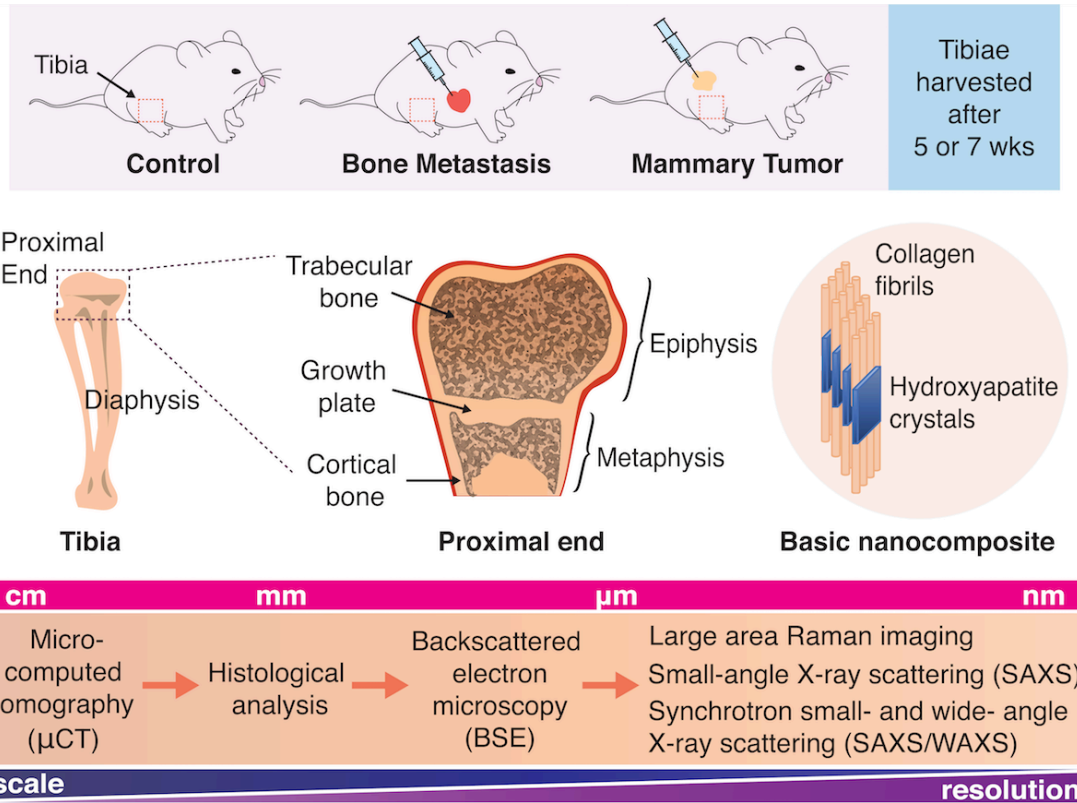


Figure 3.2: Experimental setup for multiscale analysis of bone hierarchical structure. Different stages of human breast cancer were modeled in immunocompromised nude mice. To achieve bone metastasis, luciferase-labeled BoM1-2287 cells were intracardially injected, while injection into cleared mammary fat pads resulted in localized mammary tumors without overt metastasis. Mouse tibiae harvested after 5 or 7 weeks were embedded in polymethylmethacrylate (PMMA) and subjected to micro-computed tomography (μCT), histological analysis, and backscattered scanning electron microscopy (BSE) to assess macro- to micro-scale changes in bone structure. Small- and wide-angle X-ray scattering (SAXS and WAXS) as well as large area Raman imaging were used to characterize bone nanostructure and physicochemical composition.

3.3 Materials and Methods

3.3.1 Tibiae from mouse xenograft models of breast cancer

Three week-old, female BALB/c athymic nude mice from Taconic Biosciences were used for animal studies. To recapitulate either bone metastasis or localized breast cancer in these mice, two different surgical techniques were employed. To generate secondary, bone-metastatic tumors, luciferase expressing BoM1-2287 cells (10^5 cells in 100 μ L PBS) were injected into the left ventricles of the hearts (one injection per mouse). Tibiae were harvested after 5 weeks. To assess the effects of a primary mammary tumor, luciferase expressing BoM1-2287 cells (0.75×10^6 cells in 20 μ L of DMEM, 10% FBS, 1% antibiotic) were injected into cleared and contralateral mammary fat pads (two injections per mouse). Tibiae were harvested after 7 weeks. Tumor cell localization was determined by bioluminescent imaging: mice were intraperitoneally injected with Luciferin (150 mg/kg, Gold Biotechnology) and then imaged after a 5-minute incubation period (Xenogen IVIS-200). Age-matched mice were used as controls. Immediately following harvest, tibiae were stored in 70% ethanol for 48 hours and embedded in polymethylmethacrylate (PMMA) by the Analytical Microscopy Core Laboratory at the Hospital for Special Surgery. All animal studies were performed in accordance with Cornell University animal care guidelines.

3.3.2 Micro-computed tomography (μ CT)

Mouse tibia specimens were scanned using two quantitative μ CT systems. Bone metastatic tibiae were scanned with the Skyscan 1172 (BrukerCT, Kontich, Belgium) while control and mammary tumor tibiae were scanned with the Scanco μ CT35 (Scanco Medical AG, Brüttisellen, Switzerland). Tibiae were scanned at moderate isotropic resolutions of either 10 or 15 μ m. To obtain high-contrast images, the X-ray source was set to a voltage of 55 kV and a current of 145 μ A. To reduce the effects of beam hardening, a 0.5 mm aluminum filter was used.

Avizo Fire 8.1 (FEI-Company, Oregon, USA) was used to assess macroscopic architecture following 3D reconstruction of the 2D slices. A sample size of $n = 3$ was used to compare trabecular bone outcomes, which included bone volume fraction (BV/TV), trabecular thickness (Tb.Th), and trabecular separation (Tb.Sp), between control and mammary tumor groups.

3.3.3 Backscattered electron microscopy (BSE)

The PMMA sample blocks were cut to expose a longitudinal section of the entire bone. An environmental scanning electron microscope (ESEM) (FEI-Company, Oregon, USA) was employed under low-vacuum conditions in backscattered mode at a working distance of 10 mm with electron beam energies of 10 kV and 12.5 kV. Grayscale images of mineralized tissue were captured, with regions of high calcium content appearing brighter than regions of low calcium content.

3.3.4 Histological studies

Movat's Pentachrome staining was performed on 5 μm longitudinal sections of the PMMA-embedded samples. The following tissue types were stained: bone (yellow), cartilage (blue to green), and fibrous connective tissue (pink to purple). Representative specimens were imaged with an Axioskop 2 microscope (Carl Zeiss Microscopy GmbH, Germany).

3.3.5 Small-angle X-ray scattering measurements (SAXS)

Longitudinal sample sections $\sim 200 \mu\text{m}$ thick were mounted approximately 600 mm from the detector and perpendicular to the X-ray beam path. An X-ray generator (Brucker, AXS, Karlsruhe, Germany) with a rotating copper anode operating at 40 kV and 100 mA (Cu K-alpha radiation) produced a beam with a wavelength of 1.5418 \AA . An X-ray radiograph was used to select points of measurement. For each sample, approximately 80-100 points to sufficiently map

the proximal tibiae was selected along with 5-10 points in the diaphysis. A two-pinhole setup with a focal diameter of 200 μm collimated the X-ray beam. The scattering signal was recorded for 3600 s by a position sensitive area detector (HI-STAR, Bruker AXS, Karlsruhe, Germany, pixel size 105.26x105.26 μm^2). Calculation of the beam center was achieved by using a silver behenate standard. A sample size of $n = 3$ was used for both control and mammary tumor groups. Image files were analyzed with AutoFit (proprietary Fit2D-based software by the Max Planck Institute of Colloids and Interfaces, Potsdam, Germany). The T- (mean mineral crystal thickness) and ρ - (degree of alignment) parameters were calculated as previously described (11, 19). To consistently assess mineral nanostructure of the metaphyseal bone, all data points that were distally within 1000 μm of the growth plate were considered for analysis.

3.3.6 Synchrotron measurements (SAXS/WAXS)

The previously prepared 200 μm thick sections were further polished to obtain ~ 50 μm thick sections. Measurements were obtained at the BESSY II (Berliner Elektronenspeicherring-Gesellschaft für Synchrotronstrahlung, Helmholtz-Zentrum Berlin, Germany). The instrument produced a 30 μm beam with a wavelength of 0.82656 Å. The samples were positioned approximately 300 mm from the detector and perpendicular to the beam path. An X-ray radiograph was used to select points of measurement. For each sample, roughly 150 measurement points from mineralized tissue on both distal and proximal sides of the growth plate were selected along with 5 points in the diaphysis. The scattering signal was recorded for 90 s with a position sensitive CCD-detector (MarMosaic 225, Mar USA Evanston, USA, pixel size 73.242x73.242 μm^2). Instrument calibration and beam center localization were determined by a quartz standard. The raw scattering data was then corrected for ring current variations. A sample size of $n = 4$ was used for both control and mammary tumor groups. Image files were

analyzed with AutoFit. The T- (mean mineral crystal thickness), ρ - (degree of alignment), and L- (mean mineral crystal length) parameters were calculated as previously described (11, 19) and then normalized to the sample means of the corresponding parameter values for diaphyseal cortical bone to control for variability between animals. To investigate tumor-mediated effects at the growth plate region, all data points that were within 50 μm of the growth plate cartilage were considered for comparison with corresponding data points in control samples.

3.3.7 Statistical analysis of X-ray scattering data

Because mouse tibiae were measured in multiple regions and repeatedly measured within these regions, a mixed model accounting for both fixed and random effects was used. The fixed effects were the 1) disease-state, 2) region, and 3) interaction between the disease-state and the region. The random effects were the 1) mouse and 2) region nested within each mouse. Contrasts were subsequently run to compare either the regions of interest within each disease state or the disease state within each region of interest. A Bonferroni correction was applied to adjust for multiple comparisons. The correlation between T-parameter with ρ -parameter was performed using a simple linear regression ($n = 148$). $p < 0.05$ were considered statistically significant. JMP 12 (SAS Institute Inc, Cary, NC, USA) and Graphpad Prism 5 (GraphPad Software, San Diego, CA) were used for all statistical analyses, which were performed in consultation with an independent statistician at the Cornell Statistical Consulting Unit.

3.3.8 Large area Raman imaging

Representative samples were chosen for supplementary analysis via Raman imaging. Raman spectra were collected using a WiTec Alpha300 Raman system. A continuous 532 nm laser beam was focused on select regions of 5 μm longitudinal sections. Each spectrum was acquired with an accumulation time of 0.33 seconds per point using a CCD behind a grating

(600g/mm) spectrometer (WITec UHTS Raman Spectrometer) with a spectral resolution of 4 cm⁻¹. Raman maps were generated with a spatial resolution of 2 μm. The WiTec Project 4.1 software was used for image processing and analysis. To avoid the effect of cosmic rays and other aberrations when averaging spectra, data smaller or greater than 3σ from the mean were excluded, which constituted less than 3% of the data. Background resin spectra was subtracted from the raw data for better fitting. PO₄ v1 (960 cm⁻¹), amide I (1677 cm⁻¹) and amide III (1256 cm⁻¹) peaks (21, 22) were fitted with Gaussian functions and their full width at half maximums (FWHM) as well as intensities were extracted. Bone tissue with phosphate intensities above 120 CCD counts were used for further analysis. Phosphate peak FWHM⁻¹ and phosphate-to-amide ratio (PO₄/Amide I) were calculated at each point. For segmentation analysis, the metaphyseal bone was divided into 10 segments with increasing distance from the growth plate. After excluding outlier data, the means and standard deviations of each segment were calculated. A two-sample t-test was used to assess differences in regions of interest.

3.3.9 Analysis of mouse tibiae from cell-free tumor conditioning

Five-week-old, female NOD.SCID mice from Jackson Laboratories were used for animal studies. Animal studies were performed in accordance with Cornell University animal care guidelines. For three weeks, mice received daily intraperitoneal injections of tumor-derived media (TCM) or blank media control. To generate TCM for injections, MDA-MB-231 breast cancer cells (ATCC) at 90% confluency were incubated in low-serum DMEM supplemented with 1% FBS (Atlanta Biologicals) and 1% penicillin/streptomycin (P/S, Invitrogen) for 12 hours. Conditioned media was collected, concentrated 10-fold in an Amicon centrifugal filter unit (MWCO 3 kDa, EMD Millipore), and subsequently diluted 5-fold with low-serum DMEM. Blank low-serum DMEM were processed similarly (Control) for mice receiving control

injections. Tibiae were harvested and fixed in 10% neutral buffered formalin for 48 hours, and decalcified in ethylenediaminetetraacetic acid (10% EDTA, pH 7.4). Tartrate-resistant acid phosphatase (TRAP) staining for osteoclasts and Picrosirius Red staining for collagen were performed on paraffin-embedded sections. Images of TRAP-stained sections were captured using a Scanscope digital slide scanner (Aperio, Vista, CA, USA). TRAP+ osteoclasts were counted and normalized to bone perimeter (N.Oc/B.Pm). Metaphyseal and diaphyseal regions of Picrosirius Red stained sections were imaged under cross-polarized light (Eclipse TE2000-S, Nikon, Melville, NY, USA), and green and red integrated density was measured using ImageJ to quantify thin/immature and thick/mature collagens, respectively. Metaphyseal measurements for each sample were normalized to respective diaphyseal measurements. Sample size was at least $n = 5$ for each group. Collagen content in mouse tibiae was measured over two sections with two images per section. The resulting data was analyzed using a mixed model with random effect of 1) mouse and 2) section nested within mouse. The fixed effect was condition (between mouse variable). The response was log-transformed to better fit the assumptions of the model (normality of residuals, constant variance). Student's t-test was used to analyze TRAP staining data. $p < 0.05$ were considered statistically significant. JMP 12 (SAS Institute Inc, Cary, NC, USA) was used for statistical analyses, which were performed in consultation with an independent statistician at the Cornell Statistical Consulting Unit.

3.3.10 In vitro assessment of osteogenic differentiation

TCM derived from MDA-MB-231 and the BoM1-2287 subline (Bone-TCM) were collected after 24 hours and processed as above, but instead diluted 5-fold into osteogenic induction media (low-serum DMEM supplemented with 50 μM ascorbic acid, 0.1 μM dexamethasone, 10 mM β -glycerophosphate). Bone marrow-derived mesenchymal stem cells

(3.1×10^3 cells/cm², Lonza) were treated with the prepared TCM, Bone-TCM, or Control for 3 weeks, after which cells were fixed and stained with Alizarin Red S (ARS) to visualize and quantify matrix calcification colorimetrically following extraction of ARS with 10% acetic acid. Sample size was n = 3 for all groups. One way ANOVA with Tukey's multiple comparisons was used to analyze ARS data. $p < 0.05$ were considered statistically significant. Graphpad Prism 5 (GraphPad Software, San Diego, CA, USA) was used for statistical analysis.

3.4 Results

3.4.1 In tibiae of healthy mice, HA nanocrystals are more immature in regions prone to metastasis

In experimental mouse models of breast cancer bone metastasis, the tibia is a common site of secondary tumor formation (23, 24). Within the tibia, disseminated cancer cells appear to preferentially localize to the metaphysis rather than the diaphysis (23, 24), a phenomenon that has been attributed to specific cellular properties of metaphyseal blood vessels and an enrichment of chemoattractants (25). What is unclear, however, is whether the physical nature of bone mineral also varies between the metaphysis, which is largely comprised of trabecular bone, and the diaphysis, which is primarily dense cortical bone (26). To address this question, we applied laboratory-based small-angle X-ray scattering (SAXS) analysis (Fig. 3.1A) to establish a baseline of differences in HA nanocrystal thickness and orientation (Fig. 3.3A) between metaphyseal and diaphyseal bone in the tibiae of disease-free mice. We observed that mineral crystals in the metaphysis were significantly thinner (indicated by decreased T-parameter) and less oriented (indicated by decreased ρ -parameter) than those in the diaphysis (Fig. 3.3B-D). In fact, crystals that were thinner were also less oriented (Fig. 3.3B), suggesting that the development of HA thickness and orientation occur in parallel. Our results are in strong agreement with previous studies that identified HA nanostructural heterogeneity in murine long

bones (11, 27). The relative immaturity of metaphyseal HA crystals is consistent with their close proximity to the ossification center and the high turnover rate of metaphyseal trabecular bone (26). As breast cancer cells can adhere and proliferate better on smaller and less perfect HA nanoparticles (14), the detected differences in metaphyseal versus diaphyseal HA nanostructure may be functionally relevant to the preferential metastatic tumor cell colonization of the proximal tibia.

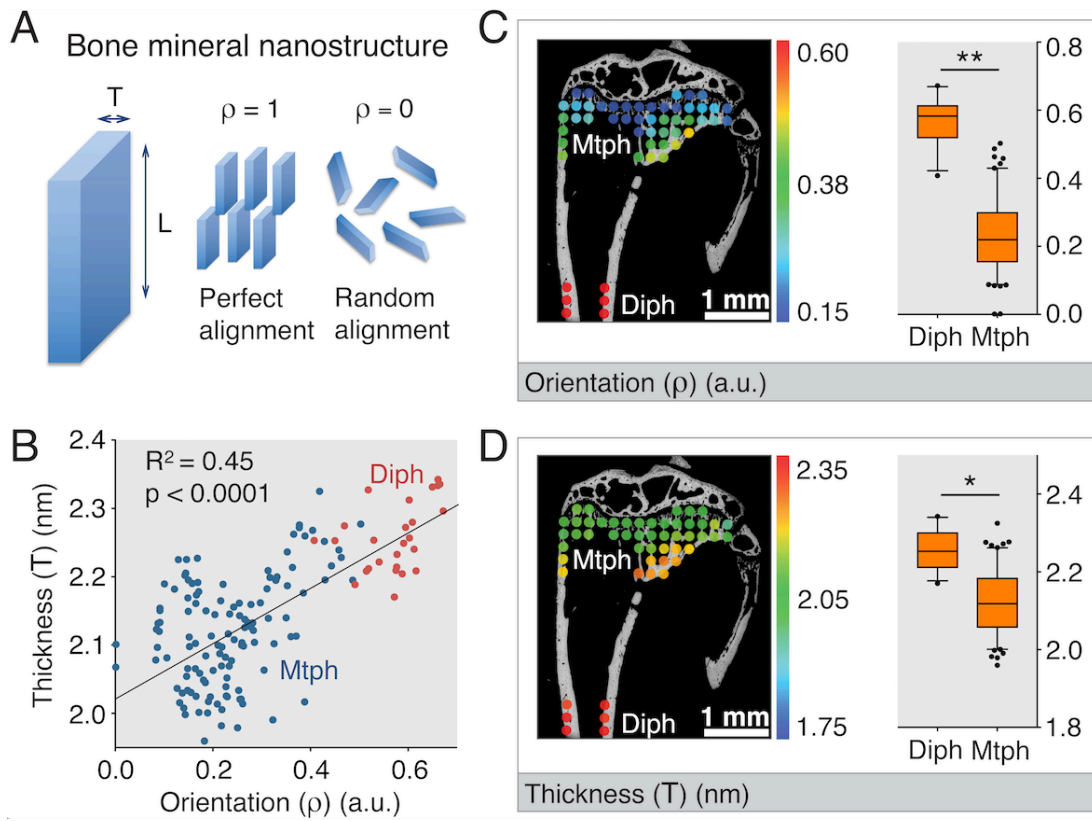


Figure 3.3: Laboratory-based SAXS analysis of tibiae from healthy mice shows that hydroxyapatite nanocrystals in the metaphysis are more immature than ones in the diaphysis. (A) X-ray scattering techniques provide information on bone mineral nanostructure. (B) Correlation analysis between T-parameter and ρ -parameter as determined by simple linear regression. Data points represent individual measurements. The data is color-partitioned into two regions of interest ('Diph' = diaphysis; 'Mtph' = metaphysis). (C, D) Spatial representation of quantitative data. Representative ρ -parameter (mean mineral crystal orientation) (C) and T-parameter (mean mineral crystal thickness) (D) data are overlaid on corresponding BSE images. Color scales: Warmer colors indicate greater crystal orientation (C) or thickness (D). Box-and-whisker plots of all ρ -parameter (C) and T-parameter (D) data from the regions of interest. Whiskers represent the 5th percentile and the 95th percentile. Outlier data points are depicted as dots. * indicates $p < 0.05$. ** indicates $p < 0.001$.

3.4.2 Metastasis initiation in the proximal tibial metaphysis alters the bone ECM

We next performed a multiscale characterization of tibial metastasis to identify tumor-mediated changes of bone ECM in these sites. To achieve bone metastasis, we injected luciferase-expressing BoM1-2287 breast cancer cells, a bone metastatic subpopulation of the MDA-MB-231 cell line (24), into the left ventricle of the mouse heart. As expected, this approach resulted in the reliable formation of macro-metastasis in the proximal tibiae of immunocompromised BALB/c nude mice after 5 weeks (24) (Fig. 3.4A).

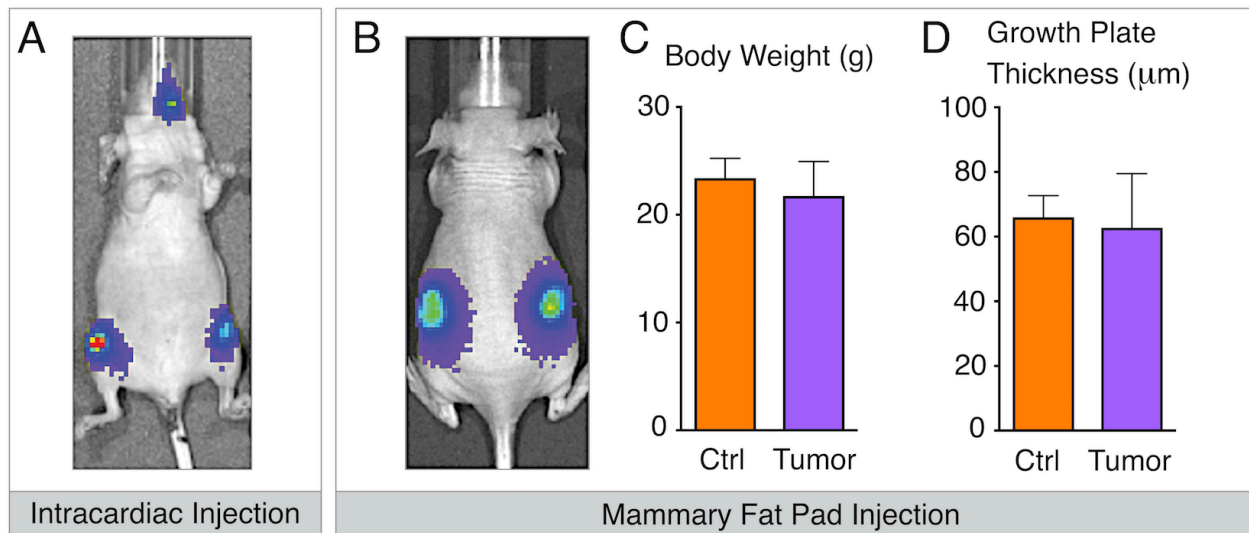


Figure 3.4: Mouse models of advanced breast cancer. To determine localization via bioluminescence imaging, luciferase-expressing bone metastatic breast cancer cells (BoM1-2287) were used in both conditions. (A) Injection of tumor cells into the left ventricle of the heart consistently resulted in metastasis to the hind limbs and to the brain. Animal is shown in dorsal recumbency. Tibiae were harvested 5 weeks post-surgery. (B) Injection of tumor cells into a pair of contralateral mammary fat pads resulted in localized tumors only. No macro-metastatic colonies were observed using this method. Animal is shown in ventral recumbency. Tibiae were harvested 7 weeks post-surgery. (C) Average body weights one day prior to bone harvest. ‘Ctrl’ = control mice; ‘Tumor’ = mammary fat pad-injected mice. In the ‘Tumor’ group, the weight of the tumor was subtracted from the total weight. $p = 0.41$. (D) Average growth plate thicknesses in the proximal tibiae. ‘Ctrl’ = control mice; ‘Tumor’ = mammary fat pad-injected mice. $p = 0.73$. (C, D) Data are means \pm SD ($n = 4$). Student’s t-test was used to confirm statistical significance between groups. Statistical analysis was performed in Graphpad Prism 5 (GraphPad Software, San Diego, CA).

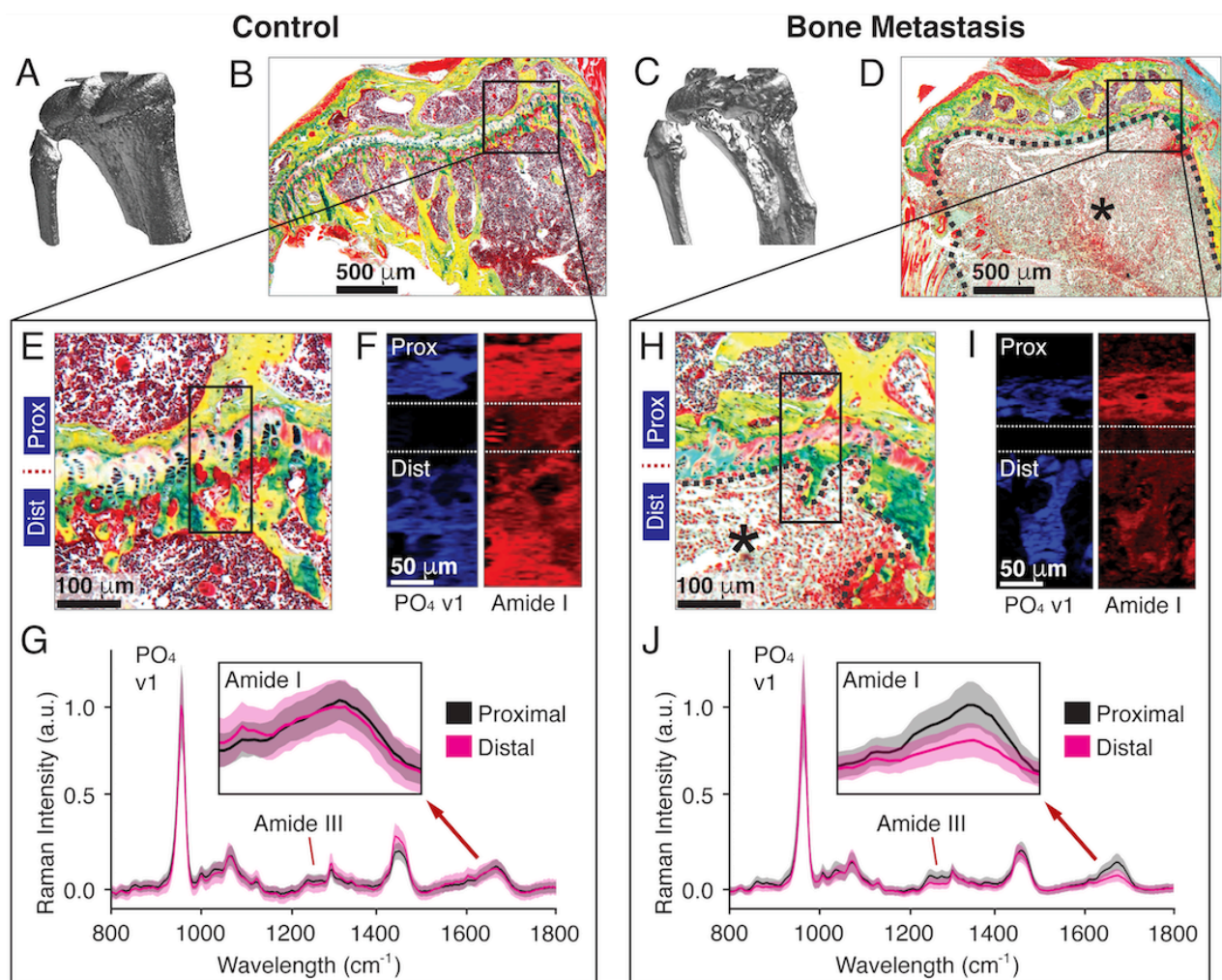


Figure 3.5: Multiscale characterization of the bone metastatic site identifies changes in the extracellular matrix associated with secondary tumor formation. (A-D) Macro- to micro-scale qualitative analysis: Representative μ CT images (A, C) and Movat's Pentachrome (MP) stained cross-sections (B, D). Color legend of the MP stain: yellow – bone; green – calcified cartilage; black – nuclei; intense red – muscle; red/pink – fibrous tissue. The metastasized tumor is highlighted by the black asterisk and outlined with dashed lines (D). (E-J) Nanoscale quantitative analysis: Large area Raman imaging of defined regions (black insets) (E, H). 'Prox' and 'Dist' (E, F, H, I) indicate bone on the proximal (i.e., the epiphysis) and distal (i.e., the metaphysis) sides of the growth plate, respectively. The metastasized tumor is highlighted by the black asterisk and outlined with dashed lines (H). False color heat maps (F, I): Blue and red depict the intensities of the PO_4 v1 and amide I peaks, respectively. Mean Raman spectra (bold line: means; fill areas: SD) (G, J) of the indicated bone regions with insets (range: $1600\text{--}1700\text{ cm}^{-1}$) highlighting the amide I peak (1677 cm^{-1}).

μ CT scans (Fig. 3.5A, 3.5C), Movat's Pentachrome staining (Fig. 3.5B, 3.5D, 3.6), and BSE images (Fig. 3.7) revealed massive degradation of metaphyseal trabecular bone. Viewed at these length scales, macro-metastatic outgrowths were largely contained in the metaphysis, did

not occur in the epiphysis (Fig. 3.6), and left diaphyseal cortical bone unaffected (Fig. 3.7). Growth plate integrity was severely compromised in bone metastasis versus control samples as suggested by the presence of fibrous tissue (28) rather than the organized arrays of chondrocyte columns (Fig. 3.6). These observations support the possibility that disseminated tumor cells preferentially entered the tibiae through sinusoidal vessels supplying the metaphyseal trabecular bone (25), and that the growth plate acted as a barrier preventing tumor cell advancement to the epiphysis.

We were specifically interested in characterizing the compositional and structural properties of tumor-interfacing bone remnants of what was once a mesh of metaphyseal trabecular bone (Fig. 3.6, 3.7). To this end, we used large area Raman imaging to compare the chemical signatures of trabecular bone proximal (i.e., the epiphysis) and distal (i.e., the metaphysis) to the growth plate in control and metastasis conditions (Fig. 3.5E-J).

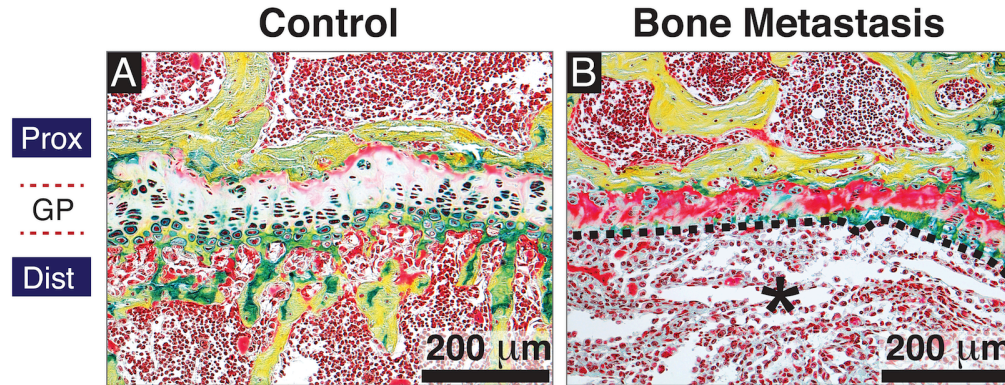


Figure 3.6: Representative Movat's Pentachrome (MP) stained cross-sections show massive destruction of metaphyseal trabecular bone and severe disruption of the epiphyseal chondrocytes in tibiae with metastasis. (A, B) Color legend of the MP stain: yellow – bone; green – calcified cartilage; black – nuclei; red/pink – fibrous tissue. 'GP' refers to the location of the growth plate. 'Prox' and 'Dist' indicate bone on the proximal (i.e., the epiphysis) and distal (i.e., the metaphysis) sides of the growth plate, respectively. The metastasized tumor (B) is highlighted by the black asterisk and outlined with dashed lines.

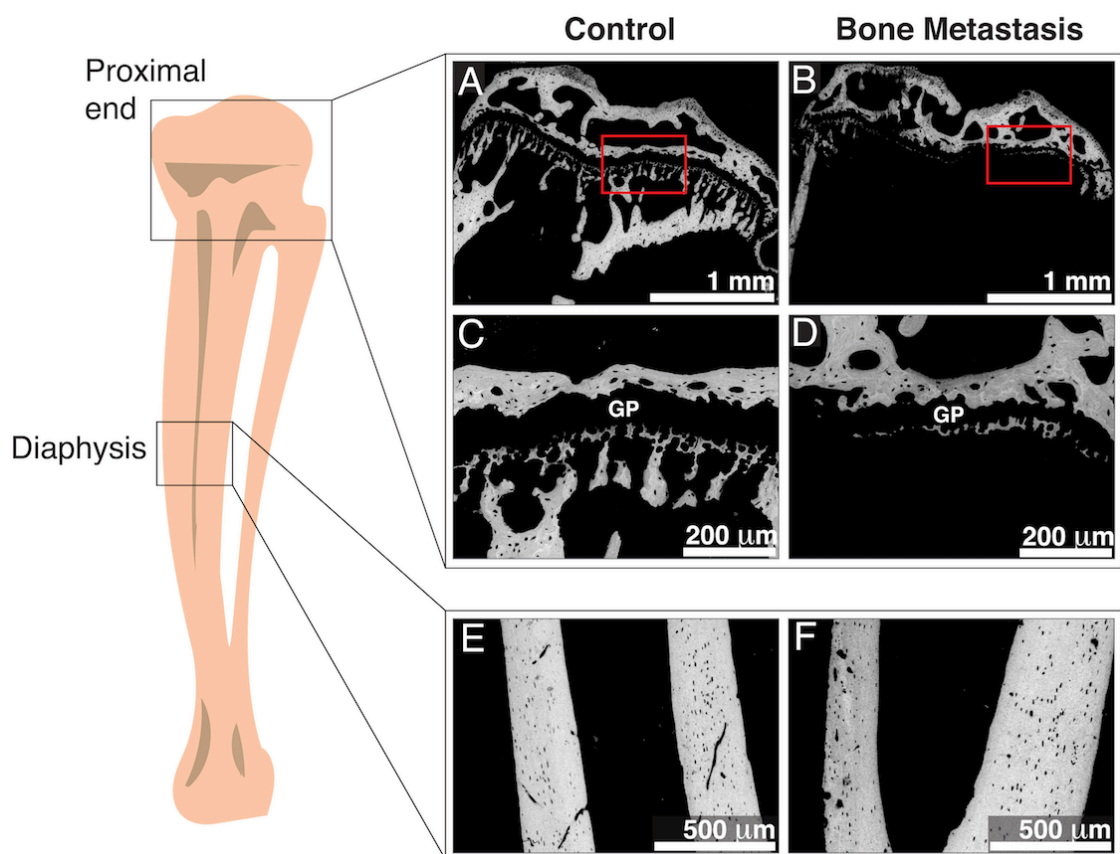


Figure 3.7: The metaphysis experiences severe degradation during bone metastasis while the diaphysis remains unaffected. Representative backscattered scanning electron microscopy (BSE) images of the proximal tibia (*A-D*) and diaphysis (*E, F*) from control mice (*A, C*) and mice with bone metastasis (*B, D*). Panels *C* and *D* show the regions defined by the red insets in *A* and *B*, respectively. ‘GP’ labels the growth plate.

Interestingly, in both control and tumor-bearing tibiae, we observed that the intensity of the PO_4 v1 peak (960 cm^{-1}) was comparable between the metaphysis and the epiphysis (Fig. 3.5F, 3.5I). This result suggests that the immediate presence of a tumor has little effect on the mineral content of the remaining bone (21). In contrast, we found pronounced spectral differences in the amide I peak (1677 cm^{-1}), a proxy for collagen type I content (21), between the metaphysis and epiphysis of metastasis-associated bones (Fig. 3.5I, 3.5J). Because the intensity of the amide I peak is polarization-dependent and may be affected by polarization orientation of the incident beam, we also assessed the intensity of the polarization-independent amide III peak (1256 cm^{-1}) (21, 22), which exhibited a concomitant decrease (Fig. 3.8B). In contrast, the amide

I and III peaks were virtually unaffected in the tibial metaphysis of control mice (Fig. 3.5F, 3.5G, 3.8A). Hence, a significant increase in the phosphate-to-amide ($\text{PO}_4/\text{Amide I}$) ratio ($p < 0.05$) was observed in the bone metastasis condition versus the control condition (Fig. 3.9). Collectively, these data suggest a decrease in collagen relative to mineral content within bone that is in physical contact with the secondary tumor.

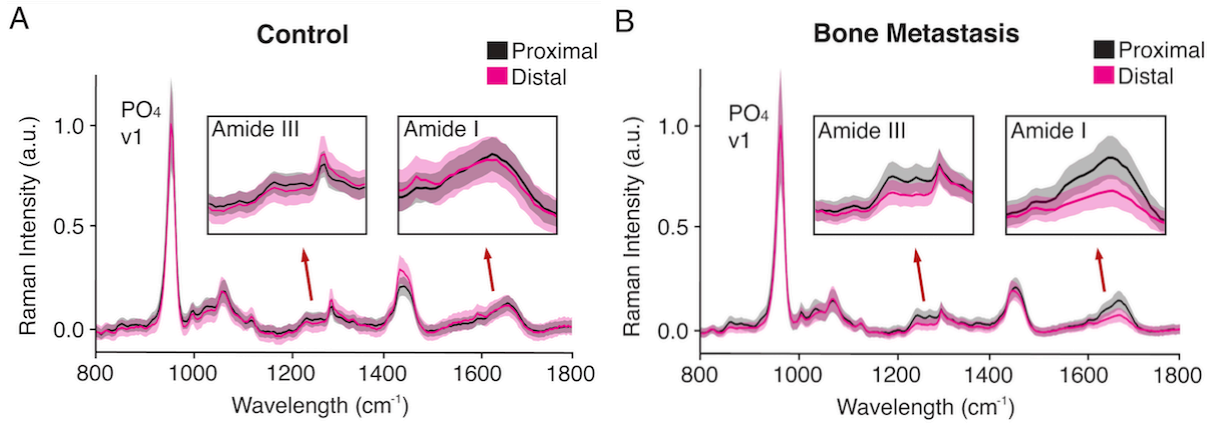


Figure 3.8: Collagen type I content is decreased in metaphyseal bone that is interfacing with the secondary tumor. Raman spectroscopy of bone proximal (i.e., the epiphysis) and distal (i.e., the metaphysis) to the growth plate in control (A) and bone metastasis (B) conditions. Mean Raman spectra with insets (1200 – 1330 cm^{-1} ; 1600 – 1700 cm^{-1}) highlighting the amide III (1256 cm^{-1}) and amide I (1677 cm^{-1}) peaks, respectively. The bold lines represent the means and the fill areas represent the respective standard deviations.

While the mineral content in the remnant bone tissue may have not been affected by the immediate presence of a tumor (Fig. 3.5I, 3.7, 3.9B), bone mineral nanostructure may still have been impacted (9, 10, 29). As such, we were also interested in assessing changes in HA nanostructure within metastasis-associated bone remnants. Targeting these bone remnants with X-ray scattering techniques proved technically infeasible, however. As an alternative, we derived mineral crystallinity – a measure of HA nanocrystal maturity – from the inverse of the Raman PO_4 v1 peak full width at half maximum (FWHM) (9, 30). This parameter positively correlates

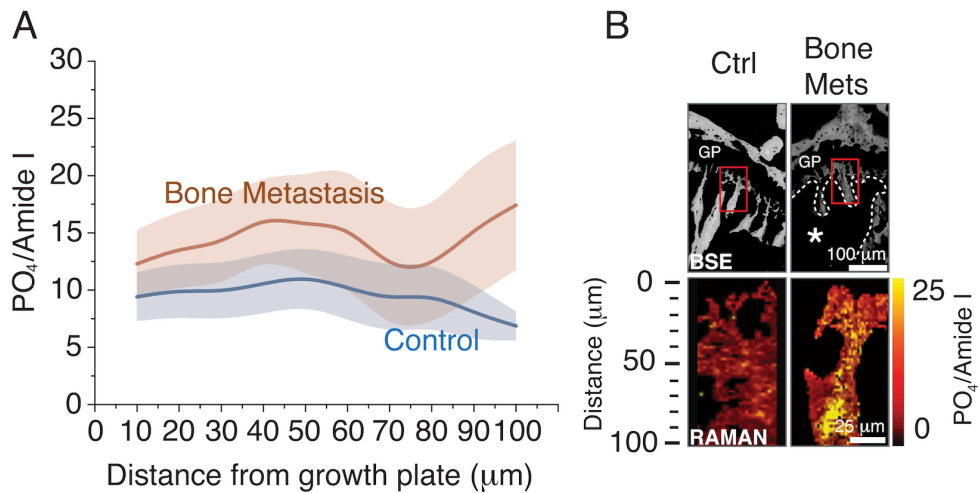


Figure 3.9: Large area Raman imaging indicates that the phosphate-to-amide ratio (PO₄/Amide I) is increased in metaphyseal bone interfacing with a secondary tumor. (A) PO₄/Amide I as a function of distance from the growth plate. The bold lines represent the means and the fill areas represent the respective standard deviations. (B) PO₄/Amide I visualized by heat-maps of the region highlighted in the red insets. ‘Ctrl’ = control; ‘Bone Mets’ = bone metastasis. Backscattered scanning electron microscopy images (BSE): ‘GP’ labels the growth plate. The metastasized tumor is indicated by the white asterisk and outlined with dashed lines. Raman heat-maps (RAMAN): ‘Distance’ refers to the proximity to the growth plate. Lighter colors indicate a greater phosphate-to-amide ratio.

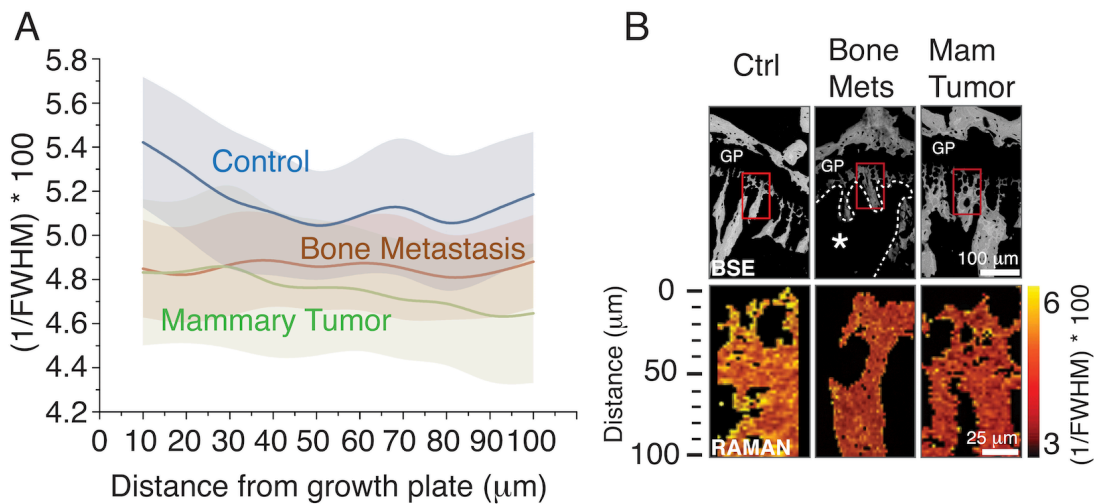


Figure 3.10: Large area Raman imaging indicates that metaphyseal bone mineral crystallinity (FWHM⁻¹*100 of the PO₄ v1 peak) is decreased in mice with localized mammary tumors as well as in mice with bone metastasis. (A) Crystallinity as a function of distance from the growth plate. The bold lines represent the means and the fill areas represent the respective standard deviations. (B) Crystallinity visualized by heat-maps of the region highlighted in the red insets. ‘Ctrl’ = control; ‘Mam Tumor’ = mammary tumor; ‘Bone Mets’ = bone metastasis. Backscattered scanning electron microscopy images (BSE): ‘GP’ labels the growth plate. The metastasized tumor is indicated by the white asterisk and outlined with dashed lines. Raman heat-maps (RAMAN): ‘Distance’ refers to the proximity to the growth plate. Lighter colors indicate greater mineral crystallinity.

with the stoichiometric perfection and length of the crystallites along the *c*-axis (30). Interestingly, we found that mineral crystallinity in the bone remnants was markedly decreased ($p < 0.05$) in the bone metastasis condition relative to the control (Fig. 3.10). Taken together, the immediate presence of a tumor may promote the decrease of mineral maturity along with reduced collagen content.

3.4.3 Metaphyseal HA nanostructure is altered by the presence of a localized mammary tumor

Next, we asked if the bone ECM can be altered by the presence of a localized primary tumor. While previous studies of bone metastasis have shown that circulating biomolecules can modulate bone cell activity (31) and bone collagen remodeling (32), our focus here was to investigate the possibility of pre-metastatic changes in the mineral nanostructure of bone. To recapitulate a scenario of breast cancer without evident bone metastases, we implanted the same BoM1-2287 cells into the mammary fat pads of BALB/c nude mice, which, over a period of 7 weeks, enabled primary tumor growth but did not result in metastatic outgrowth (33) (Fig. 3.4B) or the physical wasting associated with cachexia (Fig. 3.4C). Complementary techniques with resolutions spanning the macro- to micro-length scales did not reveal primary tumor-mediated changes in metaphyseal bone. Histological staining, BSE imaging, and μ CT analysis suggested that the cellular composition (Fig. 3.11A), mineral density (Fig. 3.11A), and trabecular bone structure (Fig. 3.11B) was similar between the tibial metaphysis of control mice and mice carrying primary mammary tumors.

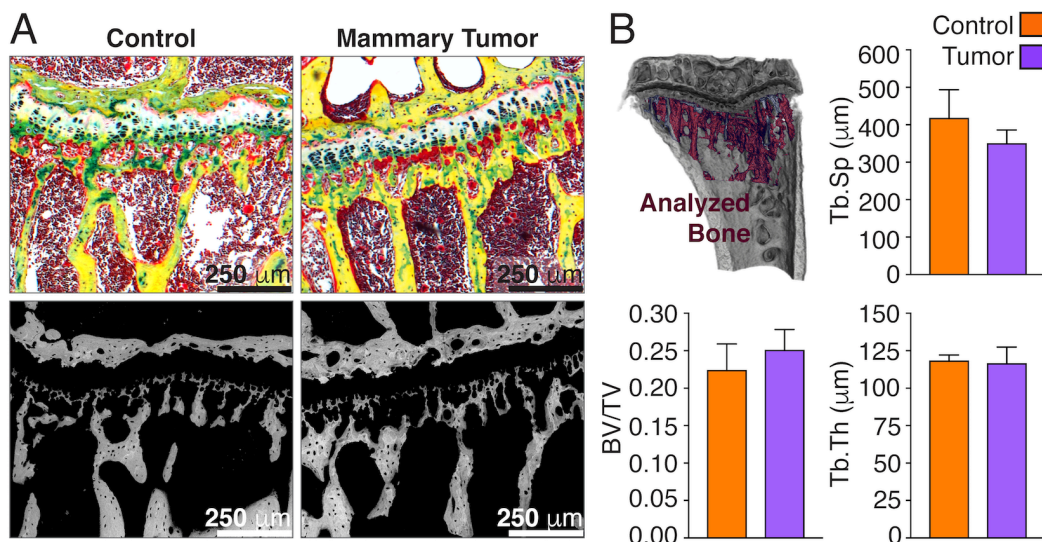


Figure 3.11: Macro- to micro-scale analysis of metaphyseal bone suggests no structural differences between control mice and mice with mammary tumors. (A) Representative images of Movat's Pentachrome-stained cross sections and BSE images of comparable regions of trabecular bone in the proximal tibia. (B) μ CT analysis of the trabecular bone highlighted in dark purple. Graphs represent the means \pm SD of bone volume fraction (BV/TV), trabecular thickness (Tb.Th), and trabecular separation (Tb.Sp) data.

We then used X-ray scattering analysis to examine potential primary tumor-mediated changes in bone nanostructure. Laboratory-based SAXS did not indicate differences in HA nanocrystal orientation and thickness in metaphyseal bone between control and mammary tumor groups (Table 3.1). However, since tumor-mediated differences in the mineral phase could conceivably occur on extremely small length scales, we hypothesized that the spatial resolution of laboratory-based SAXS (Fig. 3.1A) may have been insufficient to detect these possible changes in HA.

Parameter	Region	Control (mean \pm SD)	Mammary tumor (mean \pm SD)	<i>P</i> value (control vs. tumor)
ρ , a.u.	Diaphysis	0.587 \pm 0.066	0.522 \pm 0.102	0.30
	Metaphysis	0.246 \pm 0.003	0.283 \pm 0.036	0.40
T, nm	Diaphysis	2.268 \pm 0.052	2.279 \pm 0.016	0.66
	Metaphysis	2.131 \pm 0.027	2.091 \pm 0.064	0.26

Table 3.1: Summary of ρ - and T-parameter data from laboratory-based SAXS analysis

Therefore, we next analyzed the samples using scanning synchrotron-based small- and wide-angle X-ray scattering (SAXS/WAXS) (Fig. 3.1B). In addition to providing information on mineral crystal thickness and orientation from SAXS, this approach also enables the derivation of the mineral crystal length (L-parameter) from WAXS (Fig. 3.1B). Given that the growth plate is a region of high metabolic activity and mineralization (26), we focused our analysis on the HA mineral within 50 μm of the growth plate cartilage. Here, we observed tumor-mediated changes in mineral crystal nanostructure, which were dependent on the location of the scanned mineral (Fig. 3.12). More specifically, HA mineral crystals immediately distal to the growth plate were significantly shorter in tibiae from mice with mammary tumors versus control mice (Fig. 3.12B). A downward though non-significant trend was also detected in both mineral crystal orientation ($p = 0.33$) (Fig. 3.12C) and thickness ($p = 0.56$) (Fig. 3.12D). This observed decrease in HA nanocrystal size was corroborated with Raman imaging measurements of corresponding bone regions, which suggested that mineral crystallinity was decreased ($p < 0.05$) in the mammary tumor condition relative to that of the control (Fig. 3.10). Furthermore, these differences mimicked measurements of mineral crystallinity in the bone remnants physically adjoined to a metastatic tumor mass (Fig. 3.10). During murine bone development, HA crystals undergo large increases in length while thickness stays relatively constant (11), which could suggest that HA length is more susceptible to aberrant perturbations. Interestingly, these tumor-mediated changes were only observed in the tissue distal but not proximal to the growth plate (Fig. 3.12B-D), which is consistent with the preferential initiation of secondary tumors in the metaphysis rather than in the epiphysis (Fig. 3.5, 3.6).

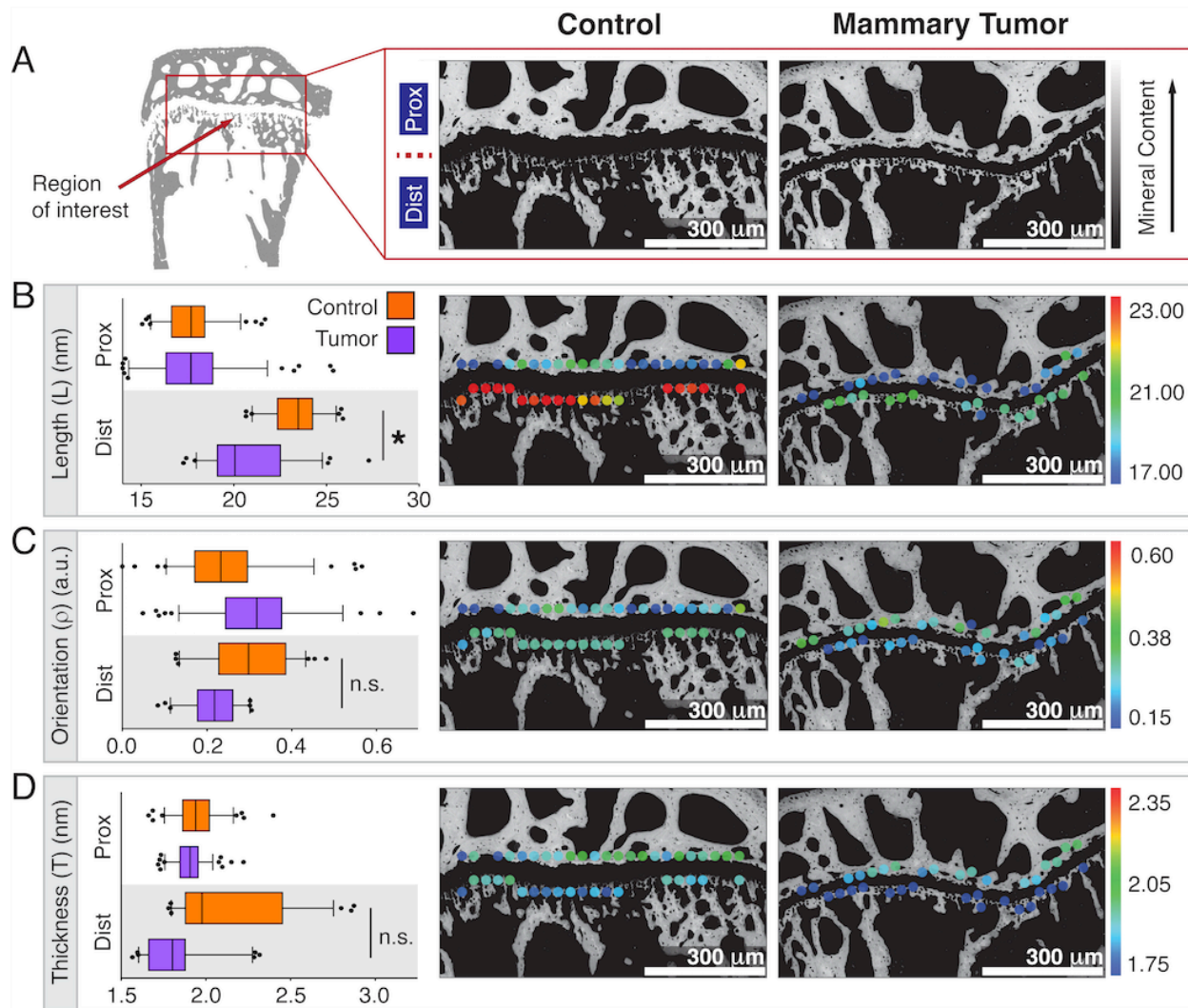


Fig. 3.12: Scanning synchrotron-based SAXS/WAXS analysis of metaphyseal tissue bordering the growth plate reveals shorter hydroxyapatite nanocrystals in mice carrying mammary tumors. (A) Representative BSE images of the region of interest. ‘Prox’ and ‘Dist’ indicate the proximal and distal sides of the growth plate, respectively. (B-D) Spatial representation of quantitative data. Box-and-whisker plots summarize all L-parameter (mean mineral crystal length) (B), ρ -parameter (mean mineral crystal orientation) (C), and T-parameter (mean mineral crystal thickness) (D) data. Whiskers represent the 5th and the 95th percentile. Outlier data points are depicted as dots. * indicates $p < 0.05$. n.s. indicates non-significance. Representative L-parameter (B), ρ -parameter (C), and T-parameter (D) data are overlaid on corresponding BSE images. Color scales: Warmer colors indicate greater crystal length (B), orientation (C) or thickness (D).

To explore possible mechanisms by which a mammary tumor could remotely alter metaphyseal bone mineral, we assessed markers of bone matrix remodeling in tibiae harvested from mice systematically conditioned with daily intraperitoneal injections of tumor-derived media over the course of 3 weeks. Picrosirius Red-stained cross sections of the proximal tibiae revealed a significant increase in the collagen content of metaphyseal trabecular bone (Fig. 3.13A) while TRAP staining of this same region revealed no difference in the number of osteoclasts (Fig. 3.13B). These data suggest that in a skeletal region prone to metastasis, circulating tumor-derived factors can lead to an increase in local osteogenesis, while leaving bone resorption unaffected.

Accordingly, culturing bone marrow-derived mesenchymal stem cells (MSCs) in the same tumor-derived media resulted in elevated matrix calcification via Alizarin Red S staining when compared to controls (Fig. 3.13C), which is indicative of tumor factor-mediated osteogenic differentiation. Importantly, this trend was more pronounced ($p < 0.05$) when MSCs were cultured in media from the bone metastatic cells used in our bone mineral characterization studies (BoM1-2287) relative to the parental cell line (Fig. 3.13C). Taken together, these results imply that factors secreted from bone metastatic breast cancer cells can aberrantly promote local osteogenesis by altering the fate of bone marrow-residing MSCs. Increased osteogenesis may explain the enhanced HA immaturity at metastatic sites, as newly formed bone is typically comprised of smaller, less perfect, and less oriented HA crystals (7).

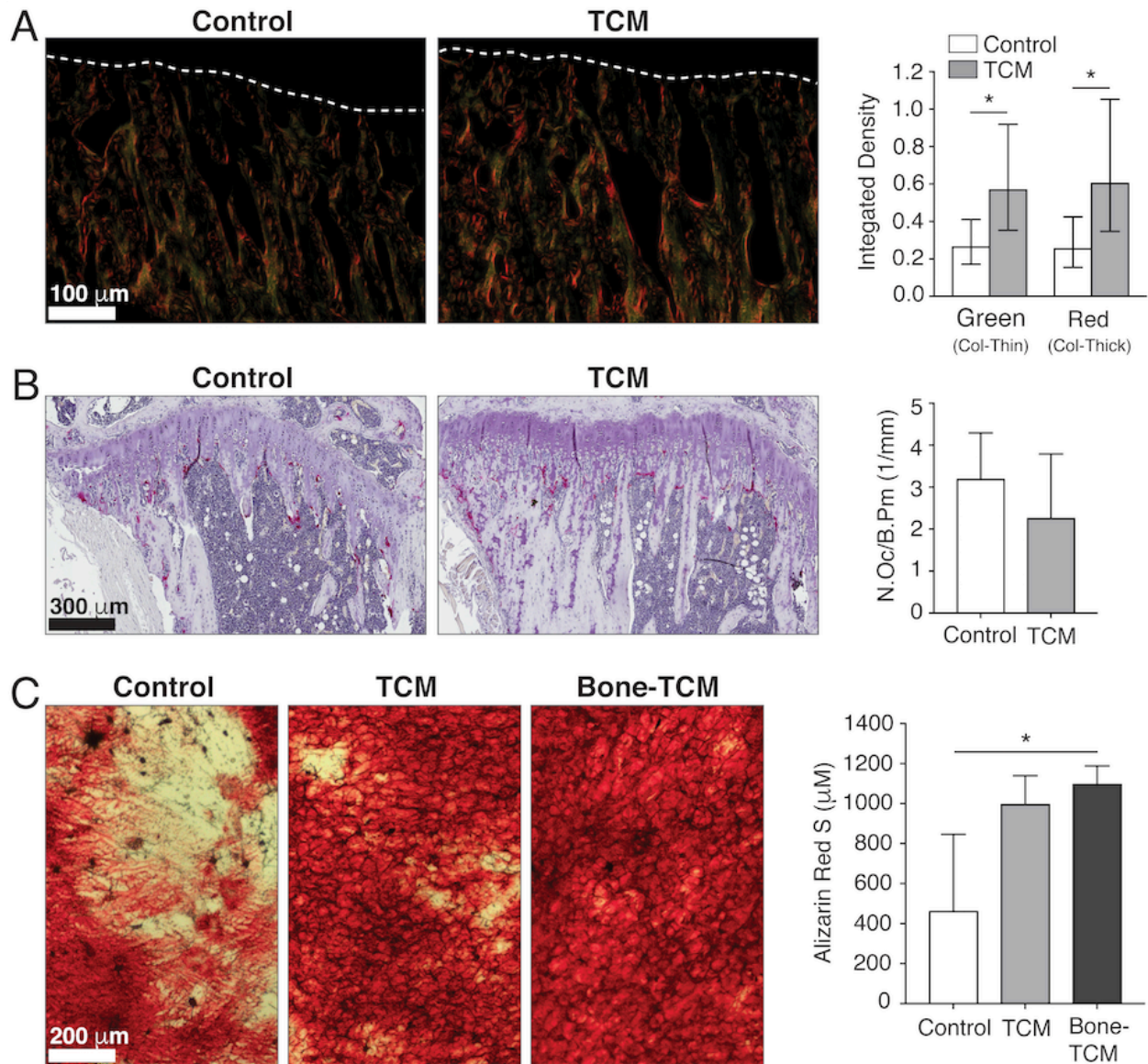


Figure 3.13: Tumor-secreted factors can promote osteogenic activity. (A) Representative Picrosirius Red-stained cross sections of metaphyseal trabecular bone in tibiae harvested from control mice (Control) or mice injected with media conditioned by parental MDA-MB-231 (TCM) cells. The growth plate border is indicated by the white dotted line. Graphs represent the back-transformed predicted means with 95% confidence interval of green and red integrated density measurements for thin/immature and thick/mature collagens, respectively. Data are normalized to regions of diaphyseal bone. * indicates $p < 0.05$. (B) Representative TRAP-stained (pink) cross sections (with hematoxylin counterstain) of either Control or TCM tibiae. Graphs represent quantification (mean \pm SD) of number of osteoclasts normalized to bone perimeter (N.Oc/B.Pm). (C) Representative images of Alizarin Red S stain (ARS) in bone marrow-derived mesenchymal stem cells treated with control media (Control) or conditioned media from parental MDA-MB-231 breast cancer cells (TCM) or BoM1-2287 (Bone-TCM). Red color indicates positive stain for matrix calcification. Graphs represent mean \pm SD of ARS extracted from stained matrices. * indicates $p < 0.05$.

3.5 Discussion

Interactions between breast cancer cells and the bone microenvironment are critical to the pathogenesis of skeletal metastases but the associated nanostructural changes of bone mineral remain unclear. Gaining an improved understanding of this potential relationship is critical as HA nanocrystal properties can significantly alter cellular phenotypes (14–16) and thus, conceivably affect malignancy. Using a combination of high-resolution analytical techniques to characterize tibiae from mouse models of bone metastatic and localized breast cancer, we show that the nanostructure of HA crystals varies between anatomical regions that are more and less prone to metastatic colonization, and that primary tumors may reinforce these variations even prior to metastatic outgrowth.

The observation that breast cancer cells preferentially colonize the proximal tibial metaphysis may have broader pathological relevance. Adjacent to a secondary ossification center and enriched with trabecular bone (26), the tibial metaphysis of young mice can exemplify a distinct anatomical site of high bone turnover (i.e., resorption of old bone followed by formation of new bone). Clinicians have long observed preferential metastatic localization to sites of active remodeling (34), such as the trabecular bone-rich pelvis and spinal vertebral bodies (2, 34). As the nanostructure of human and murine bone mineral is similar (5, 11), it is likely that HA crystals in these metabolically more active human skeletal sites are also more immature. Future studies will need to confirm this possibility and assess the functional role of HA materials properties in driving secondary tumor formation in these sites.

Furthermore, our SAXS/WAXS and Raman data point to a potential mammary tumor-mediated increase of local osteogenesis in the initial trabecular network prior to secondary tumor formation. This finding supports experimental evidence by others that primary tumors can activate pre-metastatic remodeling of the bone, and that these changes ultimately promote

metastatic dissemination (31, 32). While these previous studies of mammary tumor-mediated changes focused on bone cell activity (31) and circulating markers of bone collagen remodeling (32), our data now additionally suggest that structural changes occur in the mineral phase of bone. More specifically, we observed a decrease in mineral nanocrystal size in the metaphyseal bone tissue bordering the growth plate. Since these changes occurred at a bone growth front, these data indicate that a localized mammary tumor may be affecting the mineralization of new matrix. In bone, the deposition of HA results from a thermodynamically driven cascade that may involve the initial formation of disordered, less stable nanoparticulate phases that become more crystalline and increase in size as they progress to the final mineral phase (35, 36). As such, a mammary tumor could conceivably decrease general mineral maturity by releasing factors that stimulate osteogenic cells to increase their production of new bone (Fig. 3.13), which typically consists of smaller, less perfect and less oriented HA crystals (7). Alternatively, the physiological maturation of bone mineral could also be directly inhibited by soluble factors secreted by the mammary tumor. The glycoprotein osteopontin is a potential candidate, as it is highly expressed by the BoM1-2287 cells (24) used in this study and is known to inhibit the growth of HA mineral (37). Furthermore, changes in HA nanostructure may have been due to mammary tumor-mediated effects on the longitudinal bone growth of the young mice (38) used in our studies. However, given the similarities in growth plate thicknesses (Fig. 3.4D) and trabecular network properties (Fig. 3.11A, 3.11B) between control tibiae and mammary tumor-associated tibiae, the metabolic program of growth plate chondrocytes and the consequent rate of endochondral ossification (39) appear to be unaffected by the primary tumors. Taken together, our results suggest that the primary mammary tumor could induce the formation of less mature bone mineral in the absence of a secondary tumor, likely without changing overall skeletal growth.

Pre-metastatic, primary tumor-mediated changes in nanoscale bone mineral properties may be an underappreciated mechanism that could play a role in the initial establishment and survival of a secondary tumor colony in the bone. Because metastatic breast cancer cells exhibit increased proliferation and adhesion on smaller and less perfect HA nanocrystals (14), these early-stage changes of bone mineral may promote the initial seeding and survival of disseminated tumor cells. Furthermore, the deposition of a more immature mineral phase that is more susceptible to osteolytic degradation (40, 41) could facilitate the vicious cycle of bone metastasis, thus promoting tumor outgrowth. Complemented by our previous work suggesting that nanoscale HA materials properties can influence breast cancer malignant progression (14–16), we propose a modified view of the vicious cycle of bone metastasis in which HA materials properties are functionally linked with the pathogenesis of breast cancer bone metastasis (Fig. 3.14). Detailed *in vivo* studies will be needed to conclusively define the functional consequences of our observations. Nevertheless, our results bring to light that nanostructural parameters of the bone metastatic site are currently underappreciated, but should be considered when studying the microenvironmental complexities that influence bone metastasis.

While others have previously reported that breast cancer can remotely engender bone destruction (17, 31, 32), we now further advance this field of work by quantifying tumor-mediated changes in HA nanostructure in skeletal locations associated with metastasis. The findings here may inform future therapeutic strategies. For instance, adjuvant prescription of antiresorptive drugs such as bisphosphonates (BPs) are currently largely palliative and do not improve patient survival rate (1). BPs, which are taken up by bone-resorbing osteoclasts, localize to mineralized tissue by selectively binding to HA (1). As molecular simulation studies show that BP-HA binding energies are dependent on HA nanocrystal size (42), BP therapeutic efficacy

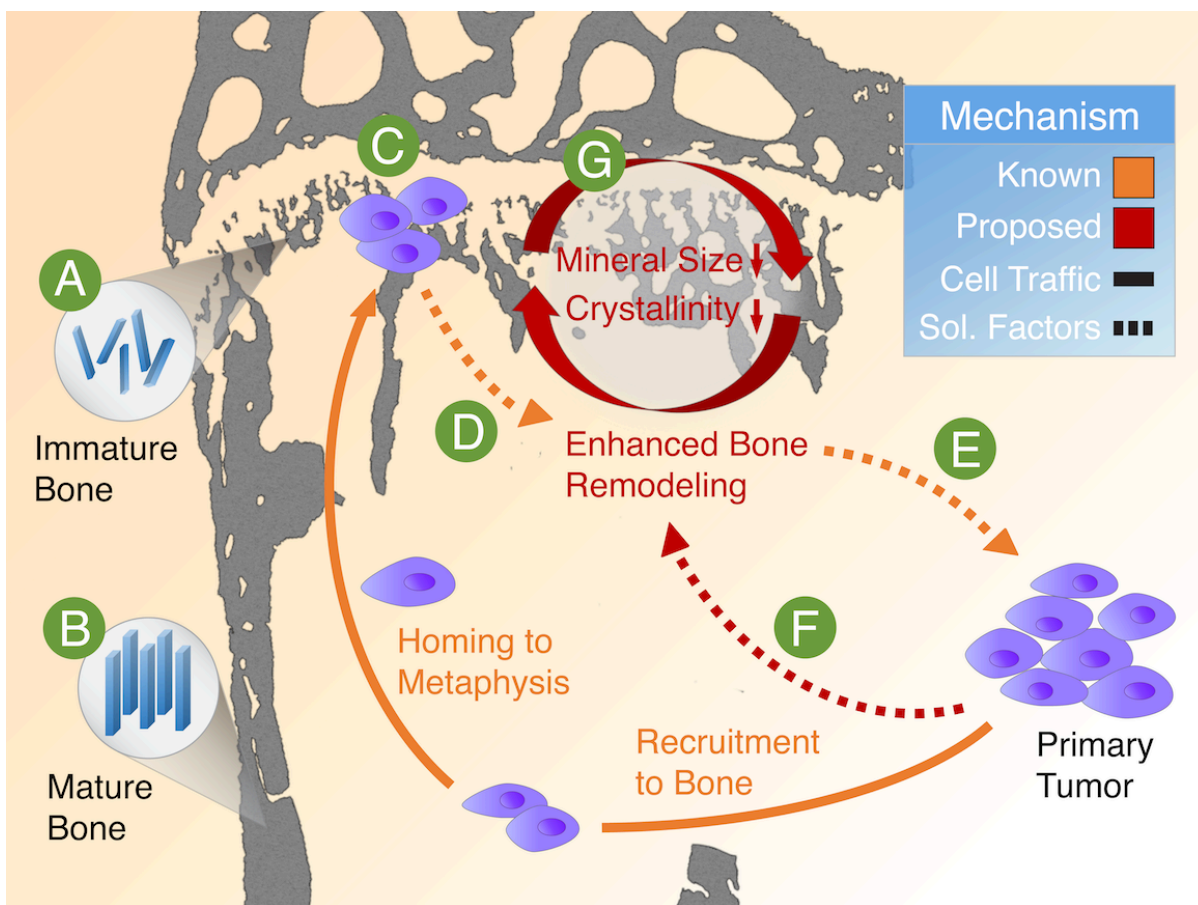


Figure 3.14: Proposed functional relationship between hydroxyapatite mineral characteristics and breast cancer bone metastasis. In mice, breast cancer cells typically colonize the metaphysis in the metabolically-active proximal tibia. We show that mineral in metaphyseal bone (A) is less mature (i.e., smaller, less perfect, and less oriented) relative to other skeletal locations (B) not prone to initiation of metastasis. Because previous *in vitro* findings show that tumor cells preferentially adhere to less mature crystals, we propose that this difference in mineral properties may be functionally relevant to the establishment of a tumor colony (C). The metastasized tumor cells can then disrupt typical bone remodeling processes (D) to result in the aberrant activity of bone cells and the increased release of tumor-recruiting soluble factors (E). Furthermore, breast cancer cells located within primary tumors can stimulate bone remodeling by secreting circulating factors (F) that enhance local osteogenesis and thus, alter the composition and structure of the bone extracellular matrix. Here, we propose that these pre-metastatic changes lead to the deposition of a less mature mineral phase (G) which may be essential in driving the vicious cycle of osteolytic bone metastasis.

may be affected by tumor-induced changes in HA nanostructure. Understanding how nanoscale variations in HA structure affect BP binding may aid the development of derivatives and protein conjugates (43) that are more effective in the treatment of bone metastasis.

Although limited by sample throughput, X-ray scattering analysis and large area Raman imaging generate position-resolved information on the micro- to nano- scales that can be combined with a host of other techniques to provide a comprehensive assessment of bone materials properties in a variety of pathological contexts. Thus, similar approaches to the one described in this paper can be used to assess bone nanostructure in animal models of other cancers (e.g. prostate, lung) that also metastasize to bone (2). Insights from these analyses will inform the design of biomimetic culture systems (44) and high-throughput screening platforms (45) to investigate the functional role of HA mineral in bone metastasis as well as the development of tissue-engineered tumor models that recapitulate the bone microenvironment (46). Moreover, future work will also need to consider the effect of changing bone mineral properties in the context of the intimately-associated collagen fibrils and adhesive proteins enriched in the metastatic site. Interdisciplinary collaborations between the fields of biomaterials, cancer biology, and oncology will be key to this promising new field of work in which materials science approaches will play an important role.

3.6 Acknowledgements

We thank Chenghao Li, Stefan Siegel, and Ingrid Zenke for assistance with SAXS/WAXS; Birgit Schonert and Gabriele Wienskol for assistance with sample preparation; Sabine Stumpp for assistance with histology; Eve Donnelly for critical reading of the manuscript; and Françoise Vermeulen for consultation with statistical analysis. BoM1-2287 cells were a gift from Joan Massagué. This work was funded by NIH (R01CA173083), NCI (1U54CA199081-01, 1U54CA210184-01), NSF (Fellowship to F.H.), and the Alexander von Humboldt Foundation (Fellowship to C.F.).

3.7 References

1. Kozlow W, Guise TA (2005) Breast cancer metastasis to bone: Mechanisms of osteolysis and implications for therapy. *J Mammary Gland Biol Neoplasia* 10(2):169–180.
2. Ren G, Esposito M, Kang Y (2015) Bone metastasis and the metastatic niche. *J Mol Med* 93(11):1203–1212.
3. Weilbaecher KN, Guise TA, McCauley LK (2011) Cancer to bone: a fatal attraction. *Nat Rev Cancer* 11(6):411–425.
4. Wang H, et al. (2015) The Osteogenic Niche Promotes Early-Stage Bone Colonization of Disseminated Breast Cancer Cells. *Cancer Cell* 27(2):193–210.
5. Fratzl P, Gupta HS, Paschalis EP, Roschger P (2004) Structure and mechanical quality of the collagen-mineral nano-composite in bone. *J Mater Chem* 14(14):2115.
6. Reznikov N, Shahar R, Weiner S (2014) Bone hierarchical structure in three dimensions. *Acta Biomater* 10(9):3815–3826.
7. Olszta MJ, et al. (2007) Bone structure and formation: A new perspective. *Mater Sci Eng R Reports* 58(3–5):77–116.
8. Boskey A, Mendelsohn R (2005) Infrared analysis of bone in health and disease. *J Biomed Opt* 10(3):31102.
9. Bi X, et al. (2013) Prostate cancer metastases alter bone mineral and matrix composition independent of effects on bone architecture in mice — A quantitative study using microCT and Raman spectroscopy. *Bone* 56(2):454–460.
10. Burke M, et al. (2017) The impact of metastasis on the mineral phase of vertebral bone tissue. *J Mech Behav Biomed Mater* 69(October 2016):75–84.
11. Lange C, et al. (2011) Fetal and postnatal mouse bone tissue contains more calcium than is present in hydroxyapatite. *J Struct Biol* 176(2):159–167.
12. Bigi A, et al. (1997) Chemical and structural characterization of the mineral phase from cortical and trabecular bone. *J Inorg Biochem* 68(1):45–51.
13. Kuhn LT, et al. (2008) A comparison of the physical and chemical differences between cancellous and cortical bovine bone mineral at two ages. *Calcif Tissue Int* 83(2):146–154.
14. Pathi SP, Lin DDW, Dorvee JR, Estroff LA, Fischbach C (2011) Hydroxyapatite nanoparticle-containing scaffolds for the study of breast cancer bone metastasis. *Biomaterials* 32(22):5112–5122.
15. Choi S, Coonrod S, Estroff L, Fischbach C (2015) Chemical and physical properties of carbonated hydroxyapatite affect breast cancer cell behavior. *Acta Biomater* 24:333–342.

16. Wu F, et al. (2017) Protein-crystal interface mediates cell adhesion and proangiogenic secretion. *Biomaterials* 116:174–185.
17. Thorpe MP, et al. (2011) Breast tumors induced by N-methyl-N-nitrosourea are damaging to bone strength, structure, and mineralization in the absence of metastasis in rats. *J Bone Miner Res* 26(4):769–776.
18. Lynch ME, et al. (2013) In vivo tibial compression decreases osteolysis and tumor formation in a human metastatic breast cancer model. *J Bone Miner Res* 28(11):2357–2367.
19. Pabisch S, Wagermaier W, Zander T, Li C, Fratzl P (2013) *Imaging the nanostructure of bone and dentin through small- and wide-angle X-ray scattering* (Elsevier Inc.). 1st Ed. Available at: <http://dx.doi.org/10.1016/B978-0-12-416617-2.00018-7>.
20. Fratzl P, H. G, P. R, K. K (2009) Bone Nanostructure and its Relevance for Mechanical Performance, Disease, and Treatment. *Nanotechnology, Volume 5: Nanomedicine* (WILEY-VCH Verlag GmbH & Co), pp 345–360.
21. Gamsjaeger S, Kazanci M, EP P, Fratzl P (2009) Raman Application in Bone Imaging. *Raman Spectroscopy for Soft Matter Applications*, ed Maher S. Amer (John Wiley & Sons, Inc), pp 227–267.
22. Kazanci M, Roschger P, Paschalis EP, Klaushofer K, Fratzl P (2006) Bone osteonal tissues by Raman spectral mapping: Orientation-composition. *J Struct Biol* 156(3):489–496.
23. Wright LE, et al. (2016) Murine models of breast cancer bone metastasis. *Bonekey Rep* 5:1–11.
24. Kang Y, et al. (2003) A multigenic program mediating breast cancer metastasis to bone. *Cancer Cell* 3(6):537–549.
25. Mastro AM, Gay C V., Welch DR (2003) The skeleton as a unique environment for breast cancer cells. *Clin Exp Metastasis* 20(3):275–284.
26. Clarke B (2008) Normal bone anatomy and physiology. *Clin J Am Soc Nephrol* 3(3):S131–S139.
27. Tesch W, et al. (2003) Orientation of Mineral Crystallites and Mineral Density During Skeletal. 18(1):117–125.
28. Joiner DM, et al. (2014) Accelerated and Increased Joint Damage in Young Mice with Global Inactivation of Mitogen-Inducible Gene 6 (MIG-6) after Ligament and Meniscus Injury. *Arthritis Res Ther* 16(2):R81.
29. Bloebaum RD, Skedros JG, Vajda EG, Bachus KN, Constantz BR (1997) Determining

- mineral content variations in bone using backscattered electron imaging. *Bone* 20(5):485–490.
30. Yerramshetty JS, Akkus O (2008) The associations between mineral crystallinity and the mechanical properties of human cortical bone. *Bone* 42(3):476–482.
 31. Cox TR, et al. (2015) The hypoxic cancer secretome induces pre-metastatic bone lesions through lysyl oxidase. *Nature* 522(7554):106–110.
 32. Kelly T, et al. (2005) Expression of heparanase by primary breast tumors promotes bone resorption in the absence of detectable bone metastases. *Cancer Res* 65(13):5778–5784.
 33. Kuperwasser C, et al. (2005) A mouse model of human breast cancer metastasis to human bone. *Cancer Res* 65(14):6130–6138.
 34. McLain RF (2006) *Cancer in the Spine* ed McLain R (Humana Press). 1st Ed. doi:10.1007/978-1-59259-971-4.
 35. De Yoreo JJ, et al. (2015) Crystallization by particle attachment in synthetic, biogenic, and geologic environments. *Science* (80-) 349(6247):aaa6760-aaa6760.
 36. Mahamid J, et al. (2011) Bone mineralization proceeds through intracellular calcium phosphate loaded vesicles: A cryo-electron microscopy study. *J Struct Biol* 174(3):527–535.
 37. George A, Veis A (2008) Phosphorylated proteins and control over apatite nucleation, crystal growth, and inhibition. *Chem Rev* 108(11):4670–4693.
 38. Jilka RL (2013) The relevance of mouse models for investigating age-related bone loss in humans. *Journals Gerontol - Ser A Biol Sci Med Sci* 68(10):1209–1217.
 39. Piao J, et al. (2013) Sirt6 regulates postnatal growth plate differentiation and proliferation via Ihh signaling. *Sci Rep* 3:3022.
 40. Nagano M, Nakamura T, Kokubo T, Tanahashi M, Ogawa M (1996) Differences of bone bonding ability and degradation behaviour in vivo between amorphous calcium phosphate and highly crystalline hydroxyapatite coating. *J Biomed Mater Res* 17(18):1771–1777.
 41. Barry AB, Baig AA, Miller SC, Higuchi WI (2002) Effect of age on rat bone solubility and crystallinity. *Calcif Tissue Int* 71(2):167–171.
 42. Wright JE, Zhao L, Choi P, Uludag H (2004) Simulating hydroxyapatite binding of bone-seeking bisphosphonates. *Adv Exp Med Biol* 553:139–148.
 43. Gittens SA, Bansal G, Zernicke RF, Uludag H (2005) Designing proteins for bone targeting. *Adv Drug Deliv Rev* 57(7):1011–1036.
 44. Murphy WL, Hsiong S, Richardson TP, Simmons CA, Mooney DJ (2005) Effects of a

bone-like mineral film on phenotype of adult human mesenchymal stem cells in vitro. *Biomaterials* 26(3):303–310.

45. Barney LE, et al. (2015) A cell–ECM screening method to predict breast cancer metastasis. *Integr Biol (Camb)* 7(2):198–212.
46. Seib FP, Berry JE, Shiozawa Y, Taichman RS, Kaplan DL (2015) Tissue engineering a surrogate niche for metastatic cancer cells. *Biomaterials* 51:313–319.

CHAPTER 4: CONCLUSIONS

Hydroxyapatite (HA) mineral is a prevalent yet underappreciated extracellular matrix (ECM) component of both the primary and bone metastatic sites of breast cancer. Previous studies have suggested that HA can regulate cancer cell behavior, yet it is unclear whether the presence of HA mineral in these breast cancer microenvironments is relevant to metastatic disease. This general lack of understanding may be due to limitations in current research methodologies. As such, the overall goal of this doctoral work was to investigate interactions between tumor cells and HA in the bone metastatic cascade of breast cancer by employing physical sciences-based approaches in combination with pathologically-relevant *in vitro* or *in vivo* model systems.

4.1 A dynamic reciprocity between breast cancer cells and HA mineral

The studies described herein suggest a dynamic reciprocity between breast cancer cells and the HA embedded within their mineralized microenvironments. As mammary microcalcifications (MCs) composed of HA mineral are commonly associated with malignant disease, it is certainly conceivable that HA could be actively contributing to the progression of breast cancer – though mechanisms remain largely unexplored. Chapter 2 described the use of a mineral-containing 3D culture system to functionally characterize the effect of HA exposure on a cell line model of ductal carcinoma *in situ* (DCIS), which is considered a premalignant condition that presents with MCs in over 90% of clinical cases. Interestingly, it was found that HA mineral stimulated the DCIS cells to adopt morphological changes that were reflective of increased invasiveness and to exhibit increased migratory behavior that was linked to IL-8 signaling. The increased individualization

*Certain text adapted from He F, Choi SY, Estroff LA, Fischbach C (2017) Mineralized 3D Culture Systems for Studying Bone Metastatic Breast Cancer. *Engineering 3D Tissue Test Systems*, ed Burg K. (Taylor and Francis Group), pp 169-191.

of DCIS cell pre-cultured in HA-containing scaffolds suggests that mineral may in fact be activating elements of the epithelial-to-mesenchymal transition (EMT) known to be associated with invasive cells, though additional experiments to assess the hallmarks of EMT (1), such as decreased E-cadherin expression at cell junctions, will need to be performed. Additionally, it was found that DCIS xenograft tumors initiated in HA scaffolds exhibited evidence of enhanced malignant progression. Future studies will be needed to investigate this further by increasing the number of experimental endpoints and by detecting potential dissemination in the lymph nodes and common metastatic sites of breast cancer, such as the bones and lungs. Collectively, IL-8 was identified as a potential HA-mediated driver of DCIS malignant progression. In a set of human breast cancer samples, higher IL-8 expression was not only correlated with the presence of mammographically-detected calcifications but also with PR- and HER2+ subtypes that are associated with higher grade lesions (2). The small sample size of the assessed patient cohort, however, limits the strength of these conclusions. More research will be needed to assess IL-8 as a useful prognostic biomarker in DCIS patients with suspicious MCs.

Following dissociating from the primary tumor, metastatic breast cancer cells will enter systemic circulation and preferentially establish a secondary tumor in the skeleton. Thus, it is likely that interactions between breast cancer cells and the mineralized bone ECM may play a critical role in the development of bone metastasis. However, current studies largely overlook the HA mineral that is an essential nanostructural component of bone. Thus, chapter 3 described efforts to characterize materials properties of the bone metastatic site in mouse models of advanced breast cancer. Bone HA nanocrystals were observed to be more immature in the metaphyseal region of the proximal tibiae known (3) and confirmed (Fig. 3.5) to be a highly common site of metastasis in models of bone metastasis. This was an expected result, for the metaphysis largely consists of newly formed trabecular bone. What was more interesting, however, was that in a model of

localized breast cancer, the bone mineral nanostructure was observed to be even more immature in the growth plate region of the metaphysis when compared to healthy controls. Theoretically, this difference in HA nanocrystal structure could have been mediated by either bone-building or bone-destroying processes. A cell-free systemic conditioning experiment with daily injections of tumor conditioned media raised the possibility that tumor-derived soluble factors could alter the balance of bone matrix remodeling by activating mechanisms of bone formation. This result was importantly in accordance with recent studies showing that early disseminated breast cancer cells require interaction with osteoblast-lineage cell types to establish micro-metastatic colonies in the bone (4). Nevertheless, follow-up studies to more thoroughly elucidate mechanisms of pre-metastatic changes to bone nanostructure will be needed, with emphasis on the cross-talk between cancer cells, bone-resident cells, and the mineralized bone ECM.

4.2 Connections to the “seed-and-soil” theory of metastasis

Given that HA mineral is such a ubiquitous ECM-embedded component of malignant mammary tissue and the bone metastatic site, one could speculate that HA may be a vital micro-environmental parameter that selectively enables bone metastases from the primary breast tumor. This line of thinking is in accordance with the recently reinvigorated “seed-and-soil” concept, which argues that site-specific metastasis occurs only if the target organ provides a fertile ground for tumor cells to seed (5–7). Also known as the pre-metastatic niche, this concept has formed the basis of investigations (8) focused on the tendency of metastatic breast cancers to spread to its preferred locations, include lungs, liver, bone and brain (9). While bone-resident cells are known to be recruited to facilitate metastatic processes in these sites (10), studies of the bone pre-metastatic niche itself are scarce due to a lack of models that can recapitulate the entirety of the bone metastatic cascade (11).

Indeed, the skeletal microenvironment possesses highly favorable characteristics for metastatic cell outgrowth (3). Breast cancer cells are known to hijack molecular and cellular machinery used by hematopoietic stem cells in order to home to and grow within bone (12). For example, expression of chemokine receptor type 4 (CXCR4) in bone metastatic breast cancer cells renders them responsive to stromal cell-derived factor 1 (SDF-1) secreted by bone marrow-derived mesenchymal cells (13–15). Furthermore, the specific physical properties (e.g., acidic pH, high extracellular calcium concentration, hypoxia) of the bone microenvironment promote tumor-cell growth (16). Once seeded in bone, tumor cells disrupt the homeostatic interplay between bone-forming osteoblasts and bone-degrading osteoclasts leading to the net effect of osteolysis during advanced stages of disease. Bone degradation, in turn, further activates the vicious cycle of bone metastasis by releasing tumorigenic growth factors and cytokines, including transforming growth factor beta (TGF- β) and insulin-like growth factor 1 (IGF-1) that foster secondary tumor development (12, 17, 18).

Whether tumor–cell interactions with the inorganic mineral HA impact the aforementioned processes by influencing either the seed or the soil (or both) remains unknown. For example, one may hypothesize that HA at the primary site primes tumor cells for seeding to bone by upregulating genes that facilitate bone metastasis (14). A recent study has shown that the presence of cancer-associated fibroblasts within the mammary tumor selects for a subset of Src-hyperactive cancer cells that are predisposed to metastasize to the SDF-1- and IGF-1-enriched bone microenvironment (19). It is possible that HA mineral may play a contributing role in this selection process. Preliminary evidence obtained from Luminex-based phospho-kinase profiling suggests that breast cancer cells cultured in HA scaffolds may exhibit an increase in Src active site (pY419) phosphorylation after an experimental timeframe of 9 days (Fig. A.1A). The lack of response in the 72 condition suggests that an HA-mediated response in Src activity may have a certain latency

period (Fig. A.1A). Interestingly, a similar trend in both response and latency was observed in the activity of ERK (Fig. A.1B), which is known to be an essential regulator of EMT (20, 21).¹ Additionally, HA could conceivably enhance expression of the SDF-1 and IGF-1 cognate receptors CXCR4 or IGF-1R, although future studies to explore these potential mechanisms will need to be conducted. Furthermore, there is also emerging evidence to suggest that the deposition of HA mineral increases as a function of breast cancer cell aggressiveness (22, 23), which implies that the more malignant the lesion, the more likely it is for cells in that lesion to be exposed to HA mineral.

Meanwhile, it is also conceivable that tumor cells in the primary site remotely modify the bone ECM to facilitate eventual colonization. However, there currently exists limited data on ECM structural organization in the pre-metastatic niche (24), and many of these studies are focused on the LOX-mediated cross-linking of the lung ECM (25, 26). In chapter 3 of this work, it was found that structural alterations of bone mineral in the metastatic site could be attributed to enhanced bone remodeling via tumor-derived factors. It is possible that disseminated tumor cells may leverage these tumor-induced HA nanostructural and physiochemical variations in bone – as suggested by studies with synthetically-defined *in vitro* cultures (27–29) – to more effectively seed and form colonies. Moreover, the resulting higher extracellular calcium levels that accompany altered bone homeostasis could be favorable for growth of the secondary tumor.

¹Author's note: The Src and ERK results in the Appendix are preliminary and should be confirmed with follow-up experiments.

4.3 Future directions and perspectives

4.3.1 Considerations for developing mineral-containing models of breast cancer and bone metastasis

When investigating the influence of HA mineral on breast cancer bone metastasis, it needs to be kept in mind that the materials properties and formation mechanisms of HA in mammary MCs and in the bone matrix vary significantly. As described in chapter 1, the HA mineral in the calcified mammary tissue appears to be formed independently from the organic matrix while the HA mineral in the bone is more intimately associated with it, as the crystallization of bone mineral occurs in the hole zones of aligned collagen fibrils during the development of the structural nanocomposite (30). Moreover, the calcified deposits in the breast can be extremely heterogeneous in both size and spatial distribution and can be orders of magnitude larger than the mineral particles in bone (31).

Considering how tumor cells can conceivably be exposed to pure mineral in the mammary tissue, the use of mineral-containing PLG scaffolds for investigating cell-microcalcification interactions may be appropriate. One particular advantage of this approach is the ability to modulate the physicochemical and structural parameters of the scaffold-incorporated HA mineral. Indeed, some of these properties, such as carbonate and metal ion content, have already been correlated with malignancy in spectroscopic analyses of human breast tissues (31, 32). Thus, having a high level of control in the synthesis of HA variations will enable the functional characterization of how these different properties may regulate breast cancer cell behavior.

However, mineral-containing PLG scaffolds may not be as well-suited to modeling tumor-bone matrix interactions because they do not contain the organic matter that is essential to the structural basis of bone. Thus, mineralized collagen scaffolds (33–35), currently being developed for bone regeneration applications, may be a viable alternative. Fabricated by freeze-drying

precursor solutions of collagen and glycosaminoglycans, these porous scaffolds can be modulated to adopt differential porous architectures and enriched for select growth factors. However, although these scaffolds would permit the 3D growth of cancer cells in bone-like matrix, they are still far from mimicking native bone ultrastructure. To this end, researchers are developing bioinspired methods of incorporating HA mineral into the collagen fibrillar microstructure by using highly negatively charged polymers such as polyaspartic acid to stabilize the formation of the amorphous calcium phosphate precursor during the mineralization process (36). Interestingly, a recent study has found differences in mechanosignaling when breast cancer cells were cultured on microwells consisting of either mineralized or non-mineralized collagen fibrils (37). The challenge moving forward will be to develop methods of controlling nanostructural and physicochemical parameters of mineral within these biomimetic composites to reflect tumor-associated states of bone quality.

4.3.2 Organs-on-a-chip: modeling metastatic processes on the whole-body level

Mineral responses could be regulated at the organ, or whole-body level particularly, as cells responding to mineral at the primary site may alter mineral properties at the secondary site. Yet, most culture approaches focus at the cellular or tissue scale. Microfluidic “organ-on-a-chip” devices provide spatial and temporal control of biochemical, biophysical, and mechanical cues, and have been used to mimic the structure and function of various tissues and organs and their communication with one another (38). Examples of how such devices have been used in the context of bone include the modeling of hematopoietic niches, screening the wound-healing potential of specific biomaterials, and assaying the invasive dynamics of breast cancer cells (39–41). Collectively, these studies suggest that “bone-on-a-chip” models could effectively recreate 3D bone environments with multiple cellular and matrix components under conditions of dynamic

flow; thereby, it is conceivable that methods to produce mineralized matrices can be co-opted for developing microfluidic systems. However, many current devices are limited to individual cells or organs. In order to recapitulate the complex metastatic cascade, the system-like integration of multiple organs will be required.

4.3.3 Concluding remarks: physical sciences approaches may accelerate cancer research

The results from this work have not only offered valuable insights for cancer biology but have also contributed to the fields of tissue engineering and biomaterials science. Chapter 2 provided further evidence that polymeric scaffolds, originally designed for tissue engineering purposes, can be used to study defined components of the tumor microenvironment in a controlled and pathologically-relevant manner. These studies strongly suggest that HA mineral should be treated as active rather than passive indicators of cancer. Meanwhile, chapter 3 demonstrated that creative synergy between the fields of cancer biology and materials sciences enables the high-resolution characterization of ECM parameters that would not be possible with conventional approaches. Here, the changing bone ECM observed in a mouse model with localized tumors highlights the systemic nature of bone metastatic disease. There are certainly limitations to the models used in this study that will need to be addressed with future advances. Yet the author is optimistic that breakthroughs will arise as long as the spirit of undeterred and wide-eyed inquiry endures. Continuing in this tradition to collaborate across the biological and physical sciences may accelerate research to uncover the multifactorial mechanisms of metastatic breast cancer, ultimately providing hope for the millions of patients worldwide who are desperate for a cure.

4.4 References

1. Thiery JP (2002) Epithelial–mesenchymal transitions in tumour progression. *Nat Rev Cancer* 2(6):442–454.
2. Simpson PT, Reis-Filho JS, Gale T, Lakhani SR (2005) Molecular evolution of breast cancer. *J Pathol* 205(2):248–254.
3. Mastro AM, Gay C V., Welch DR (2003) The skeleton as a unique environment for breast cancer cells. *Clin Exp Metastasis* 20(3):275–284.
4. Wang H, et al. (2015) The Osteogenic Niche Promotes Early-Stage Bone Colonization of Disseminated Breast Cancer Cells. *Cancer Cell* 27(2):193–210.
5. Paget S (1889) the Distribution of Secondary Growths in Cancer of the Breast. *Lancet* 133(3421):571–573.
6. Langley RR, Fidler IJ (2011) The seed and soil hypothesis revisited-The role of tumor-stroma interactions in metastasis to different organs. *Int J Cancer* 128(11):2527–2535.
7. Cox TR, Gartland A, Erler JT (2012) The pre-metastatic niche: is metastasis random? *Bonekey Rep* 1(5):1–5.
8. Liu Y, Cao X (2016) Characteristics and Significance of the Pre-metastatic Niche. *Cancer Cell* 30(5):668–681.
9. Nguyen DX, Bos PD, Massagué J (2009) Metastasis: From dissemination to organ-specific colonization. *Nat Rev Cancer* 9(4):274–284.
10. Kaplan RN, Psaila B, Lyden D (2006) Bone marrow cells in the “pre-metastatic niche”: Within bone and beyond. *Cancer Metastasis Rev* 25(4):521–529.
11. Ren G, Esposito M, Kang Y (2015) Bone metastasis and the metastatic niche. *J Mol Med* 93(11):1203–1212.
12. Weilbaecher KN, Guise TA, McCauley LK (2011) Cancer to bone: A fatal attraction. *Nat Rev Cancer* 11(6):411–425.
13. Müller A, et al. (2001) Involvement of chemokine receptors in breast cancer metastasis. *Nature* 410(6824):50–56.
14. Kang Y, et al. (2003) A multigenic program mediating breast cancer metastasis to bone. *Cancer Cell* 3(6):537–549.
15. Teicher BA, Fricker SP (2010) CXCL12 (SDF-1)/CXCR4 pathway in cancer. *Clin Cancer Res* 16(11):2927–2931.

16. Kingsley LA, Fournier PGJ, Chirgwin JM, Guise TA (2007) Molecular Biology of Bone Metastasis. *Mol Cancer Ther* 6(10):2609–2617.
17. Mundy GR (2002) Metastasis to bone: Causes, consequences and therapeutic opportunities. *Nat Rev Cancer* 2(8):584–593.
18. Kozlow W, Guise TA (2005) Breast cancer metastasis to bone: Mechanisms of osteolysis and implications for therapy. *J Mammary Gland Biol Neoplasia* 10(2):169–180.
19. Zhang XHF, et al. (2013) Selection of bone metastasis seeds by mesenchymal signals in the primary tumor stroma. *Cell* 154(5):1060–1073.
20. Lamouille S, Xu J, Derynck R (2014) Molecular mechanisms of epithelial-mesenchymal transition. *Nat Rev Mol Cell Biol* 15(3):178–196.
21. Navandar M, et al. (2017) ERK signalling modulates epigenome to drive epithelial to mesenchymal transition. *Oncotarget* 8(17):29269–29281.
22. Scimeca M, et al. (2014) Microcalcifications in breast cancer: An active phenomenon mediated by epithelial cells with mesenchymal characteristics. *BMC Cancer* 14(1):286.
23. Vidavsky N, et al. (2018) Studying biomineralization pathways in a 3D culture model of breast cancer microcalcifications. *Biomaterials* 179:71–82.
24. Høye AM, Erler JT (2016) Structural ECM components in the premetastatic and metastatic niche. *Am J Physiol - Cell Physiol* 310(11):C955–C967.
25. Wong CC-L, et al. (2011) Hypoxia-inducible factor 1 is a master regulator of breast cancer metastatic niche formation. *Proc Natl Acad Sci* 108(39):16369–16374.
26. Cox TR, et al. (2013) LOX-mediated collagen crosslinking is responsible for fibrosis-enhanced metastasis. *Cancer Res* 73(6):1721–1732.
27. Pathi SP, Lin DDW, Dorvee JR, Estroff LA, Fischbach C (2011) Hydroxyapatite nanoparticle-containing scaffolds for the study of breast cancer bone metastasis. *Biomaterials* 32(22):5112–5122.
28. Choi S, Coonrod S, Estroff L, Fischbach C (2015) Chemical and physical properties of carbonated hydroxyapatite affect breast cancer cell behavior. *Acta Biomater* 24:333–342.
29. Wu F, et al. (2017) Protein-crystal interface mediates cell adhesion and proangiogenic secretion. *Biomaterials* 116:174–185.
30. Fratzl P, Gupta HS, Paschalis EP, Roschger P (2004) Structure and mechanical quality of the collagen-mineral nano-composite in bone. *J Mater Chem* 14(14):2115–2123.
31. Kunitake JAMR, et al. (2018) Correlative imaging reveals physiochemical heterogeneity

- of microcalcifications in human breast carcinomas. *J Struct Biol* 202(1):25–34.
32. Baker R, Rogers KD, Shepherd N, Stone N (2010) New relationships between breast microcalcifications and cancer. *Br J Cancer* 103(7):1034–1039.
 33. Ren X, et al. (2016) Nanoparticulate mineralized collagen scaffolds induce in vivo bone regeneration independent of progenitor cell loading or exogenous growth factor stimulation. *Biomaterials* 89:67–78.
 34. Weisgerber DW, Caliarì SR, Harley BAC (2015) Mineralized collagen scaffolds induce hMSC osteogenesis and matrix remodeling. *Biomater Sci* 3(3):533–542.
 35. Caliarì SR, Harley BAC (2014) Structural and biochemical modification of a collagen scaffold to selectively enhance MSC tenogenic, chondrogenic, and osteogenic differentiation. *Adv Healthc Mater* 3(7):1086–1096.
 36. Nudelman F, Lausch AJ, Sommerdijk NAJM, Sone ED (2013) In vitro models of collagen biomineralization. *J Struct Biol* 183(2):258–269.
 37. Choi S, et al. (2018) Intrafibrillar, bone-mimetic collagen mineralization regulates breast cancer cell adhesion and migration. *Biomaterials* 10:1–12.
 38. Esch EW, Bahinski A, Huh D (2015) Organs-on-chips at the frontiers of drug discovery. *Nat Rev Drug Discov* 14(4):248–260.
 39. Lee JH, Gu Y, Wang H, Lee WY (2012) Microfluidic 3D bone tissue model for high-throughput evaluation of wound-healing and infection-preventing biomaterials. *Biomaterials* 33(4):999–1006.
 40. Bersini S, et al. (2014) A microfluidic 3D invitro model for specificity of breast cancer metastasis to bone. *Biomaterials* 35(8):2454–2461.
 41. Torisawa YS, et al. (2014) Bone marrow-on-a-chip replicates hematopoietic niche physiology in vitro. *Nat Methods* 11(6):663–669.

APPENDIX

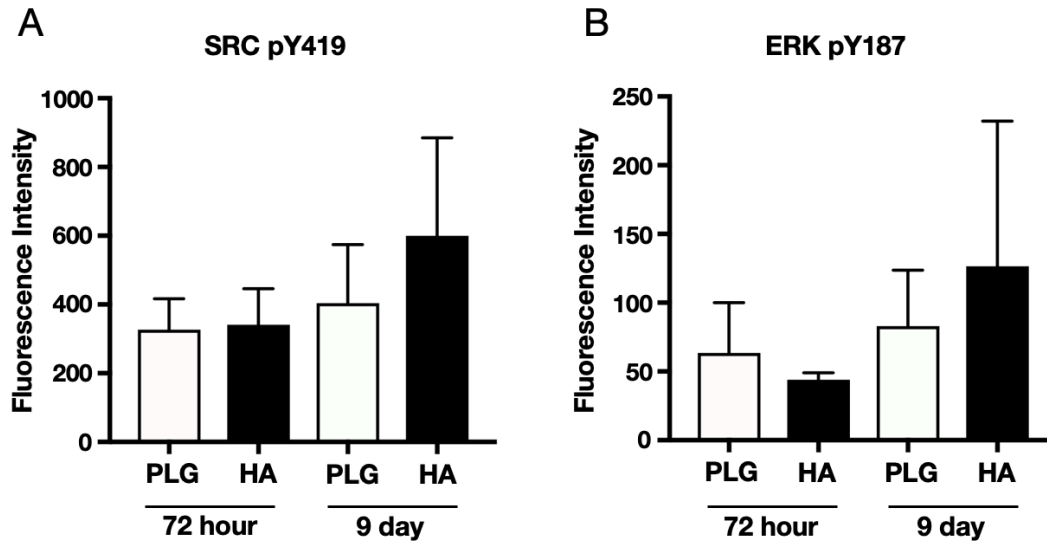


Figure A.1: Hydroxyapatite mineral may increase SRC and ERK phosphorylation. (A, B) Bead-based Luminex profiling of SRC (A) and ERK (B) active site phosphorylations in protein lysates generated from MDA-MB-231 cells cultured on PLG or HA scaffolds for the indicated timepoints.

Materials and Methods

Protein lysate generation

MDA-MB-231 cells were cultured on hydroxyapatite and PLG scaffolds for timepoints of 72 hours and 9 days then lysed in RIPA buffer (Thermo Fisher) supplemented with protease (Thermo Fisher) and phosphatase (Roche) inhibitors. Protein lysates were normalized to 1 mg/ml and immediately stored in -80C.

Profiling of kinase phosphorylation

Luminex immunosandwich assays were performed as previously described (1). Raw data were normalized by subtracting sample and antibody background signals.

1. Du J, et al. (2009) Bead-based profiling of tyrosine kinase phosphorylation identifies SRC as a potential target for glioblastoma therapy. *Nat Biotechnol* 27(1):77–83.